The Mineralogy and Chemical Evolution of the Earth's Deep Mantle

by

Byeongkwan Ko

A Dissertation Presented in Partial Fulfillment
of the Requirements for the Degree
Doctor of Philosophy

Approved January 2020 by the
Graduate Supervisory Committee:

Sang-Heon Shim, Chair
Edward Garnero
Steve Desch
Kurt Leinenweber
Mingming Li

ARIZONA STATE UNIVERSITY

May 2020

ABSTRACT

The mineralogy of the deep mantle is one of the key factors for the chemical evolution of the Earth. The constituent minerals of the mantle rock control the physical properties of the mantle, which have significant impacts on the large-scale processes occurring in the Earth's interior. In my PhD research, I adopted experimental approaches to investigate the mineralogy and the physical properties of the Earth's materials in the deep mantle by using the diamond anvil cells (DACs) combined with in-situ X-ray diffraction techniques.

First, I found that Ca-bearing bridgmanite can be stable in the deeper part of the Earth's lower mantle where temperature is sufficiently high. The dissolution of calcium into bridgmanite can change the physical properties of the mantle, such as compressibility and viscosity. This study suggests a new mineralogical model for the lower mantle, which is composed of the two layers depending on whether calcium dissolves in bridgmanite or forms $CaSiO_3$ perovskite as a separate phase.

Second, I investigated the mineralogy and density of the subducting materials in the Archean at the P–T conditions near 670 km-depth. The experiments suggest that the major phases of Archean volcanic crust is majoritic garnet and ringwoodite in the P–T conditions of the deep transition zone, which become bridgmanite with increasing pressure. The density model showed that Archean volcanic crust would have been denser than the surrounding mantle, promoting sinking into the lower mantle regardless of the style of the transportation in the Archean.

Lastly, I further investigated the mineralogies and densities of the ancient volcanic crusts for the Archean and Proterozoic at the P–T conditions of the lower mantle. The experiments suggest that the mineralogy of the ancient volcanic crusts is composed mostly of bridgmanite, which is systemically denser than the surrounding lower mantle. This implies that the ancient volcanic crusts would have accumulated at the

base of the mantle because of their large density and thickness. Therefore, the distinctive chemistry of the ancient volcanic crusts from the surrounding mantle would have given a rise to the chemical heterogeneities in the region for billions of years.

ACKNOWLEDGMENTS

I would like to express my sincere gratitude to my PhD advisor Prof. Sang-Heon Shim for his tremendous support and priceless advice during my PhD journey. I could not have imagined having a better advisor for my PhD study and it would be impossible to count all the ways that he has guided me toward the right path.

I would like to give special thanks to my fantastic mentors: Prof. Ed Garnero, Prof. Steve Desch, Dr. Kurt Leinenweber, and Prof. Mingming Li for their insightful comments and encouragement. Their guidance helped me in all the time of research and writing of this dissertation.

My sincere thanks also go to my colleagues: Dr. Hélène Gluck, Dr. Huawei Chen, Dr. Carole Nisr, Prof. Yu Ye, Nathan Dolinschi, Britany Kulka, Harrison Allen-Sutter, Dr. Shule Yu, Dr. Qian Yuan, Taehyun Kim, and Dr. Hongyu Lai for their loyal friendship and support. They have helped my research in innumerable ways, both in the office and out in the world.

In addition, I would like to mention my collaborators: Dr. Vitali Prakapenka, Dr. Eran Greenburg, Dr. Clemens Prescher, Dr. Martin Kunz, Dr. Wenli Bi, Dr. Esen E. Alp, Dr. Yu meng, Dr. Kenneth Mossman, Dr. Manuel Roldan Gutierrez, Dr. Axel Wittmann, and Dr. Yao-Jen (Jerry) Chang who helped me to conduct my experiments in the laboratory and research facilities. I deeply appreciate their precious efforts that made my research possible.

Lastly, I would like to thank Chuhong Mai, my partner, for her unconditional support and love. When I suffered physically and mentally, her unceasing encouragement made me to move forward. I could not have accomplished my PhD journey without her.

TABLE OF CONTENTS

CHAPTER Page

CHAPTER Page

CHAPTER Page

CHAPTER Page

LIST OF TABLES

LIST OF FIGURES

Figure Page

Chapter 1

INTRODUCTION

1.1 The Chemical Evolution of the Earth's Deep Mantle

Earth is a tectonically active planet where many geological processes, such as subduction, sea-floor spreading, and continental rift occur continuously (e.g. Kearey *et al.*, 2009). Subduction enables the surface materials to sink into the Earth's mantle, whereas the sea-floor spreading and continental rifts form volcanic rocks from the partially-molten mantle near the surface.

Some of the subducted materials are recycled back to the mantle (e.g. Zindler and Hart, 1986; Cooper *et al.*, 2009). But the majority of the subducted materials, in the form of subducting slab that consists of the oceanic crust and its depleted residue (harzburgite layer), continues its journey to much greater depths (e.g. Van der Hilst *et al.*, 1997; Grand, 2002). The large-scale mass transport between the upper mantle and the lower mantle can take place by the sinking of subducted slabs into the lower mantle and by the plume-associated mantle upwelling. With these processes, the present-day mantle seems to convect as a whole (e.g. Van der Hilst *et al.*, 1997; Grand, 2002).

If subducting slabs arrive at some regions in the deep mantle and accumulate, the distintive chemistry of the oceanic crust at the top layer of the slabs can give rise to chemical heterogeneties in the mantle regions. The oceanic crust is composed mostly of the basaltic rock that forms in mid ocean ridges near the surface, which is called mid-ocean ridge basalt (MORB). MORB is enriched in Si, Al, and Ca (e.g. Gale *et al.*, 2013), whereas the upper-mantle rock (peridotite) is enriched in Mg (e.g. Mc-

Donough and Sun, 1995). The different chemistry forms the different mineralogy. For example, in the upper mantle, MORB is composed mainly of Si- and Al-rich minerals, (Mg,Fe,Ca)SiO_3 pyroxene and SiO_2 coesite, whereas peridotite is composed mainly of Mg-rich mineral, Mg_2SiO_4 olivine (Irifune and Ringwood, 1987b). Harzburgite, the underlying layer of the subducting slab, forms the similar mineralogy to the mantle with slightly different ratios of the constituent elements (e.g. Baker and Beckett, 1999). The mineralogical difference between the oceanic crust (MORB) in the subducting slab and the surrounding mantle lead to the differences in physical properties like density and viscosity. Also, despite of the similar chemistry to the mantle, the harzburgite layer can play a role in the differences in density and viscosity because of its cooler temperature than the surrounding mantle. The differences in density and viscosity are key parameters for sinking behaviors of the subducting slab (Chapter 1.2.3) and forming chemical heterogeneties in the deep mantle (Chapter 1.2.1). Thus, knowledge of the mineralogy of the subducting slab and the mantle can provide some insights on understanding the material circulations and the chemical evolution of the deep mantle.

The material circulations might have occurred through either subduction (e.g. Condie and Kröner, 2008; Laurent *et al.*, 2014; Tang *et al.*, 2016) or delamination (Davies, 1992; Capitanio *et al.*, 2010; Johnson *et al.*, 2014) since the Archean (4.0–2.5 Ga). The mantle in the past was hotter than in the present day, which produced the volcanic crust with the relatively much mafic composition compared to modern MORB (Chapter 1.2.6; Korenaga, 2008; Herzberg *et al.*, 2010). The hotter mantle also results in the thicker volcanic crust (Herzberg *et al.*, 2010) in the past. With the larger thickness, the ancient volcanic crusts would have played the larger roles in sinking behaviors of subducting slabs than modern MORB does in the present day. However, the sinking behaviors of the ancient subducting slabs or the delaminated

ancient volcanic crusts have been poorly constrained due to the limited knowledge of the mineralogy and the physical properties of the ancient volcanic crusts in the deep mantle.

In my PhD research, I have explored the mineralogies of the lower mantle and the ancient volcanic crusts in order to better understand the chemical evolution of the Earth's deep mantle. The followings are the key questions that I pursued during my PhD research:

1. What is the mineralogy of the Earth's lower mantle?
2. Is the Earth's lower mantle mineralogically homogeneous?
3. How have chemical heterogeneities formed in the Earth's lower mantle?
4. Has the scale of the material circulation changed over time?
5. What about the mineralogy of the mantles in other Earth-like exoplanets?

In this chapter, I will discuss the general background regarding these questions and give an overview of the chapters for the main research.

1.2 Mineralogy of the Earth's Lower Mantle

In pyrolitic composition, bridgmanite (Brg), ferropericlase (Fp), and calcium silicate perovskite (CaPv) have been known as the major phases in the lower mantle (Irifune *et al.*, 2010; Ishii *et al.*, 2018; Ricolleau *et al.*, 2009). Ca^{2+} is the largest cation among the major elements in the lower mantle. It has been believed that the substitution of Ca^{2+} for Mg^{2+} or Fe^{2+} in A-site of Brg is unlikely to occur in the lower mantle. Instead, previous studies have suggested that Ca exists in CaPv ($CaSiO_3$) as a separate phase throughout the lower mantle (Irifune *et al.*, 2010; Kesson *et al.*, 1998; Ricolleau *et al.*, 2009).

However, some experiments have intermittently reported the absence of CaPv in the pyrolitic compositions at the lower-mantle related conditions (Lee *et al.*, 2004; Ono *et al.*, 2005; Sinmyo and Hirose, 2013). These experiments were conducted in a range of pressures, but observed CaPv only at certain pressures. For example, Ono *et al.* (2005) observed CaPv at 28 and 97 GPa, but could not resolve the existence of CaPv at 35 and 58 GPa, implying that the pressure window of 30–95 GPa may exist where CaPv is not stable. In fact, this pressure range coincides fairly well with the pressure range of 30–70 GPa where the spin transition of Fe^{3+} in Brg occurs (Fujino *et al.*, 2012; Hsu *et al.*, 2011; Badro, 2014). This raises a question whether the spin transition of Fe^{3+} in Brg is related to the Ca incorporation into Brg in the pressure range of 30–95 GPa.

The pressure range for the lower mantle has been widely explored by the laser-heated diamond anvil cell (LHDAC) technique. However, in the LHDAC experiments, one of the most common difficulties is the temperature control. The temperature gradient within the sample could be very large with an error range of several tens of percentage (e.g. Sinmyo and Hirose, 2010). More importantly, given that a typical way of reaching the target temperature is to increase laser power gradually, the sample may have to experience the low temperatures where kinetics effects are large. This effect can cause the sample (typically glass as starting material) to crystallize into minerals that are stable at far lower temperatures than the intended target temperature. Once crystallized, it is possible that with increasing temperature, these minerals do not transform into the high-temperature minerals any further, but stay as metastable because of the slow kinetics in the limited time scale in the laboratory (e.g. Asahara *et al.*, 2005).

In laboratory measurements, the chemical composition of Brg often shows small but meaningful amount of Ca (up to Ca#5; Ricolleau *et al.*, 2010; Sinmyo and

Hirose, 2013; Gu *et al.*, 2016). These observations may provide a clue that Brg could incorporate Ca in its structure. The crystal structures of both $CaSiO_3$ CaPv and $(Mg,Fe)SiO_3$ Brg belong to the perovskite-type structure in a chemical formula of ABX_3 where A and B are cations and X is an anion.

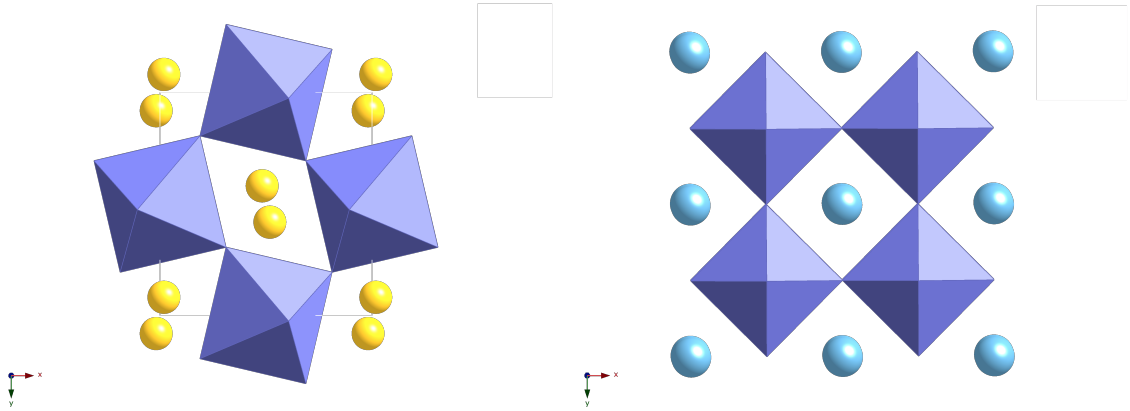

(a) $MgSiO_3$ bridgmanite (b) $CaSiO_3$ perovskite

Figure 1.1: Crytal structures of $MgSiO_3$ bridgmanite and $CaSiO_3$ perovskite. The yellow and blue spheres represent Mg and Ca cations, respectively. The blue polyhedra are the octahedra where Si bonds with 6 oxygen atoms at the corner. The c-axis is perpendicular to the paper.

Typically, the A-site is occupied by either Ca^{2+}, Mg^{2+}, or Fe^{2+}, the B-site is occupied by Si^{4+}, and X is O^{2-}. In the lower mantle, the stable form of CaPv is cubic because of the similar effective ionic sizes of Ca^{2+} and O^{2-} (1.34 and 1.35Å , respectively for 12-coordination; Shannon, 1976). The orthorhombic-structured Brg is stabilized by the octahedral tilting with respect to the cubic CaPv structure (Fig 1.1) because of the considerably smaller sizes of Mg^{2+} and Fe^{2+} (1.04 and 1.08Å , respectively for 12-coordination; Shannon, 1976) than the size of the dodecahedral site (A-site). The octahedral tilting angle is 0° for CaPv and 18° for $MgSiO_3$ Brg at ambient P–T conditions (Lundin *et al.*, 2008; Dorfman *et al.*, 2012). Dorfman *et al.*

(2013) showed that the octahedral tilting angle decreases with increasing Fe^{2+}# in Brg. Fe^{2+} is slightly larger than Mg^{2+}, thus substituting Mg^{2+} with Fe^{2+} in Brg results in a change of the crystal structure of orthorhombic Brg toward cubic by reducing the octahedral tilting angle. Like Fe^{2+}, Ca^{2+} may alter the crystal structure of Brg in a similar manner: it reduces the octahedral tilting angle so that its crystal structure becomes more cubic-like. This leads to a question whether the incorporation of Ca^{2+} in Brg or the formation of CaPv is energetically favored (i.e. which system holds lower internal energy between Ca-bearing Brg or Brg + CaPv).

If all Ca dissolves in Brg in the lower mantle, the major phases of the mineralogy would be Ca-bearing Brg (referred to as Ca-Brg) and Fp only. The Ca dissolution in Brg may change its properties, such as compressibility, density and viscosity. Brg is the most abundant mineral in the lower mantle. The changes in the chemistry and structure of Brg should result in the changes in the physical properties of the lower mantle. As discussed above, the previous reports by Lee *et al.* (2004); Ono *et al.* (2005); Sinmyo and Hirose (2013) indicate that the Ca dissolution in Brg may depend on the P-T conditions.

As part of my PhD study (Chapter 3), I adopted experimental approaches to examine the Ca solubility in Brg in the lower mantle. The mineralogy of the pyrolitic compositions was explored in a wide range of the P-T conditions of the lower mantle using the LHDAC technique. I employed the temperature control that can minimize the unintended kinetic effects at low temperatures. My new findings on the lower-mantle mineralogy will shed light on understanding the mineralogical structure of the lower mantle.

1.2.1 *Seismic Anomalies and Chemical Heterogeneities in Earth's Deep Mantle*

Seismological studies have observed numerous seismic anomalies in various scales in the deep mantle (Wu *et al.*, 2019; Kaneshima, 2016; Haugland *et al.*, 2017; Garnero *et al.*, 1998; He and Wen, 2009; Rost *et al.*, 2010). Many of them are attributed to the different chemistry of the local regions from the background mantle. For example, Wu *et al.* (2019) observed the small-scale topography at 660 km-depth in some regions, which requires the chemical layering. They suggested that an accumulation of ancient MORB may be responsible for the topography observations. Also, strong scatterers are detected within a depth range between 1400 and 1700 km in regions beneath Mariana and Peru (Kaneshima, 2016; Haugland *et al.*, 2017). Previous studies have attributed the detected small-scale heterogeneities to the phase transition of SiO_2 from stishovite to the $CaCl_2$-type silica (Kaneshima, 2016; Haugland *et al.*, 2017; Wang *et al.*, 2020), which is one of the major components in MORB in the conditions of the lower mantle (Ricolleau *et al.*, 2010).

In addition, small-scale seismic anomalies adjacent to the core-mantle boundary (CMB) have been reported. These anomalies are ultralow velocity zones (ULVZs), which are commonly tens of kilometers thick (Garnero and Helmberger, 1996; Williams and Garnero, 1996; He and Wen, 2009; Rost *et al.*, 2010) and characterized by significant velocity reductions up to 25% and 50% for P wave (Brown *et al.*, 2015) and S wave (Idehara, 2011), respectively. The origin of ULVZs is highly controversial. A number of models have been suggested: Fe-enriched mantle minerals (e.g. Wicks *et al.*, 2010; Bower *et al.*, 2011; Wicks *et al.*, 2017); partial melts (e.g. Williams and Garnero, 1996; Thomas *et al.*, 2009; Yuan and Romanowicz, 2017) of the lowermost mantle; chemical reactions between the mantle and core (Buffett *et al.*, 2000); and melt derived by subducting slabs (Andrault *et al.*, 2014; Liu *et al.*, 2016). The partial

melt model is confronted with difficulties in explaining the detected ULVZs being away from or at least near the edge of presumably hotter lowermost mantle regions (Ross *et al.*, 2004; Xu and Koper, 2009; Yu and Garnero, 2018), the large low shear velocity provinces (LLSVPs). The LLSVPs are commonly interpreted to be hotter than the background mantle (e.g. Forte and Mitrovica, 2001), so if the ULVZs are of purely thermal origin, there should be more ULVZs within the LLSVPs than outside of the LLSVPs (Yu and Garnero, 2018). The recent observations of the locations of the ULVZs point to an independent origin of the ULVZs from the LLSVPs (Yu and Garnero, 2018).

1.2.2 Large Low Shear Velocity Provinces (LLSVPs)

The large seismic anomalies are found right above the CMB beneath the Pacific Ocean and south Africa. The LLSVPs are the two anomalously large structures at the bottom of the mantle, characterized by a few percent of the shear velocity reduction (Ishii and Tromp, 1999; Grand, 2002; Garnero *et al.*, 2016; Dziewonski *et al.*, 2010; Garnero and McNamara, 2008). The locations of the LLSVPs seem to be related to the distributions of the major geological sites at the surface (Burke *et al.*, 2008; Torsvik *et al.*, 2010). The hotspots and large igneous provinces (LIPs) are concentrated above the LLSVPs, which are interpreted as the surface features of the mantle plumes (Burke *et al.*, 2008; Torsvik *et al.*, 2010). The major subduction zones seem to be away from the LLSVPs. These relations are consistent with mantle dynamics studies that the mantle plumes derive from the LLSVPs margins (Tan *et al.*, 2011; Steinberger and Torsvik, 2012), implying that the LLSVPs would exert some control on the deep mantle dynamics.

However, the origin of the LLSVPs has been much debated for many years between purely thermal models (e.g. Schuberth *et al.*, 2009; Davies *et al.*, 2012, 2015) and

thermo-chemical models (e.g. Trampert *et al.*, 2004; Garnero *et al.*, 2016; Huang *et al.*, 2020). The LLSVPs exhibit several seismic characteristics, such as long-wavelength pattern, strong gradients in shear velocity at margins, density heterogeneity and anti-correlation of shear velocity and bulk sound velocity.

Bull *et al.* (2009) suggested that the thermo-chemical model matches tomography better in visual comparison than the purely thermal model, Davies *et al.* (2012), however, argued that the both models can explain equally well the length-scale of the LLSVPs. The sharp (strong gradients of shear velocity) margins of the LLSVPs are often interpreted as evidence for their distinctive chemical nature (Karato and Karki, 2001; Brodholt *et al.*, 2007) although local thermal gradients may explain such strong gradients of shear velocity without the chemical contribution (Davies *et al.*, 2012). The difference in density between the LLSVPs and the background mantle can provide important constraint on the chemical difference. However, the resolution of the density estimation remains debatable (Masters and Gubbins, 2003; Davies *et al.*, 2015).

Trampert *et al.* (2004) suggested that the LLSVPs are denser than the background mantle, and thus the chemical variation is necessary. More recently, Koelemeijer *et al.* (2017) argued that the LLSVPs may be less dense, which can be explained by thermal elevation if post-perovskite is stable. The existence of post-perovskite in the LLSVPs may be contradictory because of its positive clapeyron slope (Tsuchiya *et al.*, 2004b; Catalli *et al.*, 2009) which can stabilize post-perovskite only at sufficiently cold regions. Also, the stability of post-perovskite depends highly on chemical composition. In specific, Fe and Al, which are enriched in the crustal materials (Table 1.1), can deepen the lower boundary of the transition between Brg-post-perovskite, allowing the both phases to coexist above the CMB (Catalli *et al.*, 2009).

The low shear velocity anomalies are anti-correlated with the bulk sound velocity anomalies in the LLSVPs. The thermal model cannot explain the anti-correlation because high temperatures lower both P- and S-wave velocities (Davies *et al.*, 2015). Recent experiments by Greaux *et al.* (2019); Thomson *et al.* (2019) showed that the shear modulus of CaPv is substantially lower than previous predictions (e.g. Stixrude and Lithgow-Bertelloni, 2012). MORB contains a substantial amount of CaPv in the mineralogy in the lower mantle (∼30%; Ricolleau *et al.*, 2010). With their new shear modulus data, the shear velocity of MORB in the lowermost mantle would reduce significantly, and hence it can explain the anti-correlation of shear velocity and bulk sound velocity. Also, MORB is intrinsically denser than the background lower mantle (Hirose *et al.*, 2005; Ricolleau *et al.*, 2010), the accumulation of which seems like a possible scenario. However, previous geodynamic models predicted that MORB is difficult to accumulate at the base of the mantle due to its small thickness (∼7 km), which is readily entrained away by the mantle stirring (Li and McNamara, 2013).

Alternatively, primitive material that is substantially enriched in Si as well as Fe has been proposed (Deschamps *et al.*, 2012). On the one hand, the more Si there is in the composition, the more Brg can form, resulting in a larger enhancement in the bulk sound velocity than in the shear velocity. On the other hand, the more Fe there is in the composition, the higher the density. However, the origin of such composition remains uncertain. For example, a residue from magma ocean would have a high Si content, but the Fe content would be lower (Walter *et al.*, 2004b).

Collectively, the question whether the LLSVPs are thermal heterogeneities or thermo-chemical piles still remains. The density anomalies and the anti-correlation between shear velocity and bulk sound velocity seem to be in favor of the thermo-chemical model, while the long-wavelength pattern and strong gradients in shear velocity at margins can be explained by both models.

1.2.3 Sinking Behaviors of Subducting Slabs in the Deep Mantle

The descent of subducting slabs is an important mechanism associated with the flow dynamics and chemical heterogenieties of the deep mantle. Tomographic images have shown the different states of sinking behaviors of the subducting slabs in the Earth's mantle (e.g., Van der Hilst *et al.*, 1997; Fukao *et al.*, 2009). Beneath the subduction zones in the Western pacific, the subducting slabs are deflected horizontally for large distances (stagnation) near the topmost lower mantle (e.g., Van der Hilst *et al.*, 1997; Fukao *et al.*, 2009). Specifically, the subducting slabs in the Northern Honshu arc stagnate right above 670 km-depth, whereas those in Tonga and Kermadec arcs pass through the 670 km-depth and stagnate above 1,000 km-depth (e.g. Obayashi *et al.*, 2013). On the other hand, beneath the subduction zones in the Central and South America the subducting slabs seem to penetrate into the lower mantle with little or no stagnation.

The subduction (sinking) behavior is controlled not only by the mantle convection but by various kinds of forces: a slab pull, a ridge push, buoyancy and viscosity. A slab pull and a ridge push are the forces exerted by the slab (plate) itself. The subducting slab is pulled downward by its own weight, which may trigger the trench rollback (Schellart and Moresi, 2013), an oceanward migration (retreat) of a trench, possibly associated with the large-scale horizontal extent of the slab stagnation (Christensen, 1996; Goes *et al.*, 2017; Mao and Zhong, 2018). The continuous formation of the oceanic plate at mid ocean ridge naturally pushes away the existing plate on the surface and subducting slabs. The slab pull and ridge push are important driving forces for the subduction dynamics at shallow depths in the mantle (i.e. the upper mantle and the transition zone).

In deeper depths (i.e. the lower mantle), the effects of the slab pull and ridge push become less influential in the sinking behaviors of the subducting slab because of the increased effects of buoyancy and viscosity. The effects of buoyancy and viscosity become larger in deeper depths where the volume of the slab surrounded by the mantle becomes larger. Buoyancy is the force exerted on the subducting slab immersed in the surrounding mantle. Buoyancy can be described as a combination of chemical buoyancy caused by the density contrast and thermal buoyancy caused by the temperature difference with respect to the surrounding mantle. Viscosity is a resistance to flow, a property that determines the flow behavior. The sinking behavior of the subducting slab depends on the viscosity contrast with respect to the surrounding mantle.

1.2.4 The Effects of Buoyancy and Viscosity on the Slab Stagnation in the Shallow Lower Mantle

Density and viscosity abruptly increase at the boundaries of the mantle layers. But the greatest increase is found between the transition zone and the lower mantle (Dziewonski and Anderson, 1981). Ringwoodite (Rw), the most abundant mineral in the deep transition zone, transforms into Brg and Fp in the lower mantle with ∼15% increase in density (Duffy and Anderson, 1989) and 1-2 orders of magnitude increase in viscosity (Fei *et al.*, 2017). The sharp increases in the density and viscosity from the transition zone to the lower mantle should occur globally, but the subducting slabs seem to behave differently in the different regions (e.g., Van der Hilst *et al.*, 1997; Fukao *et al.*, 2009).

The subducting slabs are older in the West Pacific than in the Central and South America. The oceanic plates have much longer time on the surface to be cooled before arriving in the subduction zones in the West Pacific. The subducting slabs beneath

the West Pacific are colder than those beneath the Central and South America, resulting in the larger negative thermal buoyancy of the slabs. However, the subducting slabs beneath the West Pacific experience the stagnation near 670-1,000 km-depth, whereas those beneath the Central and South America seems to penetrate the topmost lower mantle (e.g., Van der Hilst *et al.*, 1997; Grand, 2002; Fukao *et al.*, 2009). This led to the investigations that the colder temperatures may have the opposite effects on the chemical buoyancy of the subducting slabs. The cold temperatures in subducting slabs can cause slow diffusion, which delays phase transformations, such as the meatastable transformation of olivine (Tetzlaff and Schmeling, 2000), and the pyroxene-garnet transformation (King *et al.*, 2015; Nishi *et al.*, 2013). The low-density minerals would persist in the subducting slab because of the delayed phase transformation, while the minerals in the surrounding mantle undergo the phase transformation into the higher-density minerals, resulting in the positive chemical buoyancy of the subducting slab.

In addition to buoyancy, viscosity plays an important role in the sinking behaviors of subducting slabs. Because of the colder temperatures, subducting slabs should be more viscous than the surrounding mantle. However, the viscosity structure of the mantle may be complex, affecting the sinking behaviors of the subducting slabs. Recently, Mao and Zhong (2018) argued that a significant viscosity reduction in a thin layer exists at the 670 km-depth beneath the Northern Honshu arc. They suggested that the less viscous layer can be stable as a result of the phase transformation from Rw to Brg at the 670 km-depth due to the grain-size reduction and superplasticity (Kubo *et al.*, 2000; Karato, 2012; Panasyuk and Hager, 1998). The subducting slabs would move horizontally along this layer, which appears to be the slab stagnation in the seismic tomography (Mao and Zhong, 2018).

Rudolph *et al.* (2015) showed an significant increase in the viscosity of the mantle at 1,000 km-depth, where the slab stagnation is observed beneath the Tonga and Kermadec arcs. Recent experiments suggested that Fe plays an important role in such increase of the viscosity at 1,000 km-depth (Shim *et al.*, 2017; Deng and Lee, 2017). Shim *et al.* (2017) show that the smaller amount of Fe in (Mg,Fe)(Al,Si)O_3 Brg can be responsible for such viscosity increase at ∼1,000 km-depth. They showed that Fe^{2+} becomes the dominant valence state of Fe in Brg at ∼1,100–1,700 km-depth, which preferentially partitions into Fp, reducing the amount of Fe in Brg. It is known that Fe reduces the melting temperature of silicate minerals in the upper mantle (Zhao *et al.*, 2009). If this is the case of Brg, the viscosity of Brg can be scaled to homologous temperature (the normalized temperature to the melting temperature; e.g. Yamazaki and Karato, 2001; Weertman and Weertman, 1975). The less amount of Fe in Brg would increase its viscosity at ∼1,100–1,700 km-depth (Shim *et al.*, 2017). Brg is not only the most abundant mineral in the lower mantle (∼70 vol%; e.g. Irifune *et al.*, 2010) but also the most viscous mineral in the lower mantle (Yamazaki and Karato, 2001; Ammann *et al.*, 2010; Girard *et al.*, 2015). Therefore, the viscosity of Brg would control the lower-mantle viscosity (e.g. Yamazaki and Karato, 2001; Ammann *et al.*, 2010).

Also, the transition of the spin state of Fe in (Mg,Fe)O Fp was proposed to explain the viscosity jump at ∼1,000 km-depth (Deng and Lee, 2017). They observed the anomalously high melting temperature of Fp at ∼1,000 km-depth, possibly caused by the spin transition of Fe^{2+} from the high state to the low state at ∼1,000-1,600 km-depth (Badro *et al.*, 2003; Speziale *et al.*, 2005; Fei *et al.*, 2007).

However, the viscosity change alone may not provide a complete explanation of why the subducting slabs behave differently in the different regions. The multiple factors described above, such as buoyancy, viscosity contrast, and trench rollback

need to be comprehensively taken into account in order to better understand the sinking behaviors of subducting slabs in the deep mantle (Torii and Yoshioka, 2007).

1.2.5 Sinking Behaviors of Subducting Slabs in Early Earth

Multiple lines of evidence indicate that subduction processes have occurred since 2.5–3.0 Ga (Condie and Kröner, 2008; Laurent *et al.*, 2014; Tang *et al.*, 2016). It is not well understood how the sinking behaviors of subducting slabs have changed over time. In the Archean (4.0–2.5 Ga), the mantle would have been much warmer by ∼200 K than in the present day (Korenaga, 2008; Herzberg *et al.*, 2010). The warmer mantle would have been less viscous, facilitating the sinking processes of the subducting slabs with less drag force (Billen, 2010). The previous studies suggested that the sinking of the subducting slabs would have been faster in the Archean because of the less viscous mantle and the large thickness of the slab, caused by the higher temperature of the mantle (van Hunen and van den Berg, 2008; Sizova *et al.*, 2010). van Hunen and van den Berg (2008) further predicted that the subducting slabs break off, resulting in the episodic style of subduction dynamics in the Archean if the slab strength is sufficiently weak (van Hunen and van den Berg, 2008; Van Hunen and Moyen, 2012).

However, the vigor of the mantle convection does not necessarily depend on temperature. The counter effect of the warmer mantle in the Archean is that the depleted lithosphere was thicker, reducing the surface heat flow (Korenaga, 2009, 2010). This can lead to the less vigor of the mantle convection (Korenaga, 2009, 2010). Furthermore, the mantle viscosity is sensitive to the water content as well as temperature (Karato and Wu, 1993; Hirth and Kohlstedf, 2003), which is not well known for the Archean mantle (Korenaga, 2018).

Some previous studies attempted to infer the water content of the Archean mantle from komatiites (e.g. Parman *et al.*, 2001). Komatiites are volcanic rocks that formed by unusually high-degree melting mostly in the Archean. Because of their ultramafic composition, komatiites are considered to form through either anhydrous melting of ∼200 K warmer (Nisbet *et al.*, 1993; Herzberg *et al.*, 2010) or hydrous melting of only ∼100 K warmer mantle than the present-day mantle (Parman *et al.*, 2001; Grove and Parman, 2004). Berry *et al.* (2008) suggested that komatiites would have formed through anhydrous melting at high temperatures based on the ferrous iron being dominant in komatiitic melt inclusions. Also, the field occurrence of komatiites is limited up to 10% of the total volume of volcanic rocks in most greenstone belts (De Wit and Ashwal, 1997). Thus, the water content of komatiite may not represent the water content of the Archean mantle (Korenaga, 2018).

On the other hand, the buoyancy of subducting slabs in the Archean has not been well constrained. Van Hunen and Moyen (2012) predicted that the subducting slabs in the Archean would be negatively buoyant because the larger fraction of the crust in the subducting slab is negatively buoyant, while the harzburgite layer remains neutrally buoyant. If the hazburgite layer did not stay coherently, delamination style of sinking crust might have occurred in the Archean (Davies, 1992; Capitanio *et al.*, 2010; Johnson *et al.*, 2014). However, this prediction was based on approximate estimations of density and thickness (Schutt and Lesher, 2006). The densities of the crust and the harzburgite layer in the Archean subducting slab need to be thoroughly examined for the depths near 670 km-depth where complicated sinking behaviors occur in the present day.

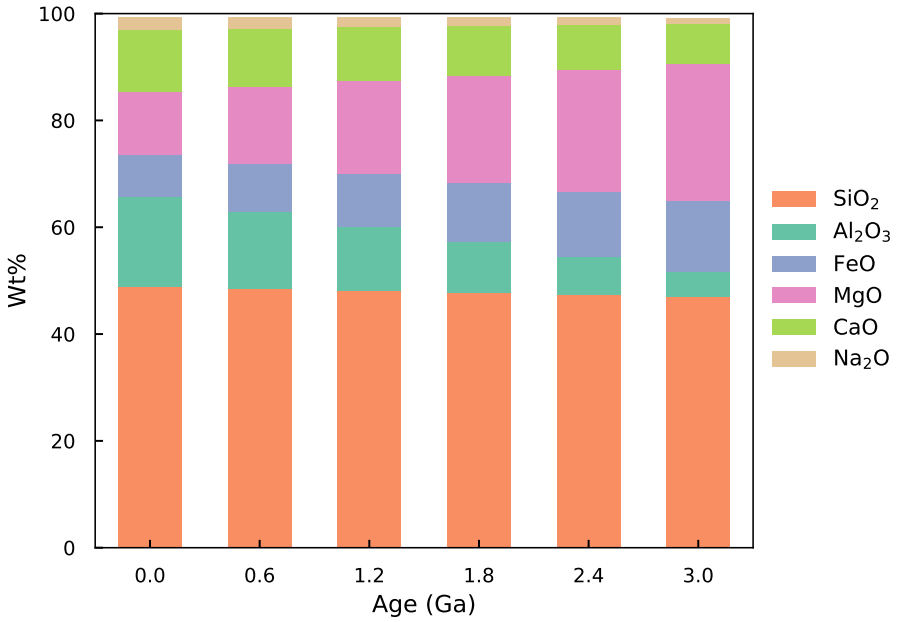

Figure 1.2: Chemical composition of primary melt as a function of time. The chemical compositions were obtained from Johnson *et al.* (2014).

1.2.6 The Compositional Evolution of the Volcanic Crust

The Volcanic crust forms through partial melting of the mantle near the surface and its composition and thickness depend on the mantle potential temperature (T_p) (Herzberg *et al.*, 2010). In early Earth, the higher T_p (up to ~200 K; Herzberg *et al.*, 2010) led to extensive partial melting of the mantle, increasing the maficity and thickness of the volcanic crust (Herzberg *et al.*, 2010).

Primary melt is the very first liquid when the mantle rock melts, the composition of which represents the starting composition of magma. Therefore, the composition of the primary crust can be derived from that of primary melt. Johnson *et al.* (2014) modeled a linear relation between the composition of primary melt and T_p (Age) (Fig. 1.2) based on the rock samples documented by Herzberg *et al.* (2010). In the model, the MgO content is the largest in the Archean (23 wt%; 2.5-3.0 Ga), decreasing

toward 8 wt% in the modern day (Table 1.1, Fig. 1.2). From this model (Johnson *et al.*, 2014), the chemical compositions of Archean (basalt formed 3.0 Ga; hereafter referred to as B30) and Proterozoic (basalt formed 1.5 Ga; hereafter referred to as B15) crusts were obtained and compared with modern MORB and pyrolite in Table 1.1.

Table 1.1: Chemical compositions of pyrolite, Archean volcanic crust (B30), Proterozoic volcanic crust (B15), and the present-day MORB.

wt%	Pyrolite[a]	B30[b]	B15[b]	MORB
SiO_2	45.1	47.0	48.1	51.8
Al_2O_3	4.8	7.5	12.7	15.5
FeO	8.4	12.7	9.2	10.1
MgO	37.7	22.8	17.8	8.0
CaO	3.5	8.8	10.4	11.7
Na_2O	0.4	1.3	1.8	2.1
(Mg+Fe+Ca)/Si	1.49	1.15	0.94	0.63

[a] McDonough and Sun (1995)

[b] Johnson *et al.* (2014).

†The compositions were normalized to 100%

For billions of years since the onset of subduction in the Archean (Condie and Kröner, 2008; Laurent *et al.*, 2014; Tang *et al.*, 2016), the sinking behaviors of subducting slabs would have been altered by the changes in composition and thickness of the crust. In the case of Archean volcanic crust, its composition contains much more Mg and Fe but less Si and Al than modern MORB (Fig. 1.2). The compositional difference produces the different mineralogy, which in turn leads to the different physical properties like density.

1.2.7 The Mineralogy and Density of Ancient Volcanic Crust in the Deep Mantle

The mineralogy of Archean volcanic crust is expected to be similar to that of pyrolite rather than modern MORB. The higher (Mg + Fe + Ca)/Si ratio of Archean volcanic crust (Table 1.1) would have formed (Ca,Mg,Fe)SiO_3 pyroxene/garnet and $(Mg,Fe)_2SiO_4$ olivine in the upper mantle, which transform into (Ca,Mg,Fe)SiO_3 majoritic garnet and $(Mg,Fe)_2SiO_4$ wadsleyite (Wd)/Rw in the transition zone, respectively (Nishihara and Takahashi, 2001; Klein *et al.*, 2017).

On the contrary, modern MORB includes pyroxene or garnet plus silica in the upper mantle and transition zone but no olivine and its polymorphs (Hirose *et al.*, 1999; Irifune *et al.*, 1986). The persistence of majoritic garnet in modern MORB at 700-800 km-depth (Hirose *et al.*, 1999) can make the subducting slab buoyant, whereas the mineralogy of Archean volcanic crust may include Rw, which transforms into the high-density mineral, Brg, at around 670 km-depth (Nishihara and Takahashi, 2001; Klein *et al.*, 2017).

The larger content of Fe in Archean volcanic crust would make the Rw-Brg transformation at the shallower (Ito and Takahashi, 1989) depth than that in pyrolite. The density of Archean volcanic crust would become greater than the surrounding mantle, resulting in the negative chemical buoyancy, unlike modern MORB at the topmost lower mantle (Klein *et al.*, 2017).

Because of the larger thickness, Archean volcanic crust (∼45 and 7 km, respectively) would have played a larger role in the sinking behaviors of subducting slabs than moden MORB does in the present day. In other words, a proportion of the crust in a subducting slab is much larger in the Archean than in the present day, thus the density of the crust becomes more influential in the chemical buoyancy of the subducting slab.

As discussed in Chapter 1.2.3, buoyancy and viscosity are the key parameters acting on the sinking behaviors of subducting slabs. The varying composition and thickness of the volcanic crust over time could have altered the sinking behaviors of subducting slabs. In the present day, the buoyancy (e.g. Irifune and Ringwood, 1987a; Hirose *et al.*, 1999, 2005; Ricolleau *et al.*, 2010) and the viscosity contrast (e.g. Marquardt and Miyagi, 2015; Torii and Yoshioka, 2007) of the subducting slabs with respect to the surrounding mantle have been widely studied. However, those in ancient eons (Archean and Proterozoic; 0.5–3 Ga) are poorly understood because of a paucity of evidence.

Herzberg *et al.* (2007, 2010) made great efforts to link the relation between the age and chemical composition of the volcanic crust based on natural rock samples of non-arc basalt. The better constraints on the chemical composition of the volcanic crusts enabled us to explore the sinking behaviors of the ancient volcanic crusts. Klein *et al.* (2017) calculated the density of Archean volcanic crust, suggesting that Archean volcanic crust is negatively buoyant in the Archean transition zone. However, their calculated mineral assemblages of Archean volcanic crust contradicts our current knowledge of the mineralogy in the deep mantle. For example, they reported the coexistence of (Mg,Fe)O Fp and SiO_2 St in the conditions of the transition zone (Klein *et al.*, 2017), which indicates that their mineralogical model might not have reached its thermodynamic equilibrium.

As part of my PhD study (Chapter 4,5), I adopted experimental approaches to examine the mineralogy and density of the volcanic crustal rocks in the Archean and Proterozoic deep mantle. Combined with modern MORB, which has been extensively examined by previous experiments (e.g. Hirose *et al.*, 1999, 2005; Ricolleau *et al.*, 2010), this study on the Archean and Proterozoic volcanic crusts (B30 and B15,

respectively) will provide insights on how the compositional evolution of the volcanic crust for ∼3 billion years has affected the chemical evolution of the mantle.

1.2.8 The Mineralogy of the Si-rich Mantle

The mineralogy for various possible mantle compositions in rocky exoplanets has not well been explored although the ratio of Mg/Si for exoplanets based on the stellar elemental abundance may widely range from <0.9 to >2.0 (Hinkel *et al.*, 2014; Young *et al.*, 2014). The ratio of divalent cations (Mg + Fe + Ca) to Si can describe the lower mantle mineralogy. Depending on (Mg + Fe + Ca)/Si, the lower-mantle mineral assemblages consist of the combination of the four major phases: (Mg,Fe)SiO_3 Brg, (Mg,Fe)O Fp, $CaSiO_3$ CaPv, and SiO_2 stishovite (St). For example, in the lower mantle conditions, if (Mg + Fe + Ca) > Si, Fp could form together with Brg and CaPv, whereas St could form instead of Fp if (Mg + Fe + Ca) < Si. If (Mg + Fe + Ca)=Si, neither Fp or St would form, but only Brg and CaPv can be stable. However, this simple estimation does not consider the trivalent cations, such as Fe^{3+} and Al^{3+}, which can substitute the divalent cations of Si^{4+} in Brg. Also, the $3Fe^{2+}$ can form $2Fe^{3+}$ alongside metallic Fe through the charge disproportionation reaction (Frost *et al.*, 2004) in Brg, which can alter the mineralogy of the lower mantle.

As discussed in Chapter 1.2, the pyrolitic composition forms Brg, Fp, and CaPv in the lower mantle conditions with the ratio of (Mg + Fe + Ca)/Si=1.49. The higher ratio of (Mg + Fe + Ca)/Si will only add more Fp to the pyrolite mineralogy. However, it is uncertain whether the lower ratio of (Mg + Fe + Ca)/Si∼1 forms Fp or St. The presence of the secondary phase of either Fp or St may have a significant impact on the physical properties of the mantle, such as viscosity. The experiments on the B30 composition at the high P–T conditions can provide some insights into the mineralogy of the Si-rich mantle for rocky exoplanets.

1.3 Overview of the Dissertation Chapters

1.3.1 Chapter 3: Incorporation of Calcium into Bridgmanite in the Earth's Lower Mantle

The mineralogy of the Earth' lower mantle has been believed to be Brg, Fp, and CaPv in most depths of the lower mantle (Irifune *et al.*, 2010; Ishii *et al.*, 2018). However, I have found that Ca may dissolve into Brg in the deep lower mantle where temperature is above 2,250 K, forming the simpler mineral assemblage (Brg and Fp only as major phases). If this indeed occurs in the Earth's deep lower mantle, two different mineral assemblages may exist: Brg (Mg-Brg), Fp, and CaPv in the shallow lower mantle (SLM); Ca-bearing Brg (Ca-Brg) and Fp in the deep lower mantle (DLM). Also, the thickness of the DLM layer might have been larger in the past when the mantle was hotter because of the temperature-dependent Ca dissolution in Brg. The Ca dissolution in Brg and the absence of CaPv in the DLM may have a profound impact on the compressibility and viscosity of the DLM.

1.3.2 Chapter 4: The Mineralogy and Density of the Volcanic Crust near 670 km-depth in the Archean Deep Mantle

Seismic tomography shows the descent of the subducting slabs into the lower mantle beneath some subduction zones (e.g., van der Hilst and Seno, 1993; Fukao *et al.*, 2009; Li and McNamara, 2013; King *et al.*, 2015), in favor of the whole-mantle convection. However, the evolution of the mantle convection has been poorly understood due to the limited knowledge on the scale of the mantle convection in early Earth. I have investigated the mineralogy and density of Archean volcanic crust in order to evaluate the chemical buoyancy near 670 km-depth (the deep transition zone and topmost lower mantle). My experiments showed that Archean volcanic crust would

have been denser than the surrounding mantle, promoting further sinking into the lower mantle. Also, I calculated the harzburgite layer of the subducting slab. The net density of the subducting slab in the Archean is denser than or at least the same as the surrounding mantle, decreasing the likelihood of the slab stagnation in the Archean. These results suggest the negative buoyancy of the Archean subducting slabs, promoting the whole-mantle convection in the Archean.

1.3.3 Chapter 5: The Mineralogy and Density of the Ancient Volcanic Crusts in the Earth's Lower Mantle

The large low shear velocity provinces (LLSVPs) at the bottommost lower mantle may be chemically distinctive from the lower mantle (e.g. Trampert *et al.*, 2004; Deschamps *et al.*, 2012). However, its origin still remains enigmatic. I have investigated whether they could have sunken to the base of the mantle and have accumulated in the region. I have measured the densities of the ancient volcanic crusts (B30 for the Archean; and B15 for the Proterozoic, respectively) in the lower-mantle pressures and temperatures. My experimental results show that the ancient volcanic crusts are denser than the surrounding lower mantle by up to 3%. The ancient volcanic crusts would have survived the vigorous mantle stirring because of the large thickness (up to 40 km), unlike modern oceanic crust (7 km) which could be too thin to accumulate (Li and McNamara, 2013). Therefore, the ancient crusts should be considered viable candidates for the chemical origin of the LLSVPs at the base of the mantle.

Chapter 2

GENERAL METHODOLOGY

2.1 Diamond Anvil Cell

The diamond anvil cell (DAC) technique has been widely used to solve the problems in the deep interiors of Earth and other rocky planets. Diamond is one of the hardest materials on Earth, which makes it suitable for high pressure experiments. The DACs are capable of generating the static compression up to 400 GPa in a conventional setup (Li *et al.*, 2018), which exceeds the pressure at the center of the Earth. Another key feature of diamond is the transparency across a broad range of the electromagnetic spectrum. Diamond allows the electromagnetic radiations, such as X-rays, gamma-rays, and infrared radiations, to pass through and interact with the sample material directly. When these radiations hit the sample, they either get diffracted, absorbed, or scattered, which provide information about the properties of the sample material.

In the typical DAC setup, two diamonds sandwich a gasket where the sample chamber is located (Fig. 2.1). The sample chamber is laser-drilled cylinder hole with 20 μm in thickness and 90–260 μm in diameter. Sample is prepared as a pre-compressed foil ($\sim$10 μm thick). The sample foil is inserted in the sample chamber in the gasket using the micro-manipulator. The micro-manipulator is equipped with a robot arm that is fully operated by a computer software with a micrometer precision. The tiny particles ($\sim$5 μm) of the sample material are placed as spacers at the corners between the sample foil and the diamonds on the both sides. This way, the empty space is created between the sample foil and the diamonds, which is filled up by

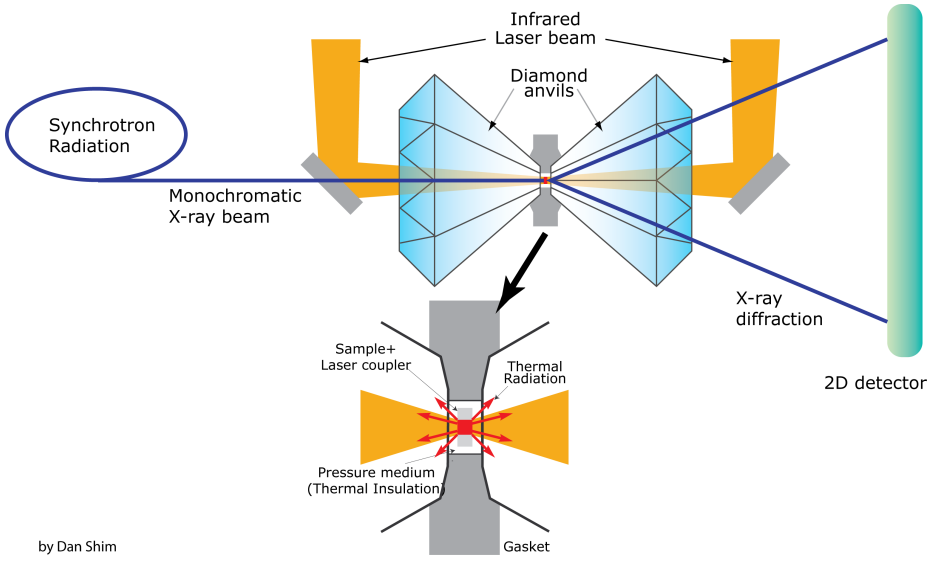

Figure 2.1: Schematic image of the synchrotron X-ray diffraction in a diamond anvil cell. Image Credit: Sang-Heon Dan Shim, ASU.

gaseous or liquid pressure medium that transmits the hydrostatic pressure to the sample.

The pressure is increased by the symmetrically-located four screws in the DAC (Fig. 2.2). To minimize the possible differential stress, an incremental pressure was increased at a time by a pair of the screws that are located across the DAC center, then by the other pair, and so on, until I reach the target pressure. In some cases, I used a gas membrane can, that encloses and compressed a DAC by gas pressure.

2.1.1 Pressure Determination and Equaition of State

The sample pressure is determined with a pressure calibrant, Au. Au powder is mixed with the sample material before being compressed into a foil. The X-ray diffractions (XRDs) of Au are measured together with those of the sample. The details about the XRD measurements will be described in Chapter 2.2. The pressure of the sample was measured using the equation of state (EOS) of Au (Dorogokupets

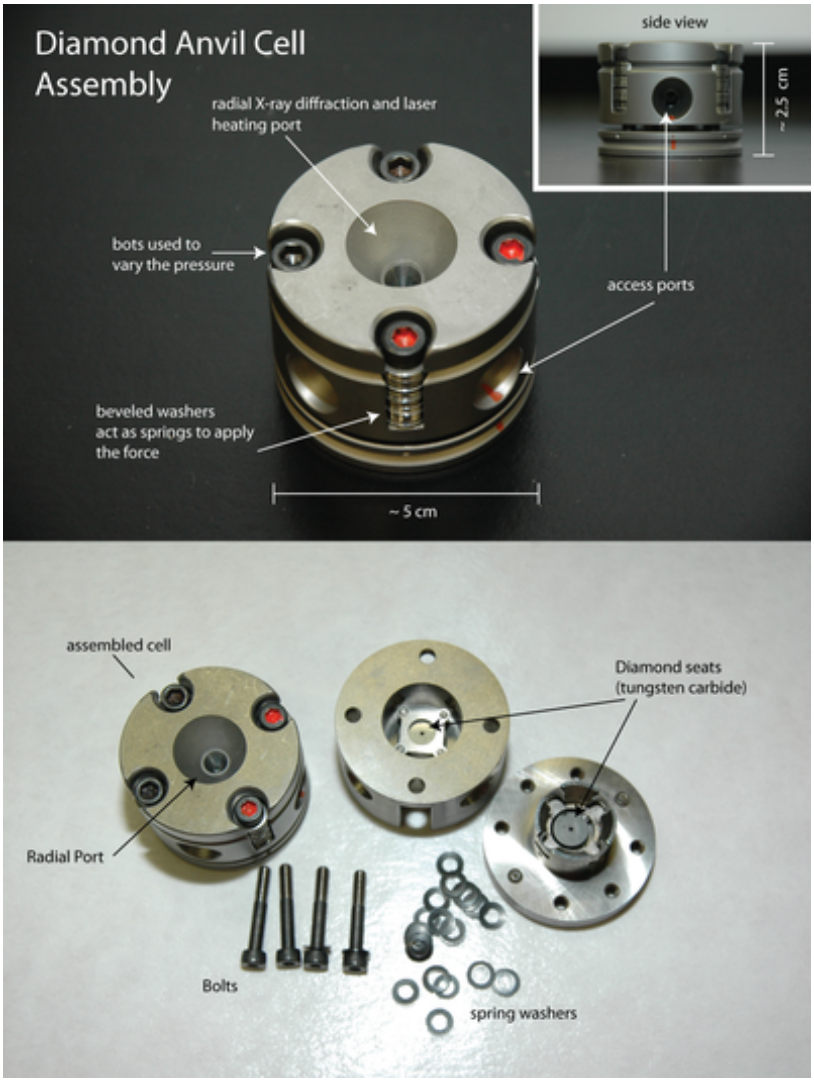

Figure 2.2: Pictures of a diamond anvil cell assembly. Image Credit: Lavina and Burnley, UNLV.

and Dewaele, 2007) based on the measured volume of Au. The static pressure was calculated using the Vinet EOS (Vinet *et al.*, 1987):

$$P_{300K} = 3K_0 \left(\frac{V}{V_0}\right)^{-\frac{2}{3}} \left[1 - \left(\frac{V}{V_0}\right)^{\frac{1}{3}}\right] \exp\left\{1.5(K_0^{'} - 1) \cdot \left[1 - \left(\frac{V}{V_0}\right)^{\frac{1}{3}}\right]\right\}$$

where P_{300K} is pressure at 300 K, K_0 is bulk modulus at 300 K, V is volume at P_{300K}, V_0 is volume at 1 bar and 300 K, and $K_0^{'}$ is a pressure derivative of K_0. For in-situ experiments at high P–T conditions, the thermal pressure P_{th} was additionally calculated using the Mie-Grüneisen relation:

$$P_{th} = \frac{\gamma}{V}[E(T, \theta_D) - E(300\,K, \theta_D)]$$

with the Grüneisen parameter:

$$\gamma = \gamma_0 \left(\frac{V}{V_0}\right)^q$$

where γ_0 is the Grüneisen parameter at V_0, q is the volume dependence, and $E(T, \theta_D)$ is the Debye temperature. The harmonic internal energy, $E(T, \theta_D)$ can be calculated from Debye model as follows:

$$E(T, \theta_D) = 9nRT \left(\frac{T}{\theta_D}\right)^3 \int_0^{\frac{\theta_D}{T}} \frac{x^3 dx}{e^x - 1}$$

where θ_D is assumed to be:

$$\theta_D = \theta_0 \left(\frac{V}{V_0}\right)^{-\gamma}$$

where θ_0 is the Debye temperature at V_0. In addition, the pressure calculations can be done easily by using a python package Pytheos (Shim, 2017b).

2.1.2 Temperature Measurements

Just like other electromagnetic radiations, laser can pass through diamonds. The laser heated diamond anvil cells (LHDACs) can increase the temperature by focusing

the laser beams from the both sides of the two diamonds. In LHDACs, I could reach temperature up to 4,000 K at the focused area in the sample with the beam diameter of $\sim$20 μm. The thermal radiation spectra measured from both sides of the sample were fit to Planck gray-body equation for the temperature estimation. Then, the two measured temperatures were averaged with an error range as the difference between them. In many runs, I employed the 'hop' method to apply the target temperature to the target area instantly, such that the target area will not experience the temperatures lower than the target temperature. The advantage of this method is that the target area can avoid the undesired kinetics at the lower temperature if temperature is gradually increased to the target temperature. I increased the laser power until the target temperature at the pre-heated area, then I moved the sample instantly, such that the fresh target area is immediately exposed to the high-power laser. This way, I have a better control on temperature especially for the experiments sensitive to temperature.

2.2 X-ray Diffraction

X-ray diffraction (XRD) is a foundational technique to identify the phases stable at certain P–T conditions during in-situ or ex situ experiments. For in-situ, synchrotron provides the powerful monochromatic X-ray that enables me to measure a XRD pattern in only seconds or minutes.

When the X-ray wave hits the sample it's diffracted by the lattice planes of the crystal structure of the sample material (Fig. 2.3). The distance between the parallel lattice planes is called d-spacing. In the synchrotron set up used in this study, the angle-dispersive XRDs are recorded as 2θ (angle) in the 2-dimensional detector. The 2θ depends on the energy of the incident X-ray and the d-spacing of the lattice plane where X-ray is diffracted (Equation 2.2). Typically, a number of XRDs are

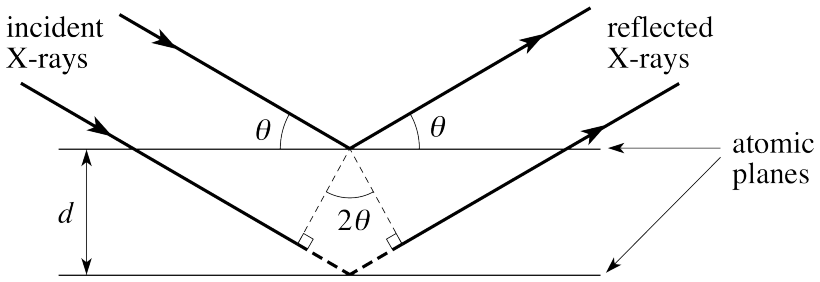

Figure 2.3: Schematic image of the X-ray diffraction. Image Credit: University of Reading (URL `http://www.met.reading.ac.uk/pplato2/h-flap/phys7_1.html`).

generated from the multiple sets of the lattice planes of a crystal structure(s) that have different d-spacings. The XRD pattern can characterize the crystal structures of materials. By analyzing the 2θ angles of the XRD pattern, the d-spacings of the sets of the lattice planes can be identified. For polycrystallin materials, the XRD peaks are generated by the constructive interference when Bragg condition is satisfied. The following equation, Bragg's law, describes how Bragg condition on θ for the constructive interference to be at its strongest:

$$2d\sin\theta = n\lambda$$

where d is d-spacing, n is a positive integer, and λ is the wavelength of the incident wave. Assuming the random crystallogaphic orientation of the polycrystalline material, the diffractions off the various lattice planes will interfere destructively if Bragg condition is not satisfied. These diffractions will cancel out one another's intensities and remain as the background. Only the diffractions at θ that satisfies Bragg condition will stack (the constructive interference) and generate the observable XRD peaks (Bragg peaks). The 2-dimensional XRD patterns are collected and integrated into 1-dimensional patterns in the DIOPTAS software (Prescher and Prakapenka, 2015). Then, the XRD patterns can be analyzed using a python software PeakPo (Shim, 2017a) and Rietveld refinements in GSAS-II (Toby and Von Dreele, 2013).

2.3 Chemical Analysis

After the LHDAC experiments, the samples are recovered from the DACs by using the micro-manipulator. The recovered samples are placed onto the copper tape of the stub. The stub is coated with carbon for imaging in the focused ion beam (FIB). I use the lift-out method with the FIB to extract the heated area in the sample and to mount it on the copper grid. Then, the sample is thinned to the thickness of 50-100 nm with the Ga ion milling.

I analyze the chemical compositions of the thinned sample by using the scanning transmission electron microscopy (STEM) combined with the energy dispersive X-ray spectroscopy (EDS). The STEM is a powerful tool that is capable of focusing the electron beam into the atomic scale of 1 Å.

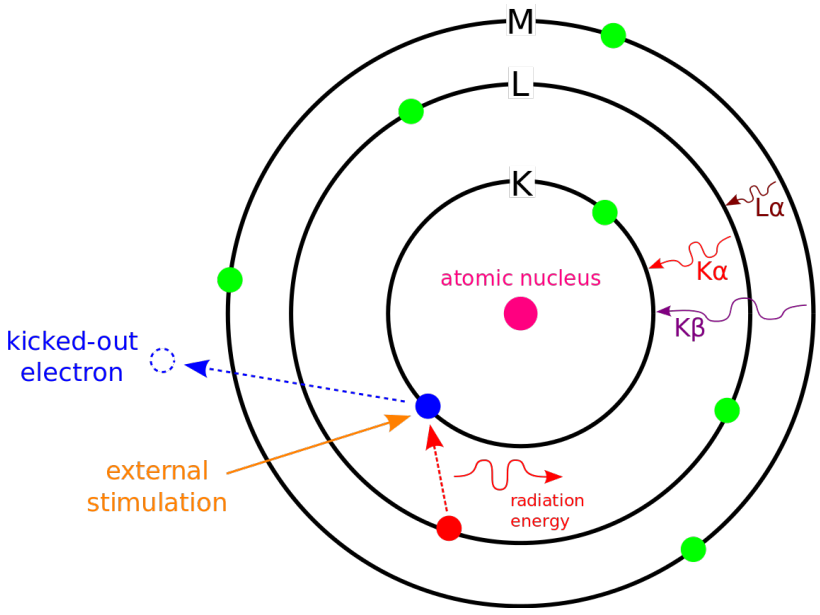

Figure 2.4: Schematic image of the generation of the characteristic X-ray. Image Credit: Muso (URL: `https://en.wikipedia.org/wiki/Energy-dispersive_X-ray_spectroscopy#/media/File:EDX-scheme.svg`).

The EDS technique uses the highly focused electron beam of the STEM to stimulate the characteristic X-rays from the atoms of the sample material. The incident beam can excite an electron in an inner shell of an atom depending on the beam energy (Fig. 2.4). The excited electron is ejected from the inner shell, creating an electron hole. Then, another electron in the outer shell immediately migrates into the electron hole in the inner shell to fill it up. When this migration occurs, the X-ray is generated with the energy that is equivalent to the energy difference between the inner and outer shells. Because the energy of the generated X-ray is the characteristic of the element, I can identify the elements of my sample by indexing the energies of the X-rays from the collected spectra. More importantly, I can measure the atomic fraction of each element by counting the number of the X-rays in the energy spectra.

Elements that have higher atomic number (Z) have the more number of shells, therefore they generate the multiple X-rays from one atom (Fig 2.4). For example, Fe has K-, L-, and M-shells in an order of the distance from the nucleus. The X-ray generated by the electron migration from the L-shell to the K-shell is called Kα, that from the M-shell to the K-shell is called Kβ, and that from the M-shell to the L-shell is called Lα.

For the quantitative analysis, I only consider Kα of O, Mg, Al, Si, Ca, and Fe in an order of the characteristic X-ray energy. These elements are the major elements of the Earth's mantle minerals and my samples. After background is subtracted, the following equation, Cliff-Lorimer method, is used to calculate the relative abundance of the elements:

$$\frac{\mathrm{C}_A}{\mathrm{C}_B} = k_{AB}\frac{\mathrm{I}_A}{\mathrm{I}_B}$$

where C_A and C_B are the atomic (or weight) concentrations of the element A and B, respectively, I_A and I_B are the X-ray intensities of the element A and B, respectively, and K_{AB} is Cliff-Lorimer sensitivity facor (k-factor).

First, I measure the elemental abundances of the standard material whose composition is already known, in order to obtain the k-factors for each element. After the k-factors are acquired, I measure the elemental abundances of the samples. The X-ray intensities are calculated from the areas of the peaks in the EDS spectra, which were fitted using a python code LMFIT (Newville *et al.*, 2016). The measured chemical compositions of my samples typically show $\sim$10% of an error range.

Chapter 3

INCORPORATION OF CALCIUM INTO BRIDGMANITE IN THE EARTH'S LOWER MANTLE

3.1 Introduction

The major phases of the Earth's lower mantle have been suggested to stay similar in most depths in the lower mantle: bridgmanite (Brg), ferropericlase (Fp), and $CaSiO_3$ perovskite (CaPv) in order of abundance (e.g. Ricolleau *et al.*, 2009; Irifune *et al.*, 2010). Ca^{2+}, the largest cation among the major cations in the lower mantle (1.34 Å for 12 coordination), has been believed to exist in the 12-coordinated site (A site) of the cubic perovskite structure of CaPv. The smaller cations of Mg^{2+} and Fe^{2+} (0.86 and 0.92 Å, respectively for 12 coordination) preferentially partition into the 8- or 12-coordinated site (A site) of the orhorhombic perovskite structure of Brg.

Many previous studies have supported the existence of CaPv (e.g. Hirose *et al.*, 2005; Irifune *et al.*, 2010; Ricolleau *et al.*, 2009) in the pressure and temperature (P–T) conditions of the lower mantle. But notable exceptions have been intermittently reported by several experiments (Lee *et al.*, 2004; Ono *et al.*, 2005; Sinmyo and Hirose, 2013). Lee *et al.* (2004) examined pyrolite in a range of pressure of 24–107 GPa at 2,250 ± 250 K and could not observe CaPv above 65 GPa in the X-ray diffraction patterns. Ono *et al.* (2005) observed CaPv along with Brg and Fp at 28 GPa and 2,050 K and 97 GPa and 2,100 K, but could not resolve the existence of CaPv in the X-ray diffraction patterns at 35 GPa and 2,100 K and 58 GPa and 2,250 K. Sinmyo and Hirose (2013) also could not find CaPv in peridotitic composition 110 GPa and 2,300 K, while the recovered sample showed Brg with the high Ca# (0.05) in the

chemical analysis. In the relatively lower P–T conditions (28 GPa and 1,900 K and 82 GPa and 2,100 K), they did observe CaPv in the synthesized mineralogy. The reported absence of CaPv may indicate the Ca dissolution in Brg because the other major phase, Fp, has no capability of incorporating such large cation in the structure that has only the 6-coordinated sites. Also, it seems to occur at the higher P–T conditions in these studies, suggesting the pressure- or temperature-dependence of the Ca dissolution in Brg.

However, the majority of the other experiments of the lower-mantle mineralogy have focused on temperatures close to the mantle geotherm in 20–115 GPa (Irifune *et al.*, 1994, 2000; Hirose, 2002; Nishiyama and Yagi, 2003; Nishiyama *et al.*, 2004; Ono *et al.*, 2004; Lee *et al.*, 2004; Ono *et al.*, 2005; Kubo *et al.*, 2008; Sanehira *et al.*, 2008; Ohta *et al.*, 2008; Ricolleau *et al.*, 2009; Sinmyo *et al.*, 2011; Sinmyo and Hirose, 2013). Only a few data points is available for higher temperatures (>2,400 K at >40 GPa) from the existing literature (Ono *et al.*, 2004; Ohta *et al.*, 2008). If the mineralogy changes depending on temperature, the mineralogal structure of the lower mantle may be complicated than expected. Also, the time-dependent changes in the mineralogy of the lower mantle would be important to understand as Earth's mantle cools over time (e.g. Korenaga, 2008). Therefore, a wider range of temperatures at the lower-mantle related pressures is worthwhile to explore in order to verify the temperature-dependent mineralogy caused by the Ca dissolution in Brg.

The change in the mantle mineralogy will change the properties of the mantle, such as the compressibility and viscosity. In the lower mantle, Brg is the most abundant mineral (∼80 vol%; Irifune *et al.*, 2010), and thus the properties of the lower mantle mantle depend primarily on those of Brg. If Brg incorporates Ca in the lower mantle, the effects of Ca on Brg as well as the absence of CaPv may have a significant impact on the compressibility and viscosity of the lower mantle.

Here, I report the experimental results of the stability of Ca-bearing bridgmanite (referred to as Ca-Brg hereafter) at the P–T conditions of the deep lower mantle. I conducted experiments on pyrolitic compositions using the laser-heated diamond anvil cell (LHDAC) combined with the in-situ X-ray diffraction technique at 38–108 GPa and 1,800–3,000 K. The unit-cell parameters of Ca-Brg and Ca-low bridgmanite (referred to as Mg-Brg hereafter) were compared at 300 K to reveal the effects of Ca on the lattice structure of Ca-Brg. In addition, the chemical compositions of the recovered samples were measured to examine the possible Ca dissolution in Brg.

3.2 Experimental Methods

3.2.1 Starting Material

I used 3 different starting compositions (Table 3.1). The first composition is Ca-enriched pyrolite (referred to as Ca-pyrolite hereafter), which is a mixture of pyrolite glass (McDonough and Sun, 1995) and $CaSiO_3$ glassa. The increased amount of Ca enhances the detectability of CaPv in X-ray diffraction patterns if it forms. Ca-pyrolite was used to investigate the stability of Ca-Brg in the P–T field. Also, the unit-cell parameters of the phases in Ca-pyrolite were measured at high pressures and 300 K. In addition to Ca-pyrolite, Ca#10Fe#10 composition ($Ca_{0.1}Mg_{0.8}Fe_{0.1}SiO_3$) was prepared as a single glass to examine whether Ca-Brg forms without the Al content in the composition. Ca#10Fe#10 composition was also used for investigating the P–T stability of Ca-Brg.

Lastly, I prepared glass with the komatiitic composition (Herzberg *et al.*, 2010; Johnson *et al.*, 2014). The komatiitic composition contains much less Mg than pyrolite and would not form Fp in the lower-mantle related conditions because of the ratio of (Mg + Fe + Ca)/Si is close to 1. Therefore, the komatiitic composition would

be a useful composition to eliminate any possible influence of Fp on the solubility of Ca in Brg. The synthesis experiments were performed with the komatiitic glass. I measured the unit-cell volumes of the synthesized phases and analyzed the chemical compositions of the recovered samples.

I confirmed the homogeneous compositions of the starting materials in an electron probe micro analyzer (JEOL JXA-8530F EPMA) combined with wavelength-dispersive X-ray spectrometer (WDS) at Arizona State University (ASU).

Table 3.1: Chemical compositions of starting materials. After excluding minor elements, I normalized each composition to 100 mol%.

mol%	Ca-pyrolite[a]	Komatiitic[b]	Ca#10Fe#10
SiO_2	41.2	44.1	50.0
Al_2O_3	2.2	4.2	0.0
FeO	4.6	9.9	6.4
MgO	43.0	31.8	40.0
CaO	9.1	8.8	5.0
Na_2O	0.0	1.2	0.0

[a] Additional $CaSiO_3$ was added to pyrolite composition from McDonough and Sun (1995)

[a] Johnson *et al.* (2014)

3.2.2 Laser-heated Diamond-anvil Cell Preparation

The starting materials were powdered and mixed with ∼10 wt% of Au powder (grain size of 1–3 μm) that served as a pressure standard and laser absorber in laser-heated diamond-anvil cell (LHDAC) experiments. The mixture was compressed to

thin foils with a thickness of ∼10 μm. I loaded a sample foil into a sample chamber, a pre-indented hole in a rhenium gasket, using a micro-manipulator (Microsupport Axis Pro SS) at ASU. Four spacers (<10 μm sized pure sample particle) were placed between the sample foil and each side of the diamond culets for gas or liquid medium loading. I used Ne, Ar or NaCl as a pressure medium that also served as a thermal insulator. For a NaCl solid medium, the NaCl powder was dried at 120°C for 4 hours and loaded into the sample chamber without spacers. I cold-compressed the samples in the symmetric-type diamond-anvil cell with 150–400 μm-sized culet before the laser heating.

3.2.3 X-ray Diffraction Measurements in Laser-heated Diamond Anvil Cell

I have conducted LHDAC experiments combined with in-situ X-ray diffraction (XRD) at sector 13-IDD of the GeoSoilEnviroConsortium (GSECARS) in the Advanced Photon Source (APS; Prakapenka *et al.*, 2008). The pressure and temperature ranges of the experiments were 38–108 GPa and 1,800–3,000 K, respectively. I provide the run table for the in-situ experiments in Table 3.2. The cold decompression measurements for sample #1208 were conducted at sector 12.2.2 in the Advanced Light Source (ALS). I measured diffraction patterns with monochromatic X-ray beams of 0.3344, 0.4133, and 0.4959 Å for the GSECARS and 0.4971 Å for the ALS. For the in-situ experiments, I focused the laser beams on both sides of the sample and aligned the laser beams coaxially with the X-ray beam by the visual observations of the X-ray fluorescence in order to measure XRD patterns at the center of the laser heating spot. The typical beam diameters for X-ray and laser were ∼5 and 20 μm, respectively. I fit the thermal radiation spectra measured from both sides of the sample to Planck gray-body equation for the estimation of temperature.

The diffraction images were collected using a MarCCD or a Dectris Pilatus detector in the GSECARS and a MarCCD in the ALS. The exposure time was 5–10 seconds and 300 seconds at 1 bar in the GSECARS and 120–300 seconds in the ALS. I integrated the collected images to 1-D diffraction patterns with the calibration parameters obtained from the LaB_6 standard in the DIOPTAS software (Prescher and Prakapenka, 2015). The diffraction patterns were analyzed and fitted with a pseudo-Voigt profile function to obtain the peak positions in the PeakPo software (Shim, 2017a). The unit-cell parameters were measured using the UnitCell software (Holland and Redfern, 1997), the Peakpo software, and Rietveld refinement GSAS-II (Toby and Von Dreele, 2013). I determined pressures with the equation of state (EOS) of Au (Dorogokupets and Dewaele, 2007) using the Pytheos software (Shim, 2017b).

For the P–T stability experiments, an area with a diameter of $\sim$20 μm was heated for up to 8 minutes for each heating cycle (Table 3.2). The locations of heating spots were chosen with an enough distance of 20–30 μm from the previously heated areas in order to start a new heating cycle with unheated fresh areas. For the synthesis experiments, the entire sample was scanned with the laser to ensure the complete synthesis of the sample for the chemical analysis afterwards.

From in-situ XRD patterns, I have observed that the glass samples transformed into crystalline phases within 1–60 seconds depending on temperature. Once crystalline phases formed, the XRD peak intensity gradually grows without a significant change in the further heating. In most runs for the P–T stability experiments, I first increase the laser power at a previously heated spot until a target temperature is reached, and then translated the sample position instantly such that the same laser power can be directly applied to a unheated, fresh spot. This heating method

helps preventing the target spot from undergoing the low-temperature kinetics when temperature is increased gradually from low to high.

Table 3.2: Run Table for the P–T Stability

Run No.	Data No.	Composition	Medium	Heating duration	Au V (Å)	P (GPa)	P_err (GPa)	T (K)	T_err (K)	Phase assemblage
3930	24	Ca#10/Fe#10	NaCl	01:34	59.88	42.15	0.64	2201	100	Brg+CaPv
3930	42	Ca#10/Fe#10	NaCl	00:53	59.77	40.21	0.96	1807	100	Brg+CaPv
3930	54	Ca#10/Fe#10	NaCl	01:14	59.77	41.17	0.67	1955	100	Brg+CaPv
3930	72	Ca#10/Fe#10	NaCl	03:14	60.85	39.30	0.66	2526	100	Brg
4833	25	Ca-pyrolite	NaCl	01:22	55.60	70.90	0.70	2219	100	Brg+CaPv
4833	30	Ca-pyrolite	NaCl	00:20	55.36	70.66	0.65	1869	100	Brg+CaPv
4833	36	Ca-pyrolite	NaCl	03:32	54.51	82.46	1.74	2548	278	Brg
4833	44	Ca-pyrolite	NaCl	02:34	55.24	76.74	1.34	2668	200	Brg
4833	52	Ca-pyrolite	NaCl	02:10	55.45	77.10	1.61	3022	170	Brg+Fp
4833	63	Ca-pyrolite	NaCl	08:24	54.50	83.34	1.55	2675	200	Brg
4901	30	Ca-pyrolite	NaCl	05:49	52.19	107.30	1.19	2691	190	Brg+Fp
4901	37	Ca-pyrolite	NaCl	05:43	52.68	99.33	1.91	2306	120	Brg+Fp
4901	53	Ca-pyrolite	NaCl	03:38	53.33	90.07	0.72	1932	100	Brg+Fp+CaPv
4901	62	Ca-pyrolite	NaCl	02:21	53.12	93.55	1.56	2130	200	Brg+CaPv
4901	67	Ca-pyrolite	NaCl	03:38	53.00	99.41	1.33	2861	180	Brg+CaPv
4901	73	Ca-pyrolite	NaCl	03:22	52.27	106.25	1.63	2655	261	Brg
5003	18	Ca-pyrolite	NaCl	03:47	56.73	61.47	0.99	2123	100	Brg+CaPv
5003	35	Ca-pyrolite	NaCl	02:03	56.54	67.86	1.73	2909	183	Brg+Fp+CaPv
5003	43	Ca-pyrolite	NaCl	04:02	56.38	65.99	0.75	2424	100	Brg+Fp
5220	30	Ca-pyrolite	Ne	03:30	56.67	63.27	0.94	2343	130	Brg+Fp
5220	42	Ca-pyrolite	Ne	03:41	57.83	55.42	0.69	2377	100	Brg
5220	45	Ca-pyrolite	Ne	02:14	58.66	51.55	0.67	2592	100	Brg+Fp
5920	6	Ca-pyrolite	Ar	03:32	56.46	64.49	1.70	2284	233	Brg

3.2.4 Chemical Analysis

I recovered the synthesized samples of the komatiitic composition (K33 and K100) using a micro-manipulator. The samples were processed in a focused ion beam (FIB) at Arizona State University (ASU). The center part of the heated area was extracted and mounted on a Cu grid. I analyzed the chemical compositions of the samples in the aberration-corrected scanning transmission electron microscope (STEM; JEOL ARM200F) combined with energy-dispersive X-ray spectroscopy (EDS) at ASU. A 120 keV of acceleration voltages were used. I performed point analysis with exposure time within 40 seconds depending on the beam sensitivity at a target area. For the K100 sample, the scanning analysis was performed to obtain chemical maps. The collected EDS spectra were fitted using a python code LMFIT (Newville *et al.*, 2016).

3.3 Results

3.3.1 The Stability of Ca-bridgmanite

Fig. 3.1 shows the two different sets of mineralogies depending on temperature in Ca-pyrolite and Ca#10Fe#10 compositions. I observed the absence of the XRD lines of CaPv above 2,250 K at 40–110 GPa, while Brg was always observed regardless of temperature (Fig. 3.2). Below 2,250 K, CaPv was identified with 110, 200, 211, and 220 lines (Fig. 3.1). Above 2,250 K, CaPv peaks were not observed except for run #4901_067 and #5003_035 at ∼2,900 K (Fig. 3.2). Fp was indexed by 200 and 220 lines in some runs, which are difficult to identify in the other runs in Ca-pyrolite due to the overlap with Brg or CaPv lines (Fig. 3.1). Nonetheless, I assume the existence of Fp in all runs in Ca-pyrolite composition because the intensities of the XRD peaks are noticeably increased, where the Fp lines are expected to be.

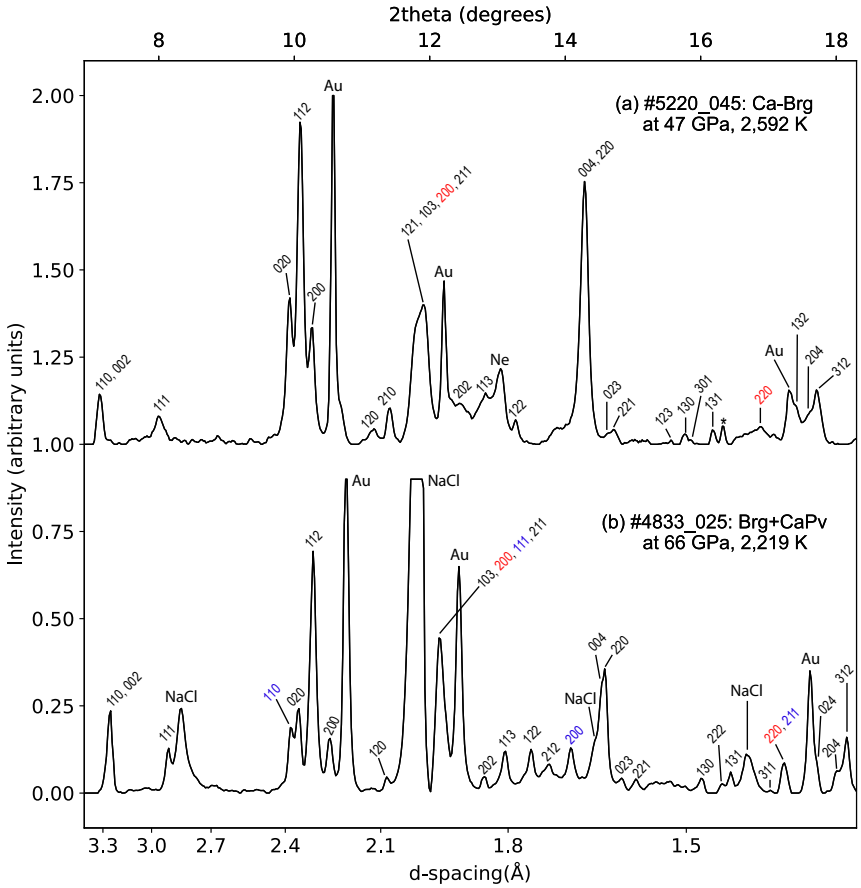

Figure 3.1: In-situ X-ray diffraction (XRD) patterns of Ca-pyrolite at high P–T in laser-heated diamond anvil cell (LHDAC). X-ray energy was 25.002 keV. The Miller indices of the major lines are provided in black, blue, and red colors for bridgmanite, $CaSiO_3$ perovskite, and ferropericlase, respectively. Ne (a) or NaCl (b) were used as pressure medium.

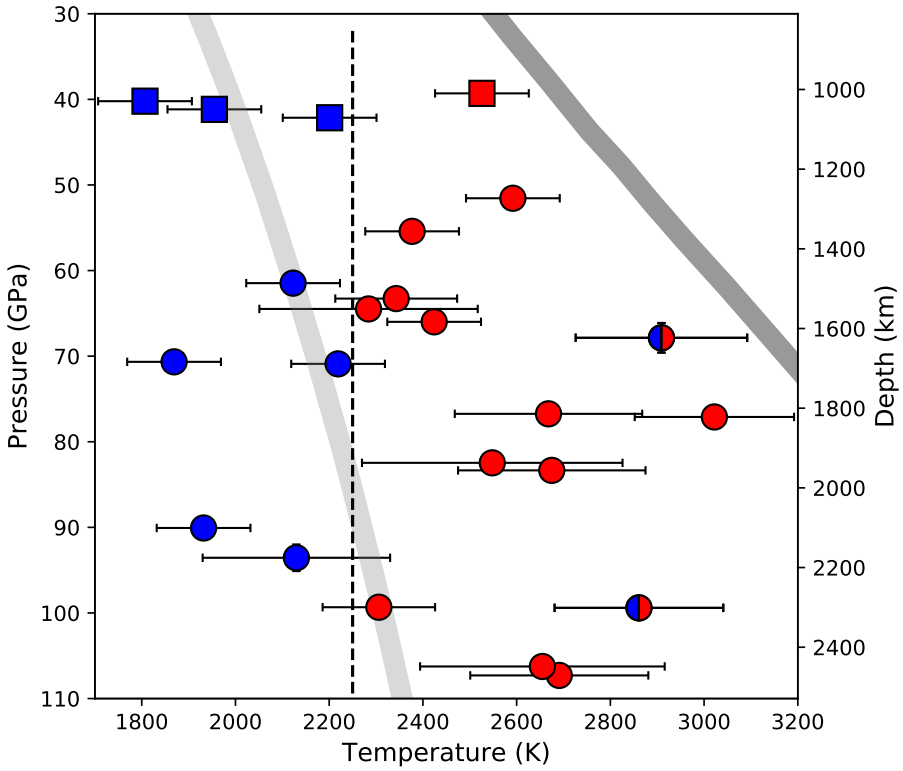

Figure 3.2: Phase stability in pressure-temperature (P–T) field. Circles and squares represent Ca-pyrolite and Ca#10Fe#10 compositions, respectively. Blue and red symbols represent the presence and the absence of $CaSiO_3$ perovskite in XRD observations, respectively, in their mineralogy besides bridgmanite and ferropericlase. The mix-colored circles indicate the presence of $CaSiO_3$ perovskite in XRD observations, but unit-cell parameters of bridgmanite are similar to those of Ca-bridgmanite. The mantle solidus is shown as the dark grey curve (Nomura *et al.*, 2014). The mantle geotherm is illustrated as the light grey bar (Brown and Shankland, 1981).

3.3.2 The Equation of State of Ca-bridgmanite in Ca-pyrolite Composition

I found the two sets of the unit-cell volumes of Brg in Ca-pyrolite at 1 bar–100 GPa and 300 K (Fig. 3.3). The unit-cell volumes of Brg, when CaPv was not observed (Ca-Brg), appear to be systematically larger by 1.4% than those of Mg-Brg, when CaPv was observed together in the explored pressure range. The unit-cell volume data were fitted to the Vinet equation with the fixed pressure derivative of bulk modulus ($K_0' = 4$). The fits yielded V_0 of 166.5(2) and 164.1(4) Å^3 and K_0 of 252.1(7) and 241.5(9) GPa for Ca-Brg and Mg-Brg, respectively (Table 3.3). For Mg-Brg, although the number of the unit-cell volume data is smaller for refined fitting, the fit matches well with the previous report of Brg in the pyrolitic composition (Fig. 3.3; Ricolleau *et al.*, 2010). The unit-cell volume of Ca-Brg at 1 bar and high pressures at 300 K in this study is much larger (∼1–2%) than those of Brg in pyrolitic compositions reported by previous studies (Andrault *et al.*, 2001; Lee *et al.*, 2004; Ricolleau *et al.*, 2009).

Table 3.3: Vinet equation of state parameters for Ca-bridgmanite (Ca-Brg) and Ca-low bridgmanite (Mg-Brg) at high pressure and 300 K. K_0' was fixed as 4 for all fits. Δ represents the difference between Ca-Brg and Mg-Brg. Dorogokupets and Dewaele (2007) was used for the pressure scale.

Composition	Brg type	V_0 (Å^3)	K_0 (GPa)	Δ V_0 (Å^3)	Δ K_0 (GPa)
Ca-pyrolite	Ca-Brg	166.5(2)	252.1(7)	2.4	10.6
	Mg-Brg	164.1(4)	241.5(9)	(1.4%)	(4.4%)
Komatiitic	Ca-Brg	168.3(0)	254.3(1)	1.9	6.0
	Mg-Brg	166.3(7)	247.5(8)	(1.2%)	(2.4%)

In addition to the increase in the unit-cell volume of Brg, I observed the changes in the unit-cell parameters between Ca-Brg and Mg-Brg (Table 3.2). Although both the a and c parameters are larger in Ca-Brg than in Mg-Brg, the difference in the a parameter between Ca-Brg and Mg-Brg is greater than the c parameter, resulting in the smaller c/a ratio in Ca-Brg. The b parameter seems similar between Ca-Brg and Mg-Brg therefore the smaller b/a ratio in Ca-Brg. These differences in the unit-cell parameters result in the decrease in anisotropy, suggesting that the effect of Ca on the unit-cell parameters is similar to that of Fe^{2+} in the A site (Lundin *et al.*, 2008; Dorfman *et al.*, 2012, 2013). The tilting angle of SiO_6 octahedra of Brg can be used to measure anisotropy of the orthorhombic perovskite with respect to the isotropic cubic perovskite (O'keeffe *et al.*, 1979). Fig. 3.4 illustrates the smaller octahedral tilting angle of Ca-Brg compared to Mg-Brg. Dorfman *et al.* (2013) documented the effect of Fe^{2+} on the decrease in the octahedral tilting angle of Brg. They reported that the octahedral tilting angle of (Mg,Fe)SiO_3 Brg increases with increasing pressure by $\sim$0.05 °/GPa, similar to 0.054 °/GPa of Ca-Brg in this study.

The previous studies reported that Fe^{3+} (Catalli *et al.*, 2010) and Al (Walter *et al.*, 2004a) increase the octahedral tilting angle of Brg in contrast to the effect of Fe^{2+} (Dorfman *et al.*, 2013). Mg-Brg in Ca-pyrolite in this study exhibits the larger octahedral tilting angle than $MgSiO_3$ Brg by 8 $\pm$ 2%, despite of the opposite effect from Fe^{2+} in Mg-Brg (Fig. 3.4). This suggests that Mg-Brg contains the considerable amount of Fe^{3+} and Al in Ca-pyrolite. In the Ca-Brg + Fp assemblage, Fe^{3+} and Al cannot exist in Fp but Ca-Brg. Therefore, the similar amounts of Fe^{3+} and Al in Ca-Brg to those in Mg-Brg are expected to be present.

The bulk modulus at 300 K (K_0) of Ca-Brg is larger than that of Mg-Brg by 4.4 % (Table 3.3). Dorfman *et al.* (2013) showed that K_0 of Brg increases with the increasing Fe^{2+}#. The measured K_0 of Ca-Brg is substantially larger than that of Mg-Brg in

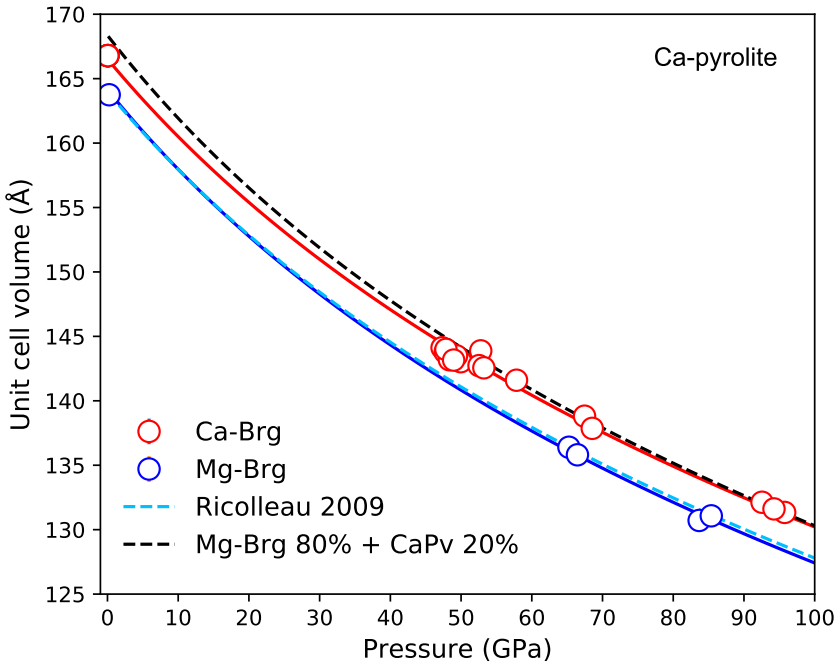

Figure 3.3: The compressibility of bridgmanite in Ca-pyrolite at 300 K. The data for the unit-cell volume of bridgmanite were obtained either from temperature-quench measurements after each heating cycle or from decompression measurements. The red and blue circles represent Ca-bridgmanite (Ca-Brg) and Ca-low bridgmanite (Mg-Brg), respectively. The solid curves are fits to the Vinet equation of state. The blue dashed curve is from bridgmanite in KLB-1 peridotite (Ricolleau *et al.*, 2009). The combined volume of Mg-Brg (86 %) and $CaSiO_3$ perovskite (14 %) is plotted as the dashed black curve for comparison.

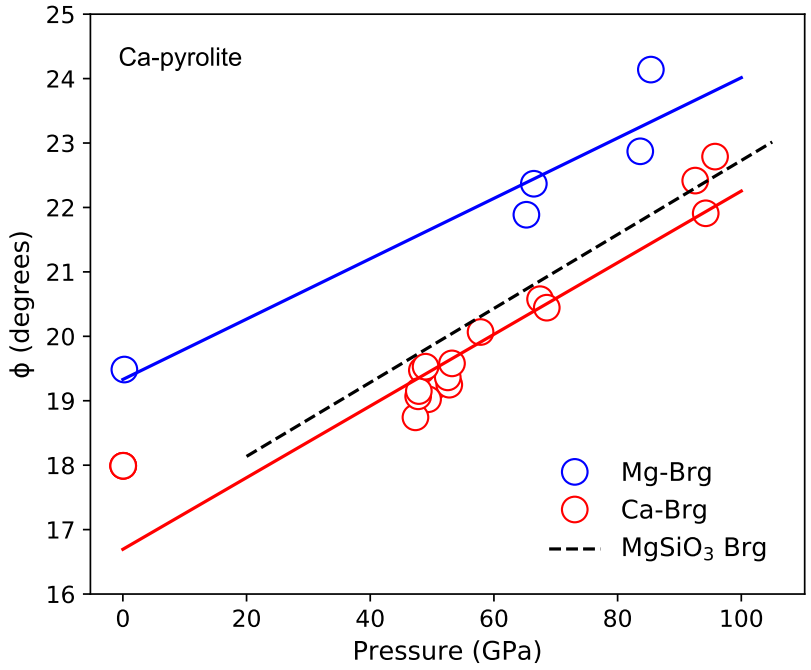

Figure 3.4: The octahedral tilting of bridgmanite in Ca-pyrolite. The red and blue circles represent Ca-bridgmanite (Ca-Brg) and Ca-low bridgmanite (Mg-Brg), respectively. The octahedral tilting angle for $MgSiO_3$ is shown as the black dashed line.

Ca-pyrolite composition, the effect of Ca on K_0 of Brg appears to be similar to that of Fe^{2+}. This observation is consistent with the observed octahedral tilting angle of Brg discussed above. The similar behavior between Ca and Fe^{2+} is likely because of their larger ionic sizes that substitute the smaller Mg in the A-site in the Brg structure.

However, the size difference from Mg is much greater with Ca than with Fe^{2+} (1.13, 0.92, and 0.86 Å for Ca^{2+}, Fe^{2+}, and Mg^{2+} in the 12-coordinated site; Shannon, 1976). The effects of Ca on the crystal structure of Brg may be greater than those of Fe^{2+} if their amounts are the same in Brg.

I estimated the relative proportion of Mg-Brg to CaPv based on the starting composition of Ca-pyrolite, assuming that all the $CaSiO_3$ component forms CaPv.

The estimation yielded 8:2 ratio of Mg-Brg to CaPv in mol, which is plotted as the red dashed line in Fig. 3.3. The volume of CaPv at 300 K was calculated with the equation of state parameters from Chen *et al.* (2018). The volume of Mg-Brg + CaPv is slightly greater than that of Ca-Brg in 0–100 GPa at 300 K, while the volume difference between these two becomes smaller with increasing pressure. Although the volume difference is likely within the experimental error range at high pressures, the volume comparison shows the possibility that the formation of Ca-Brg is energetically favorable at high temperatures (>2,250 K).

3.3.3 Chemical Composition of Ca-bridgmanite in the Komatiitic Composition

In order to further investigate the Ca dissolution in Brg without the possible interference of Fp, I synthesized samples of the komatiitic composition at 33, 65, and 100 GPa (K33, K65, and K100 samples, respectively) and at high temperatures. The samples were scanned with the laser to heat the entire sample evenly. The distances between the heating areas were 20 μm for K33 and 5 μm for K65 and K100. The synthesis temperatures were at 2,200 $\pm$ 200 K for K33, 2,450 $\pm$ 350 K for K65, and 2,300 $\pm$ 100 K for K100. In XRD patterns, I observed Brg with the strongest peaks in all runs. CaPv was only observed in K33, but not in K65 and K100. St peaks were observed with weak intensities in all K33, K65, and K100 likely because of the formation of Fe^{3+} through the charge disproportionation reaction in Brg (Frost *et al.*, 2004) that decreases the ratio of divalent cations to Si below 1. I also identified 104 and 116 peaks of alumina (Al_2O_3) with weak intensities from some of the runs on K65 and K100. In the other runs in K65 and K100, alumina was difficult to clearly identify because of the peak overlap with Brg.

The chemical analysis on the recovered samples confirmed the XRD observations. In K33, I found CaPv together with Mg-Brg that contains the limited Ca content

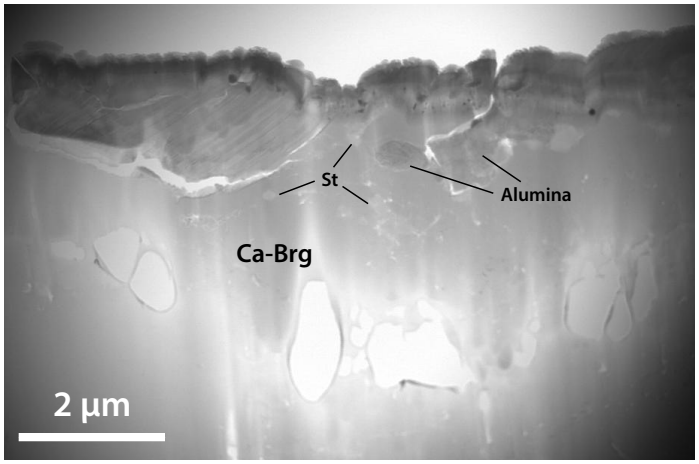

Figure 3.5: A bright-field image of the komatiitic composition. The sample was synthesized at 100 GPa and 2,300 K. Ca-Brg: Ca-bearing bridgmanite; St: stishovite.

Table 3.4: Chemical Compositions of Minerals in the Komatiitic Composition.

	K33[a]			K100[b]		
Cation#	Mg-Brg	CaPv	St	Ca-Brg	Alumina	St
Si	0.83	0.92	0.95	0.86	0.0	0.87
Al	0.20	0.02	0.01	0.15	1.97	0.04
Fe	0.20	0.07	0.01	0.20	0.03	0.02
Mg	0.72	0.10	0.02	0.60	0.0	0.05
Ca	0.05	0.88	0.01	0.19	0.0	0.02
Vol%[c]	84.4	14.3	1.4	94.7	3.1	2.2

[a] Measured by point analysis in TEM mode.

[b] Measured by the chemical mapping in STEM mode.

[c] Phase proportions were determined by mass balance calculation for K33 and area fractions in the STEM image for K100.

(Ca#5; Table 3.4). St was also observed as a minor phase, which is in an agreement with the XRD observations. In K100, the STEM images show that Ca-Brg exists as matrix surrounding the minor phases of alumina and St. The Ca content in Ca-Brg of K100 is significantly larger than in Mg-Brg of K33, suggesting the Ca dissolution in Ca-Brg (Ca# 0.19 and 0.05, respectively; Table 3.4).

The existence of alumina in K100 is consistent with the Al# in Ca-Brg in K100, which is smaller than in Mg-Brg in K33 (Al# 0.15 and 0.20, respectively; Table 3.4). The previous study showed that the solubility of Al_2O_3 increases with increasing pressure in $MgSiO_3$ Brg (Liu *et al.*, 2017). However, the presence in Fe^{3+} in Brg may play a role in the solubility of Al_2O_3 in Brg. At pressures below 40 GPa, the high-spin state (HS) is predominant in Fe^{3+}, which substitutes Mg^{2+} in A site, while Al^{3+} substitute Si^{4+} in B site in Brg. At around 40–60 GPa, the spin state of Fe^{3+} starts undergoing the transition from the HS to the low spin (LS; Fujino *et al.*, 2012; Hsu *et al.*, 2011). The ionic size of Fe^{3+} becomes much smaller with the spin transition, resulting in the cation exchange with Al^{3+} in the B-site. It is possible that LS-Fe^{3+} substitutes Si^{4+} in the B-site, while Al^{3+} substitutes Mg^{2+} in the A-site (Fujino *et al.*, 2012). The change in the substitution mechanism driven by the spin transition in Fe^{3+} may be related to the decrease in the solubility of Al^{3+} and the increase in the solubility of Ca in Brg.

I estimated $Fe^{3+}/\sum Fe$ in Brg based on the measured compositions by assuming the charge-balanced substitutions of Fe^{3+} and Al^{3+}. The calculations yielded 74 and 67% for K33 and K100, respectively, in a good agreement with previous reports of Fe,Al-bearing Brg (e.g. Frost *et al.*, 2004; Irifune *et al.*, 2010). The Fe^{3+}/Al ratio can be further estimated, which is larger in K100 than in K33 (0.9 and 0.75, respectively). However, this estimation method for $Fe^{3+}/\sum Fe$ is very sensitive to the Si# in the

stoichiometric composition of Brg, and therefore the large uncertainties could be involved given the error range of the EDS measurements (∼10%).

3.3.4 The Equation of State of Ca-bridgmanite in the Komatiitic Composition

I measured the unit-cell volumes of Ca-Brg (K65 and K100) and Mg-Brg (K33) in the komatiitic composition at 300 K (Fig. 3.6). The unit-cell volumes of Ca-Brg appear to be systematically larger by up to 1.2% than those of Mg-Brg (Table 3.3). The unit-cell volume data were fitted to the Vinet equation with the fixed pressure derivative of bulk modulus ($K_0' = 4$). The fits yielded V_0 of 168.3(0) and 166.3(7) Å^3 and K_0 of 254.3(1) and 247.5(8) GPa for Ca-Brg and Mg-Brg, respectively (Table 3.3).

Similar to the Ca-pyrolite composition, the octahedral tilting angles are different between Ca-Brg and Mg-Brg in the komatiitic composition (Fig. 3.7). The a, b, and c parameters are all larger in Ca-Brg than in Mg-Brg. The difference is the largest for the a parameter between Ca-Brg and Mg-Brg, then for the c parameter. Therefore, the both c/a ratio and b/a ratio are smaller in Ca-Brg than in Mg-Brg, consistent with those found in Ca-pyrolite (Section 3.3.2). The octahedral tilting angle is much smaller in Ca-Brg than in Mg-Brg, suggesting the Ca effect on the unit-cell parameters, consistent with the observations from Ca-pyrolite. The octahedral tilting angle of Ca-Brg in the komatiitic composition increases with pressure by 0.032 °/GPa, smaller than 0.054 °/GPa of Ca-Brg in Ca-pyrolite, possibly because of the compositional difference. K_0 is larger in Ca-Brg than in Mg-Brg by 2.3 % in the komatiitic composition, consistent with the observations of Ca-pyrolite.

Additionally, I have compared the volumes between Ca-Brg and Mg-Brg + CaPv at 300 K (Fig. 3.6). The phase proportions of Mg-Brg and CaPv in K33 were determined by the mass balance calculations based on their measured chemical compositions. The calculations yielded 86 mol% of Mg-Brg and 14 mol% of CaPv in K33

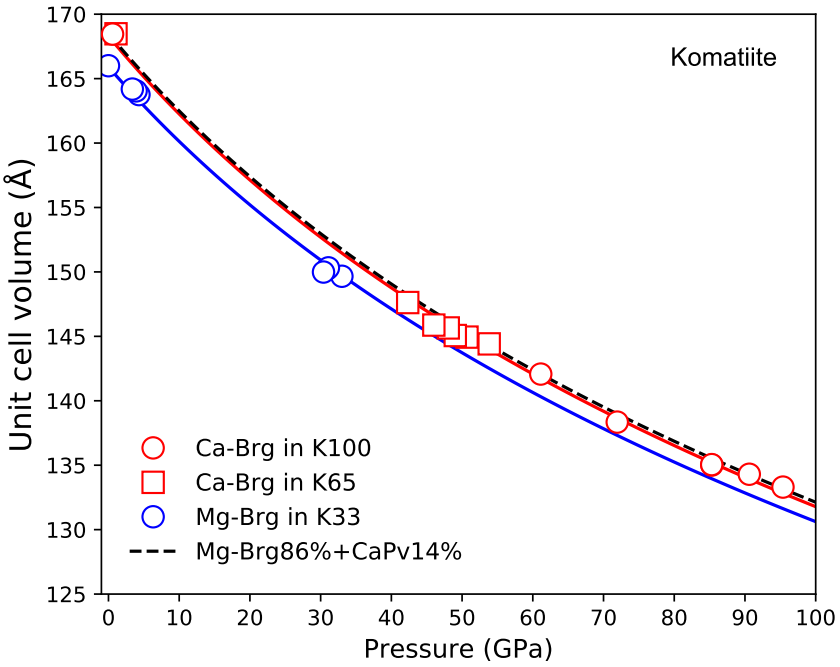

Figure 3.6: The compressibility of bridgmanite in the komatiitic composition at 300 K. I obtained the unit-cell volume of bridgmanite from decompression data. The red symbols represent Ca-bridgmanite (Ca-Brg) from different synthesis pressures (100 and 65 GPa, respectively). The blue triangles represent Ca-low bridgmanite (Mg-Brg). The combined volume of Mg-Brg (86 mol%) and $CaSiO_3$ perovskite (14 mol%) is plotted as the dashed curve for comparison. The Vinet equation of state was used for fitting.

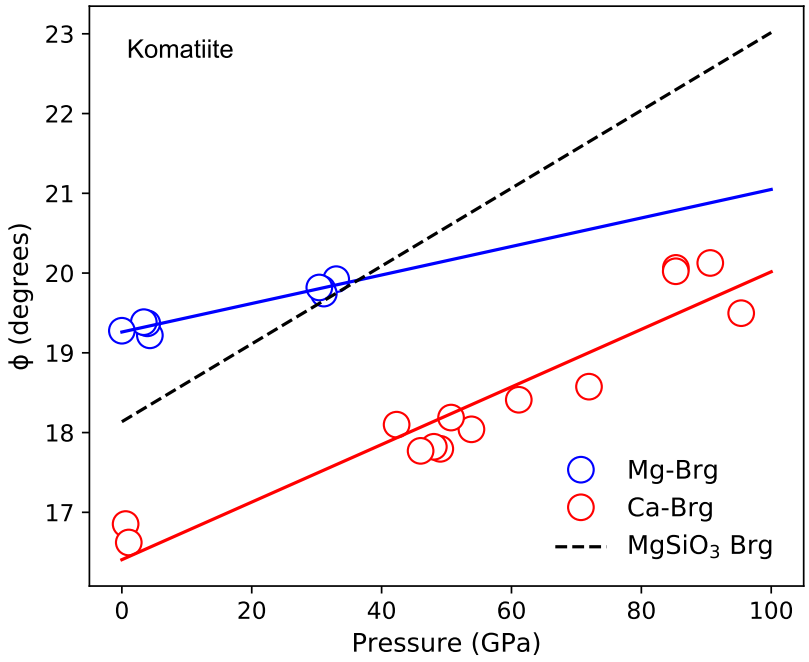

Figure 3.7: The octahedral tilting of bridgmanite in the komatiitic composition. The red and blue circles represent Ca-bridgmanite (Ca-Brg) and Ca-low bridgmanite (Mg-Brg), respectively. The octahedral tilting angle for $MgSiO_3$ is shown as the black dashed line.

(Table 3.4). The volume of CaPv at 300 K was calculated with the equation of state parameters from Chen *et al.* (2018). The combined volume of Mg-Brg and CaPv at 300 K is plotted as the black dashed line in Fig. 3.6. The volume of Ca-Brg is marginally smaller than the volume of Mg-Brg + CaPv, but the volume difference is within the experimental error range. In order to better evaluate the stability of Ca-Brg at high temperatures, the thermal expansivity of Ca-Brg needs to be investigated in the future.

3.4 Discussion

3.4.1 The Solubility of Calcium in Brg

The present study showed that Ca-Brg in the komatiitic composition has Ca#19 which is nearly same as Fe#20 (Table 3.4). This suggests that the significant amount of Ca can dissolve into Brg in the warmer regions in the lower mantle (Fig 3.2). However, the two exceptions (run #4901_067 and #5003_035) were observed at ∼2,900 K (Fig. 3.2), which show Brg and CaPv together in the XRD patterns. The unit-cell parameters of Brg in these runs are consistent with those of Ca-Brg at high pressures and 300 K. It is possible that the Ca solubility in Brg decreases at ∼2,900 K. Also, the appearance of CaPv at high temperatures of ∼2,900 K may be due to the incongruent melting behavior. As temperature increases close to the solidus (Fig. 3.2), some portions of the $CaSiO_3$ component might come out from the Ca-Brg structure and form CaPv, while Brg starts melting. Nonetheless, the present study does not draw conclusions on this observation.

3.4.2 The Stability of Ca-bridgmanite

The stability of Ca,Mg,Al-bearing perovskite (CMA-perovskite) in cubic or orthorhombic structure has been discussed by early experiments in mid ocean ridge basalt (MORB) and pyroxene compositions (Liu, 1987; Funamori *et al.*, 2000; Litasov *et al.*, 2004; Asahara *et al.*, 2005; Sano *et al.*, 2006). Asahara *et al.* (2005); Sano *et al.* (2006) pointed out that CMA-perovskite is a metastable phase that only forms from glass starting materials due to the slow kinetics and that decomposes into Mg-Brg and CaPv with increasing temperature. However, they investigated the low pressures of ∼20–35 GPa, which only represents the deep transition zone and the topmost lower mantle.

The present study found that at 40–110 GPa, Ca-Brg forms at higher temperatures above ∼2,250 K, whereas Mg-Brg and CaPv form at temperatures below ∼2,250 K. If the slow kinetics was involved in my experiments that used glass materials, it should have affected the low-temperature runs much more, which formed CaPv along with Mg-Brg.

Furthermore, the results in this study show that the volume of Ca-Brg is slightly smaller than that of Mg-Brg + CaPv up to 100 GPa at 300 K in both Ca-pyrolite and the komatiitic compositions. Although the differences were small to be within the resolution of the measurements, these results still raise the reasonable possibility that Ca-Brg is energetically favored over Mg-Brg + CaPv in the conditions of the deep lower mantle.

3.4.3 The Time-dependent Change in the Lower-mantle Mineralogy

The mantle geotherm from Brown and Shankland (1981) intersects the vertical line at 2,000 km-depth (2,250 K) in Fig. 3.2, suggesting that Ca-Brg could be stable below 2,000 km-depth in the present-day lower mantle. In this case, the pyrolitic lower mantle can be divided into two layers with different phase assemblages: the shallow-lower mantle (SLM) where Mg-Brg, Fp, and CaPv are stable; and the deep-lower mantle (DLM) where Ca-Brg and Fp are stable.

The Earth's mantle has cooled down since the Archean (Korenaga, 2008; Herzberg *et al.*, 2010). If the Ca incorporation into Brg depends on temperature at the depths of the lower mantle as suggested in this study, the thickness of the DLM where Ca-Brg is stable might have been reduced over time. In the Archean, the mantle would have been much hotter by ∼200 K (Herzberg *et al.*, 2010; Korenaga, 2008), than the present-day mantle. With the mantle geotherm from Brown and Shankland (1981), the boundary between the SLM and DLM would have been much shallower

to be 1,200 km-depth in the Archean. Since then, the boundary would have gradually deepened toward 2,000 km-depth in the present-day.

3.4.4 Compressibility of the Earth's Lower Mantle

To estimate the compressibility of the lower mantle, the bulk moduli of the major phases of Brg, Fp and CaPv and their proportions should be considered. Because the compressibility of the SLM has been well documented by previous studies, I will focus on that of the DLM in this discussion. My results show that Ca-Brg exhibits slightly greater K_0 than Mg-Brg by 4.4% (Table 3.3) in Ca-pyrolite. The Ca content in Ca-pyrolite used in this study is 2.6 times larger than in the 'normal pyrolite' from McDonough and Sun (1995). Therefore, the difference in K_0 between Ca-Brg and Mg-Brg should be much smaller in pyrolite than in Ca-pyrolite.

The chemical analysis of the komatiitic composition revealed that the Mg/Fe ratio is lower in Ca-Brg (in K100) than in Mg-Brg (in K33) because of the substitution of Mg with Ca. Based on this observation, I speculate that Fe# of Fp would be smaller when Ca-Brg is stable in pyrolite. While the proportion of Ca-Brg increases by incorporating $CaSiO_3$, the decrease in the Mg/Fe ratio in Ca-Brg results in the decrease of Fe# in Fp. The previous studies have shown K_0 of Fp decreases with increasing Fe# (e.g. Finkelstein *et al.*, 2017). K_0 of Fp would become larger when Ca-Brg exists because of the lower Fe#. Therefore, K_0 of Fp in the Ca-Brg + Fp assemblage would be larger than that of Fp in the Mg-Brg + Fp + CaPv assemblage in pyrolite. In addition, the absence of CaPv would increase K_0 of the Ca-Brg + Fp assemblage even further, because of the lower K_0 of CaPv (223 GPa with the fixed K_0'=4; Chen *et al.*, 2018) than that of Brg.

Overall, K_0 of the Ca-Brg + Fp assemblage would be greater by at least 4% than that of the the Mg-Brg + Fp + CaPv assemblage. This implies that the bulk

modulus of the DLM could be greater (i.e. less compressible) than previously thought. However, whether this difference between the SLM and DLM is large enough to be seismically detectable remains questionable because of the low Ca content in pyrolite.

3.4.5 Heat Producing Elements in Bridgmanite

U^{+4} and Th^{+4} are considered to be the major radiogenic heat source in the lower mantle (e.g. Arevalo *et al.*, 2009). Previous studies have suggested that the heat producing elements, such as U^{+4} and Th^{+4} can be stored in CaPv in the lower mantle (Corgne *et al.*, 2003; Gautron *et al.*, 2006; Gréaux *et al.*, 2009, 2012; Perry *et al.*, 2017). U^{+4} and Th^{+4} have the similar ionic size (1.17 and 1.21 pm for 12-coordination, respectively; Shannon, 1976) to Ca^{+2} (1.34 pm for 12-coordination site; Shannon, 1976), which allows them to substitute Ca^{+2} in the A site of the CaPv structure by the coupled-substitution mechanism as follows:

$$Ca^{2+} + 2Si^{2+} \leftrightarrow U(Th)^{4+} + 2Al^{3+} \tag{3.1}$$

This way, the charge difference between Ca^{2+} and $U(Th)^{4+}$ can be compensated with two Al^{3+} (Corgne *et al.*, 2003; Gautron *et al.*, 2006; Gréaux *et al.*, 2009, 2012; Perry *et al.*, 2017). However, in the lower mantle, Al is known to preferentially partition into Brg over CaPv (e.g. Hirose, 2002). The partitioning behavior of Al may limit the storage capability of the heat producing elements in CaPv.

In this study, I showed that Ca^{+2} can substitute Mg^{+2} in the A site of Brg, expanding its lattice structure. In fact, Ca^{2+} is even larger than U^{4+} and Th^{4+} in the 12-coordination of the A site (1.34, 1.17 and 1.21 pm, respectively; Shannon, 1976). In terms of the ionic size, the A site of Ca-Brg should be able to accommodate U^{4+} and Th^{4+}. Also, the chemical analysis showed that Ca-Brg contains a substantial amount of Al (Table 3.4). The capability of storing the heat producing elements may

be much larger in Ca-Brg than in CaPv. Therefore, the concentration of the heat producing elements may be larger in the DLM than in the SLM.

3.5 Conclusions

I conducted experiments on Ca-pyrolite, Ca#10Fe#10, and the komatiitic compositions in the lower-mantle related conditions of 40–110 GPa and 1,800–3,000 K. The XRD patterns of Ca-pyrolite and Ca#10Fe#10 show that Mg-Brg, Fp, and CaPv are stable below ∼2,250 K, whereas Ca-Brg and Fp are only stable above ∼2,250 K. The results suggest that Ca-Brg would be stable in the deep lower mantle with no CaPv. The chemical analysis on the recovered samples of the komatiitic composition revealed that a significant amount of Ca can dissolve into Brg up to 8.8 mol% (Ca#19 in the Brg stoichiometry) in the komatiitic composition. Similar to Fe^{2+}, the incorporation of Ca^{2+} into Brg results in: 1) an expansion of the unit-cell volume of Brg; 2) a decrease in anisotropy of its lattice structure; and 3) a decrease in compressibility. The volume comparison between Ca-Brg and Mg-Brg + CaPv showed that Ca-Brg is marginally smaller up to 100 GPa at 300 K, suggesting the possibility that the formation of Ca-Brg with no CaPv is energetically favorable. However, the thermal expansivity of Ca-Brg should be investigated in the future for better knowledge of the stability of Ca-Brg at the high temperatures of the lower mantle.

Chapter 4

THE MINERALOGY AND DENSITY OF THE VOLCANIC CRUST NEAR 670 KM-DEPTH IN THE ARCHEAN DEEP MANTLE

4.1 Introduction

The surface materials have been subducted into the deep mantle and played vital roles in mantle geochemistry and dynamics for 2.5–3.5 billion years of the Earth's history (e.g., Condie and Kröner, 2008; Laurent *et al.*, 2014; Tang *et al.*, 2016). Seismic tomographic images have shown the slab stagnation beneath the mantle transition zone (MTZ) in the Western Pacific (e.g., van der Hilst and Seno, 1993; Fukao *et al.*, 2009; Li and McNamara, 2013; King *et al.*, 2015). Indeed, sinking of the slab into the deep mantle can be challenged beneath the MTZ at 670–760 km-depth (Christensen, 1997; Ogawa, 2003; Davies, 2008; Klein *et al.*, 2017), where the density of the surrounding mantle increases dramatically because of the post-spinel transition in the surrounding mantle (Hirose, 2002; Ye *et al.*, 2014; Ishii *et al.*, 2018).

While the density of the modern subductig slab has been well documented (Hirose *et al.*, 1999; Irifune and Ringwood, 1993; Ringwood and Irifune, 1988), the density of the early Earth's materials is not the case. In the Archean, the mantle potential temperature has been much higher than the present day by approximately 200 K (Korenaga, 2008; Herzberg *et al.*, 2010). The high temperature results in the more extensive partial melting in the Archean which makes the two important differences for Archean volcanic crust. First, Archean volcanic crust forms with a much greater MgO content than mid ocean ridge basalt (MORB; Table 4.1) in the modern day (Herzberg *et al.*, 2007, 2010). The different composition of Archean volcanic crust

should lead to different mineralogy and density in high pressure-temperature (P–T) conditions in the mantle. Second, the thickness of the crust is much thicker in the Archean (up to 45 km-thick) than in the modern day (7 km-thick; Herzberg *et al.*, 2010; Herzberg and Rudnick, 2012). With the large thickness, Archean volcanic crust takes a large portion of the subducting slab in the Archean, and therefore plays a more important role in the sinking behavior of the subducting slab.

Archean volcanic crust could have been transported into the mantle through a range of different processes: delamination (e.g., Bédard, 2006; Johnson *et al.*, 2014), and subduction (e.g., Condie and Kröner, 2008; Laurent *et al.*, 2014; Tang *et al.*, 2016). If Archean volcanic crust remains as a heterogeneity in the present-day mantle, because of the slow chemical diffusion at high pressure (Holzapfel *et al.*, 2005; Stixrude and Lithgow-Bertelloni, 2012; Xu *et al.*, 2011; Ito and Toriumi, 2010), the behavior of such heterogeneity is also important for understanding the seismic observations of the mantle heterogeneities (e.g. Fukao *et al.*, 2009; Fukao and Obayashi, 2013; Wu *et al.*, 2019).

In addition, Archean volcanic crust might have contributed to the rise of atmospheric O_2 at approximately 2.4 Ga (the Great Oxidation Event or GOE) (Kasting, 2013). The ultramafic composition might have resulted in the more extensive H_2 production through serpentinization than in the modern day (Kasting, 2013). The compositional change in the volcanic crust during the mantle cooling might have reduced such H_2 production, leading to the accumulation of O_2 in the atmosphere. In addition, the recent measurements of the V partitioning in ancient volcanic rocks suggested that the reducing Archean upper mantle might have undergone the secular oxidation between 3.5 and 1.9 Ga (Nicklas *et al.*, 2019). The possible mechanisms for the oxidation processes include not only the compositional change of the volcanic crust recycled into the mantle but the homogenization of the redox state of the man-

tle by the effective mantle mixing (Nicklas *et al.*, 2019; Aulbach and Stagno, 2016). The style of the mantle convection in the Archean should have been affected by the changes in the tectonic mod. It is possible that the mantle convection associated with the subducting slab might have facilitated the whole mantle mixing with the primordial oxidizing materials stored in the lower mantle (Nicklas *et al.*, 2019; Aulbach and Stagno, 2016; Andrault *et al.*, 2018a).

The composition of the Archean materials sunken to the mantle has been modeled with komatiitic compositions (e.g. Nishihara and Takahashi, 2001; Klein *et al.*, 2017). Nishihara and Takahashi (2001) conducted multi-anvil experiments and calculated the density of komatiite with thermodynamic parameters based on the zero-pressure densities of the synthesized phases. They showed that the komatiite density is greater than the PREM density in the MTZ up to 23 GPa. The density of the surrounding mantle in the Archean is likely lower than the PREM density because of the higher temperature. Therefore, the density contrast between their komatiite and the Archean mantle may be even greater. However, their komatiite composition may not represent Archean volcanic crust formed by partial melting from Archean mantle because of the higher MgO content (32 wt%) and the lower Al_2O_3 content (4 wt%) compared to non-arc basaltic compositions in the Archean (23 and 9 wt%, respectively; Herzberg *et al.*, 2010; Johnson *et al.*, 2014, ; Table 4.1). Furthermore, the density was not directly measured at high P–T conditions.

Klein *et al.* (2017) has recently studied the density of komatiitic composition at depths of the MTZ and topmost lower mantle using a thermodynamic modelling program, Perple_X (Connolly, 2009). They used a less mafic komatiitic composition (26 wt% of MgO) for Archean volcanic crust (Herzberg *et al.*, 2010). The model predicted that komatiite is denser than the pyrolitic Archean mantle in the MTZ and topmost lower mantle, increasing the likelihood of the sinking of the material

into the lower mantle. However, unlike other compositions, such as modern MORB and pyrolite which have been cross-examined by theoritical calculations (Xu *et al.*, 2008; Stixrude and Lithgow-Bertelloni, 2012) and in-situ experiments (Ricolleau *et al.*, 2010; Hirose *et al.*, 2005), the density of Archean volcanic crustal composition has not been directly measured by in-situ experiments. Furthermore, no study has shown the combination of the densities of the crust and harzburgitic layer for the Archean subducting slabs. The lack of such consideration limits our understanding of the sinking behaviors of the Archean subducting slabs.

Here, I report experimental results on the composition for Archean volcanic crust at pressures of 19–34 GPa and temperatures of 1,400–2,400 K. The in-situ X-ray diffraction provides the direct measurements of the unit-cell volumes of the stable phases, allowing us to estimate the densities at high P–T conditions. I also explore the effects of harzburgite layer using Perple_X, for the case that Archean volcanic crust is transported through subduction style.

Table 4.1: Chemical compositions of pyrolite, basaltic crust, complementary residues, and Archean volcanic crust. After excluding minor elements, each composition was normalized to 100%.

wt%	Pyrolite[a]	B30[b]	Modern MORB[c]	Archean residue[b]	Modern residue[d]	Archean crust[e]
SiO_2	45.1	47.0	51.8	43.8	43.4	47.6
Al_2O_3	4.8	7.5	15.5	2.8	1.3	7.1
FeO	8.4	12.7	10.1	6.4	8.6	12.3
MgO	37.7	22.8	8.0	46.3	45.7	22.9
CaO	3.5	8.8	11.7	0.8	0.9	8.3
Na_2O	0.4	1.3	2.1	0	0	1.7
Mg#[f]	88.9	76.2	58.5	92.8	90.4	76.8
(Mg+Fe+Ca)/Si	1.49	1.15	0.63	1.72	1.76	1.12
Thickness (km)[g]	-	40	7	74	32	-

[a] McDonough and Sun (1995)

[b] Composition models ($X = 0.8$) from Johnson *et al.* (2014).

[c] Gale *et al.* (2013)

[d] Baker and Beckett (1999)

[e] Oceanic plateau basalt 3.3 Ga; Schulz (1982)

[f] Mg# = Mg/(Mg+Fe)

[g] Thickness of a layer in the subducting slab considered in this study.

4.2 Experimental Methods

4.2.1 Starting Material

I synthesized a homogeneous glass using the laser-levitation method (Tangeman *et al.*, 2001) by adapting the chemical composition from the partial melting model by Johnson *et al.* (2014) (Table 4.1). The model assumes that the MgO and FeO contents of the crustal composition linearly increase with an increase in the mantle potential temperature (T_P) based on the reported chemical compositions of a range of non-arc volcanic crustal compositions from 3.5 Ga to the present day (Johnson *et al.*, 2014; Herzberg *et al.*, 2007, 2010; Palin and White, 2016). From this model, I chose the composition for Archean volcanic crust (2.5–3.0 Ga; hereafter B30) that might have formed at a T_P of 1,600 K. I confirmed the successful synthesis of the starting material in an electron probe micro analyzer (JEOL JXA-8530F EPMA) combined with wavelength-dispersive X-ray spectrometer (WDS) at Arizona State University (ASU) (Table 4.1).

4.2.2 Laser-heated Diamond-anvil Cell Experiments

The powdered glass was mixed with ∼10 wt% of Au powder (grain size of 1–3 μm), which served as a pressure standard and a laser absorber in the laser-heated diamond-anvil cell (LHDAC) experiments. The mixture was compressed to thin foils with a size of 100–200 μm and a thickness of ∼10 μm. Then, the foil was loaded into a hole in a pre-indented rhenium gasket with a micro-manipulator (Microsupport Axis Pro SS) at ASU. The four spacers (<10 μm sized pure sample particle) were placed between the sample foil and each side of the diamond culets for the gas or liquid medium loading. I loaded Ne and Ar in the COMPRES-GSECARS high-pressure gas loading system (Rivers *et al.*, 2008) or the cryogenic liquid loading system at ASU.

For an NaCl medium, the powder was dried at 120°C for 4 hours and loaded into the sample chamber without spacers. I compressed the samples in the symmetric-type diamond-anvil cell with 400 μm-sized culet.

I have conducted LHDAC experiments combined with in-situ X-ray diffraction (XRD) at sector 13-IDD of the GeoSoilEnviroConsortium (GSECARS) in the Advanced Photon Source (APS) (Prakapenka *et al.*, 2008) (Tables S1 and S2). The pressure and temperature ranges of the experiments are 19–34 GPa and 1,400–2,400 K, respectively. For run #4430 only, I synthesized the sample in LHDAC at Arizona State University (ASU) and then measured diffraction patterns at high pressure and room temperature in DAC at sector 12.2.2 in the Advanced Light Source (ALS) (Table 4.2). I measured diffraction patterns with monochromatic X-ray beams of 0.3344, 0.4133, and 0.4959 Å for GSECARS and 0.4971 Å for ALS. For in-situ experiments, I focused the laser beams on both sides of the sample and aligned the laser beams coaxially with the X-ray beam by visually observing X-ray fluorescence, in order to measure XRD patterns at the center of the laser heating spot. The typical beam diameters for X-ray and the laser were ~5 and 20 μm, respectively. I fit the thermal radiation spectra measured from both sides of the sample to Planck gray-body equation for the estimation of temperature. I attached a gas membrane to the LHDAC for fine control of pressure during in-situ laser heating (Letoullec *et al.*, 1988), except for run #218 where the pressure was increased manually to the target pressure.

I measured diffraction images using a MarCCD or a Dectris Pilatus detector at GSECARS. For run #4430, diffraction images were collected with a Mar345 detector at ALS. I integrated the images to 1D diffraction patterns with the calibration parameters obtained from the LaB_6 standard in the DIOPTAS software (Prescher and Prakapenka, 2015). I collected diffraction images for 5–10 seconds to ensure enough quality for data analysis during heating and after quenching to room temperature.

For run #4430 at ALS, I exposed the detector for 120–300 seconds. The collected diffraction patterns were analyzed and fitted with a pseudo-Voigt profile function to obtain the peak positions in the PeakPo software (Shim, 2017a). I obtained unit-cell parameters using the PeakPo and UnitCell softwares (Holland and Redfern, 1997). I determined pressures with the equation of state (EOS) of Au (Dorogokupets and Dewaele, 2007) using the Pytheos software (Shim, 2017b). The pressures at high temperatures were further corrected according to Ye *et al.* (2017). The unit-cell volume of Au was calculated from the 2–5 diffraction lines for majority of the data points.

I heated multiple spots in each sample and avoided areas that are close to the Re gasket. For each heating spot, an area with a diameter of 20 μm was heated for up to 11 minutes (Table 4.2). The locations of heating spots were chosen with an enough distance up to 30 μm from the previously heated areas in order to start a new heating cycle with unheated fresh areas.

From in-situ XRD patterns I have observed that the glass samples transformed into crystalline phases within 5–60 seconds depending on temperature. Once crystalline phases formed, the XRD peak intensity gradually grows over time without a significant change in the further heating. For most runs, I first increase the laser power at a previously heated spot until a target temperature is reached, and then instantly translated the sample position such that the same laser power can be directly applied to a previously unheated glass spot. This heating method helps preventing kinetic effects in experiments with a gradual increase in temperature.

4.2.3 Chemical Analysis

I recovered the synthesized samples from runs #218 and #4430 in a micromanipulator. The samples were processed for the STEM measurements in a focused

Table 4.2: Run table for in-situ experiments of B30.

Sample#	Run#	Medium	Dur. (min)	Au V (Å^3)	P[a] (GPa)	P_err (GPa)	T (K)	T_err (K)	Phase assemblage
218	7	Ne	4.5	61.66	33.62	0.75	2356	100	Brg+CaPv
	13	Ne	5	61.91	32.54	0.75	2382	100	Brg+CaPv
	15	Ne	5	61.65	31.06	0.75	2012	100	Brg+CaPv
812	107	Ar	3.5	62.26	29.13	0.75	2160	100	Brg+CaPv
	76	Ar	2.5	62.51	24.67	0.76	1719	100	Brg+CaPv
	122	Ar	5	61.88	28.06	0.75	1766	100	Brg+CaPv
	102	Ar	3	62.18	28.87	1.09	2072	145	Brg+CaPv
914	96	Ar		62.74	25.98	0.76	2040	100	Brg+CaPv
	114	Ar	4	62.64	25.68	0.76	1938	100	Brg+CaPv
	16	Ar	2.5	65.07	13.09	0.78	1592	100	Gt+Rw
1415	54	Ar	3	63.61	21.20	0.76	1906	100	Gt+Rw
	137	Ar	3	63.15	21.31	0.76	1663	100	Gt+Rw
	38	Ar	3.5	62.70	22.64	0.76	1573	100	Gt+Rw+CaPv+(Brg)[c]
1514	93	Ar	3	63.11	23.79	1.64	1966	215	Gt+Brg+CaPv
	44	Ar	3.5	62.68	25.72	0.76	1966	100	Gt+Brg+CaPv
1615	82	Ar	2	63.07	24.25	0.76	2004	100	Gt+Brg
	86	Ar	5	62.89	23.44	0.76	1791	100	Gt+Brg
	97	Ar	4	62.61	24.89	0.76	1816	100	Gt+Brg+(CaPv)[c]
	41	Ar	6	63.05	24.06	0.76	1966	100	Gt+Brg+CaPv
	46	Ar	4	63.15	24.92	0.76	2140	100	Gt+Brg+CaPv
	63	Ar	5.5	62.82	23.66	0.76	1777	100	Gt+Brg+CaPv
	76	Ar	6.5	62.78	24.69	0.76	1889	100	Gt+Brg+CaPv
	51	Ar	3	62.99	23.18	0.76	1820	100	Gt+Brg+CaPv
1912	28	NaCl	2 sec.	60.70	34.16	0.74	1737	100	Brg+CaPv
	91	NaCl	2 sec.	61.21	33.28	0.75	2003	100	Brg+CaPv
2115	127	Ar	2	61.99	29.40	0.75	2014	100	Brg+CaPv
2715	167	Ar	1.5	62.94	26.65	0.76	2247	100	Gt+Brg+CaPv
	189	Ar	3	62.72	25.08	0.76	1904	100	Gt+Brg+CaPv
	196	Ar	5	62.54	25.88	0.76	1899	100	Gt+Brg+CaPv
	20	Ar	5	63.82	18.90	0.77	1718	100	Gt+Rw
	81	Ar	4	63.21	22.56	0.76	1834	100	Gt+Rw
	86	Ar	1	63.56	20.75	0.76	1822	100	Gt+Rw
	89	Ar	2	63.92	20.24	0.83	1947	108	Gt+Rw
	95	Ar	1.5	63.36	18.98	0.76	1476	100	Gt+Rw
	99	Ar	2	62.91	21.09	0.76	1496	100	Gt+Rw
	114	Ar	3.5	63.38	20.92	0.76	1746	100	Gt+Rw
	141	Ar	2	63.50	20.04	0.76	1695	100	Gt+Rw
4530	98	KCl	4	63.38	23.77	1.25	2120	164	Gt+Brg
	91	KCl	5.5	62.81	25.83	1.31	2058	173	Gt+Brg+CaPv
	119	KCl	5	62.59	24.24	1.06	1715	140	Gt+Brg+CaPv
	25	KCl	5	62.83	23.18	0.83	1724	110	Gt+Brg+CaPv
	38	KCl	7.5	63.14	24.89	1.22	2126	161	Gt+Brg+CaPv
5733[b]	12	Ar	NA	62.02	19.52	NA	1900	150	Gt+Rw

[a] Pressure was determined by Au scale (Dorogokupets and Dewaele, 2007) and corrected according to (Ye *et al.*, 2017).

[b] Pressure was measured at 300 K.

[c] The phases in parenthesis were identified with the weak X-ray diffraction peaks.

ion beam (FIB; FEI Nova 200 and FEI Helios) at ASU and University of Arizona (UofA), respectively. I extracted the center part of the heated area and mounted it on a Cu or Mo grid. The composition of the sample was analyzed in the aberration-corrected scanning transmission electron microscope (STEM): JEOL ARM200F at ASU and Hitachi HF-5000 at UofA combined with energy-dispersive X-ray spectroscopy (EDS). A 120 and 200 keV of acceleration voltages were used at ASU and UofA, respectively. I measured standard spectra from the starting glass material for the data analysis. I performed a 2D chemical mapping for run #4430 and then estimated volume fractions of phases from the area fraction (Fig. 4.3). I also performed a point analysis with exposure time of 20–40 seconds depending on the beam sensitivity at a target grain. The collected EDS spectra were fitted using a python code LMFIT (Newville *et al.*, 2016).

4.3 Experimental Results

I have found three distinct P–T fields with different mineralogy in the experiments (Fig. 4.1): garnet-dominant (Gt-dominant), garnet-bridgmanite-transition (Gt-Brg-transition), and bridgmanite-dominant (Brg-dominant) P–T fields (Fig. 4.2).

4.3.1 Garnet-dominant P–T Field

Between 19 and 25 GPa, I observed Gt and ringwoodite (Rw) as stable phases (Fig. 4.1a). The diffraction peak intensities indicate that Gt represents the major phase of the mineralogy (Fig. 4.2), which can be supported by the STEM observations. Fig. 4.3 shows a high-angle annular dark-field (HDADF) image of the sample from run #4430 which was synthesized at 19.5 GPa (pressure measured at 300 K) and 1,900 K in LHDAC. The chemical maps of the image shows that Gt exists as matrix that surrounds the Rw grains. From the STEM-EDS images, I obtained 85.3 and 14.7 vol%

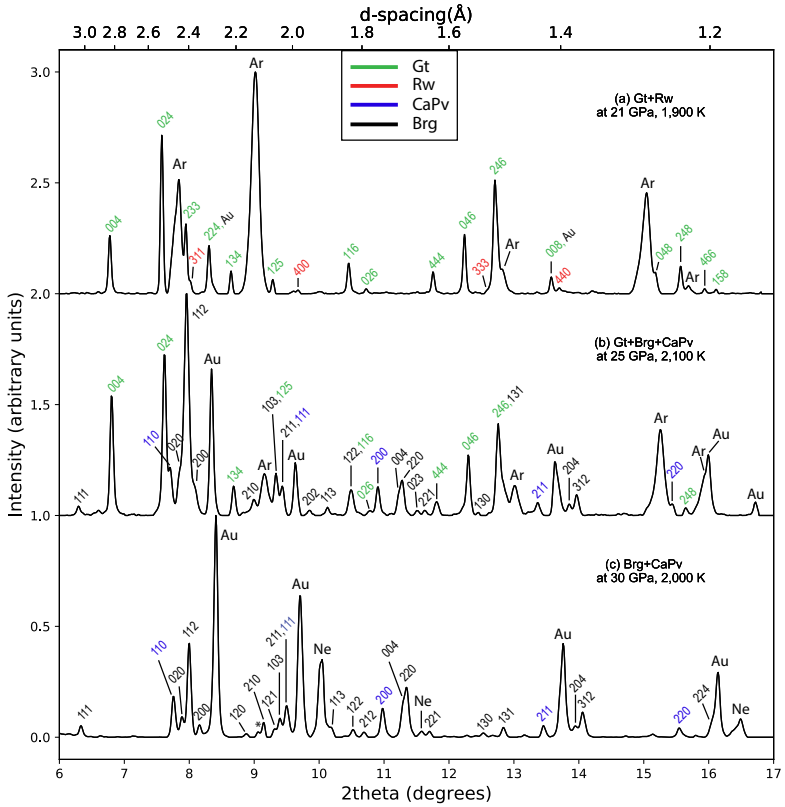

Figure 4.1: In-situ X-ray diffraction (XRD) patterns of B30 at high P–T in laser-heated diamond anvil cell (LHDAC). X-ray energy was 37 keV. The Miller indices of the major lines are provided. Gt: garnet; Rw: ringwoodite; CaPv: $CaSiO_3$ perovskite; Brg: bridgmanite; Au: gold (pressure standard); Ar: argon (medium); Ne: Neon (medium); and $*$: unidentified peaks.

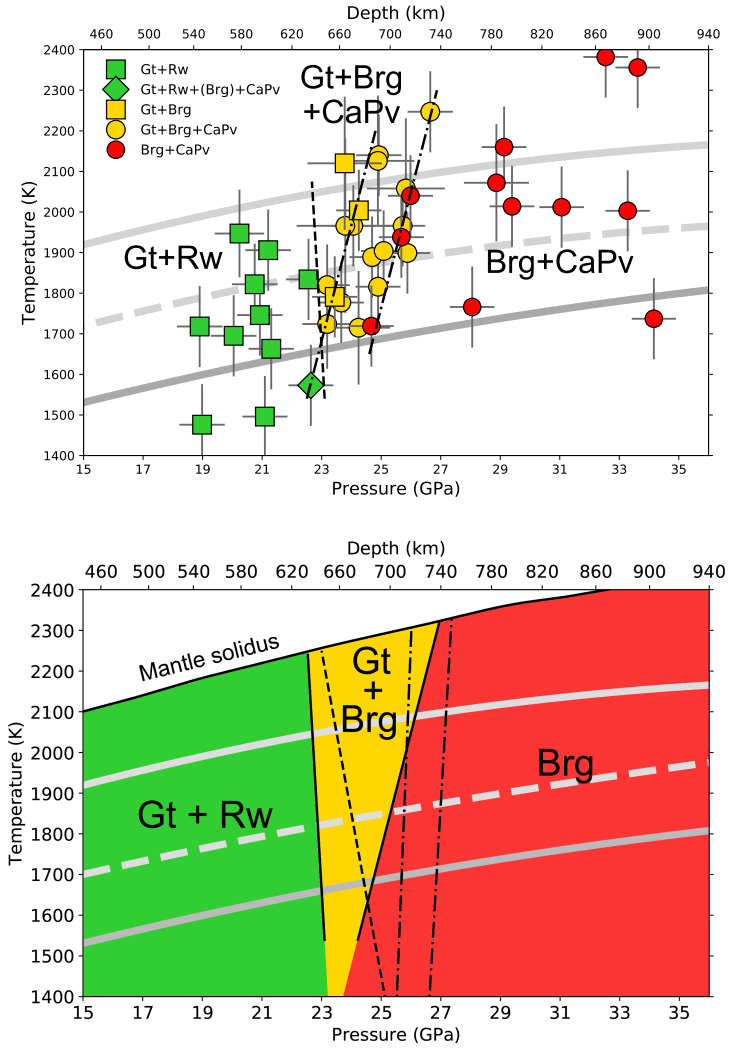

Figure 4.2: Phase changes in the B30 composition at high pressure and temperature. The light gray line represents the Archean mantle geotherm, which was shifted by 200 K from the modern mantle geotherm (the dashed gray line; Brown and Shankland, 1981). The gray line represent the temperature profile of the subducting slab after Klein *et al.* (2017). Top: Each symbol represents one heating cycle in the LHDAC experiments. The dashed and dot-dashed lines indicate the post-spinel and post-Gt transition boundaries determined in this study, respectively.

(Caption continued on the following page.)

Figure 4.2: Bottom: The major phases in the distinctive mineralogy fields. The black solid lines are Brg-in and Gt-out boundaries determined in this study. The post-spinel transition boundary in pyrolite (Ye *et al.*, 2014) is plotted as the dashed line. The post-garnet transition boundaries in modern MORB (Hirose *et al.*, 1999) are plotted as the dot-dashed lines. The mantle solidus is obtained from Andrault *et al.* (2018b). Gt: garnet; Rw: ringwoodite; CaPv: calcium perovskite; Brg: bridgmanite.

for the area proportions of Gt and Rw, respectively, consistent with the mass-balance calculation, which yielded 82.7 and 17.3 vol% of Gt and Rw, respectively (Table 4.4).

The modern MORB mineralogy features Gt as the most abundant component (60–90 vol%) (Irifune and Ringwood, 1993; Litasov and Ohtani, 2005) as does B30 mineralogy (86 vol%; Table 4.4). However, stable minor phases are significantly different between these two compositions. The ratio of divalent cations (Mg, Fe^{2+}, Ca) to Si (referred to as Di/Si hereafter) for B30 is higher than 1 ($\sim$1.15) and therefore excess MgO and FeO can form Rw in addition to Gt as observed from the experiments in the present study. On the other hand, in the modern MORB composition the Di/Si ratio is low enough (0.63) to form Stv from excess silica content (Gale *et al.*, 2013). In addition, the greater Al content (15.5 wt%) in modern MORB adds Al-rich phase to the mineralogy, whereas nearly all Al is incorporated in Gt in B30 (8.6 wt%). The mineralogy of the modern MORB composition consists of Gt, Stv, CaPv, and Al-phase, in an order of their abundances, at 15–26 GPa and 1,473–2,573 K (Irifune *et al.*, 1986; Irifune and Ringwood, 1993; Hirose and Fei, 2002).

At a similar pressure range, pyrolite has Rw (or Wd), Gt, CaPv, and akimotoite (Aki) in an order of abundance (Hirose, 2002; Ye *et al.*, 2014; Ishii *et al.*, 2018). Pyrolite has a much higher Di/Si ratio (1.49) than modern MORB and B30 (Table 4.1), making Rw (or Wd) the most abundant phase in the mineralogy As shown

in Table 4.4, Gt represents 84 vol% in B30, whereas Rw represents 60 vol% in pyrolite (Irifune *et al.*, 2010; Ishii *et al.*, 2018).

Table 4.3: Garnet compositions of pyrolite, B30, and modern MORB.

	20.5 GPa 2,073 K	23 GPa 1,900 K	24 GPa 2,023 K
Wt%	Pyrolite[a]	B30[b]	MORB[c]
SiO_2	50.8	49.7	40.7
TiO_2	0	0	0.7
Al_2O_3	10.6	8.6	20.6
FeO	5.0	11.8	14.4
MnO	0	0	0.2
MgO	28.0	20.9	12.3
CaO	4.6	9.0	8.1
Na_2O	0.3	NA	2
K_2O	0.2	0	0
Cr_2O_3	0.7	0	0.1
Total	100.1	99.3	99.1

[a] Hirose (2002)
[b] This study
[c] Hirose and Fei (2002)

The chemical composition of Gt is significantly different among B30, modern MORB, and pyrolite (Table 4.3). Compared to B30, Gt in modern MORB has twice more Al_2O_3 (8.6 and 20.6 wt%, respectively) and half as many MgO (20.9 and 12.3 wt%, respectively) as B30 has (Hirose and Fei, 2002). Gt in pyrolite has nearly half as many FeO (5.0 and 11.8 wt%, respectively) and CaO (4.6 and 9.0 wt%) as B30 does but slightly more MgO than in B30 (Hirose, 2002). These compositional differences are important to consider for the density and velocity profiles.

4.3.2 Garnet-bridgmanite-transition P–T Field

At intermediate pressures in the experiments, I observed the Gt-Brg-transition *P–T* field in B30 (Fig. 4.2). Above 23 GPa, Rw disappears and Brg appears, suggesting the occurrence of the post-spinel transition where Rw decomposes into Brg and

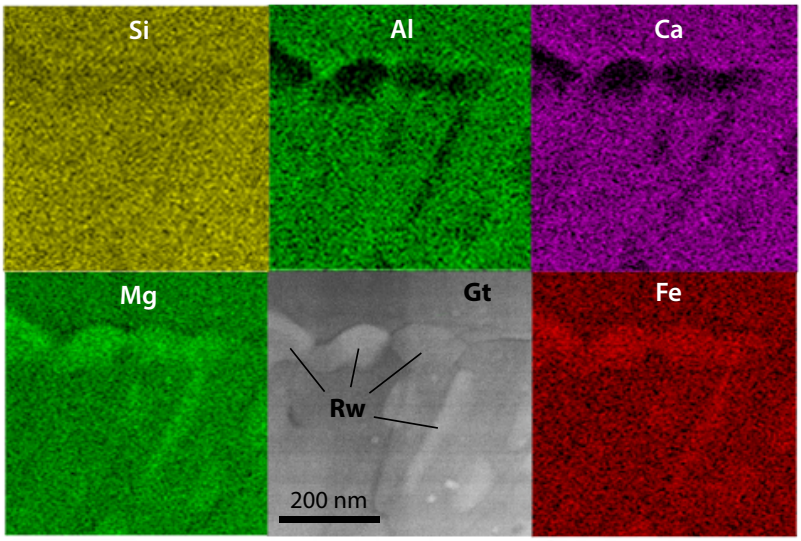

Figure 4.3: A high-angle annular dark-field image in the different region with chemical maps of B30 in LHDAC. The sample was synthesized at 19.5 GPa and 1,900 K. The brighter color in each chemical map represents the more concentration of the corresponding element. The chemical compositions and the proportions of individual phases are provided in Table 4.4. Gt: garnet; Rw: ringwoodite.

ferropericlase (Fp). While the diffraction peak intensities show that Gt is still the major phase in the Gt+Brg mineralogy (Fig. 4.1), I could not resolve Fp in XRD patterns because of the peak overlap with Ar, Gt, or Brg peaks. Furthermore, the peak intensities of Fp is expected to be small because of the possible reduction process in amount. Brg is known to have high capacity for Fe^{3+} through the charge disproportionation reaction: 3FeO to $2Fe_2O_3$ and Fe metal (Frost *et al.*, 2004). If a significant fraction of Fe is Fe^{3+}, the more Brg can form by the coupled-substitution of Mg^{2+} + Si^{4+} with Fe^{3+} + Al^{3+}, and therefore reduce the available FeO for Fp in the system (e.g., McCammon, 1997; Andrault *et al.*, 2001). While it involves with large uncertainty, the measured composition of Brg requires approximately 0.57 for $Fe^{3+}/\sum Fe$, which is consistent with previous reports (e.g. Shim *et al.*, 2017). However, I did not

Table 4.4: Chemical compositions of recovered samples of B30 in the Gt-dominant P–T field and Brg-dominant P–T field. The compositions were normalized to be 100% in total.

	19.5 GPa†, 1,900 K		31 GPa, 2,000 K	
wt%	Gt	Rw	Brg	CaPv
SiO_2	49.7	41.4	47.9	48.1
Al_2O_3	8.6	2.7	9.0	1.1
FeO[a]	11.8	23.8	13.1	4.6
MgO	20.9	29.2	26.3	3.4
CaO	9.0	2.8	3.7	42.8
Proportions (vol%)				
Mass balance	82.7	17.3	81.6	18.4
EDS mapping	85.3	14.7		
Rietveld			82.2	17.8
Average[b] (vol%)	84.0	16.0	81.9	18.1

[a]All Fe is assumed to be Fe^{2+}.
[b]Averaged proportions from the two different methods.
†Pressure was measured at 300 K.

observe Fe metal in either STEM observations or XRD patterns, perhaps because of the expected small amount of Fe metal. Although the limited number of data points increases the uncertainties, the P–T slope of Brg-in boundary was roughly estimated to be -0.8 ± 0.3 MPa/K, in a good agreement with the Clapeyron slope of the post-spinel transition from previous studies (Katsura *et al.*, 2003; Litasov *et al.*, 2005; Ishii *et al.*, 2011, 2018).

At higher pressures above 1,600 K, CaPv was observed alongside Gt and Brg. The diffraction peak intensities of Brg are in general stronger in the Gt + Brg + CaPv mineralogy than in the Gt + Brg mineralogy. These observations suggest the post-Gt transition where Gt decomposes into CaPv and Brg. I observed the two phase boundaries for the post-Gt transition with 1.7 GPa of the pressure interval: the CaPv-in boundary and Gt-out boundary. The P–T slopes of these boundaries

were determined to be 3.5 ± 0.5 MPa/K, which is in the middle of the range of the Clapeyron slopes of the post-Gt transition in previous studies (Hirose *et al.*, 1999; Kubo and Akaogi, 2000; Oguri *et al.*, 2000; Hirose, 2002; Litasov *et al.*, 2004; Ishii *et al.*, 2018). Note that the uncertainties of the *P–T* slopes may be large due to the limited number of data points across the boundaries. The gradual post-Gt transition in a range of pressure has been reported by earlier experiments of Al-bearing Gt (Irifune *et al.*, 1996) up to 2.1 GPa of an interval at 1,773 K for 3–11 mol% of Al_2O_3. Gt in B30 contains 4.8 mol% of Al_2O_3 which is estimated to yield 1.1 GPa interval for the post-Gt transition according to Irifune *et al.* (1996). However, Gt in B30 also contains a significant amount of FeO (11.8 wt%; Table 4.1), the effect of which on the pressure interval of the post-Gt transition is not well known.

The opposite signs of *P–T* slopes of the post-spinel and post-Gt transitions (−0.8 ± 0.3 and 3.5 ± 0.5 MPa/K, respectively) results in the wider stability of the Gt-Brg-transition *P–T* field with an increase in temperature above 1,600 K. Below 1,600 K, I do not provide the sufficient number of data points due to the large kinetic effects at lower temperatures. One run at 22.6 GPa and 1,570 K (the green diamond in Fig. 4.2) shows the signs of Brg 112, 200, and 220 lines and strong CaPv 110 line in the XRD pattern, alongside the strong Gt and Rw lines. These observations are in line with CaPv-in boundary observed from the higher temperatures, suggesting that the post-Gt transition may occur at shallower depths than the post-spinel transition at lower temperatures.

The most noticeable difference in mineralogy between modern MORB and B30 at the intermediate pressure range is the depths of Brg-in and Gt-out boundaries (Fig. 4.2b). For example, at 1,700 K Brg-in boundary appears as the post-spinel transition at a lower pressure of 23 GPa in B30 than the post-Gt transition at 25.8 GPa in modern MORB (Hirose *et al.*, 1999). The Si-rich composition of modern MORB does

not form Rw in the mineralogy, resulting in the absence of the post-spinel transition, which can occur at the shallower depth than the post-Gt transition. Then, Gt completely transformed to Brg at 24.8 GPa in B30, whereas Gt persists until 26.8 GPa in modern MORB (60–70 vol%) (Hirose *et al.*, 1999; Irifune and Ringwood, 1993; Litasov and Ohtani, 2005). The difference in the depth and the P–T slope of Gt-out boundary between B30 and modern MORB is likely caused by the compositional difference in Gt (Table 4.3).

Pyrolite has the similar mineralogy to B30 in tje Gt-Brg-transition P–T field. In pyrolitic composition, Gt and Brg coexist as major components (Hirose, 2002; Ishii *et al.*, 2018) at 22–26 GPa. Also, pyrolite exhibits the negative slope for Brg-in boundary because of the post-spinel transition. Brg-in boundary appears at a nearly same pressure in B30 and pyrolite: 22.8 and 22.6 GPa at 1,900 K, respectively (Ishii *et al.*, 2018). On the other hand, the Gt-out boundary appears at a higher pressure in B30 than in pyrolite by 1.1 GPa: 25.5 and 24.4 GPa at 1,900 K, respectively (Ishii *et al.*, 2018)).

4.3.3 Bridgmanite-dominant P–T Field

At pressures above 25 GPa, the mineralogy of B30 becomes Brg and CaPv (Fig. 4.2). The diffraction intensities show that Brg is the major phase in the Brg + CaPv system (Fig. 4.1). The Di/Si ratio of B30 is higher than 1 (1.15), the excess MgO and FeO can stabilize Fp together with Brg and CaPv, if the majority of Fe is Fe^{2+}. However, I could not identify Fp peaks in the diffraction patterns because of the expected peak overlap with the Brg peaks. Fp was not observed in TEM analysis also. The amount of Fp might have been too small to be detected because the dispropotionation reaction of Brg (Section 4.3.2; Frost *et al.*, 2004) can reduce the available number of Fe^{2+} for Fp. The calculated phase proportions based on the measured compositions

by TEM-EDS (Table 4.4) yield only 1 ± 1 vol% of Fp. For Brg and CaPv, 81.6 and 18.4 vol% were obtained by the mass-balance calculations, consistent well with 82.2 and 17.8 vol% from Rietveld refinements using GSAS-II (Toby and Von Dreele, 2013) within 1 % of difference (Table 4.4).

Modern MORB contains much lower content of Brg than B30 at P–T conditions of the lower-mantle. Modern MORB contains 30, 27, 22, and 21 vol% of CaPv, aluminous phase, Stv, and Brg, respectively at 31 GPa (Ricolleau *et al.*, 2010). Pyrolite and B30 are much alike in that Brg is abundant (75, 18, and 7 vol% for Brg, Fp, and CaPv, respectively, above 27 GPa for pyrolite; Irifune *et al.* (2010); Ishii *et al.* (2018)), but different in that B30 contains very small or no Fp in the mineralogy.

4.4 Density Profiles

4.4.1 Density Profile of Archean Volcanic Crust

I estimated density profiles of Archean volcanic crust (B30) along the low and equilibrated temperature profiles in the Archean (hereafter referred to as AL and AE, respectively). The AL temperature was obtained from the temperature model of the subducting slab in Klein *et al.* (2017). For the AE temperature, I assumed the same temperature as the surrounding mantle in the Archean, which was shifted from the modern mantle geotherm (Brown and Shankland, 1981) by 200 K (Korenaga, 2008; Herzberg *et al.*, 2010). Fig. 4.5 compares the geotherm models with the adiabatic temperature gradients.

The in-situ X-ray experiments provided the direct measurements of the unit-cell volumes of the stable phases at high P–T. I considered Gt, Rw, Brg, and CaPv at 20–34 GPa. For the Gt + Rw mineralogy, the chemical compositions and phase proportions of Gt and Rw were obtained from the STEM-EDS measurements, which

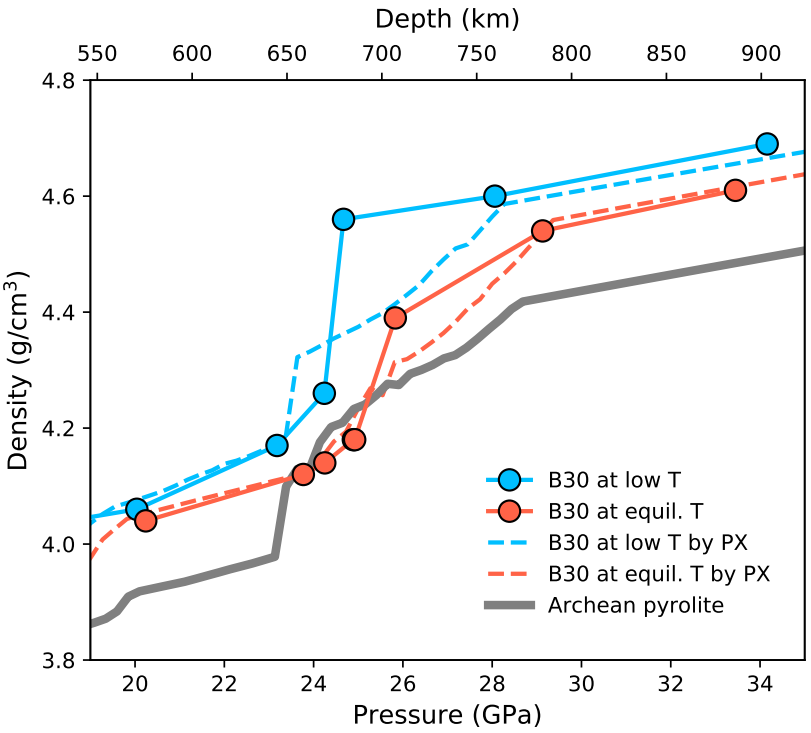

Figure 4.4: Density profiles of B30 for temperature profiles in the Archean. The orange, and red curves represent low (AL), and equilibrated (AE) temperature profile in the Archean. The solid and dashed lines indicate densities determined by experiments and by Perple_X (PX; Connolly, 2009), respectively. The circles along the solid lines represent the data points obtained from the experiments in the present study. Information on the temperature profiles can be found in Table 4.5.

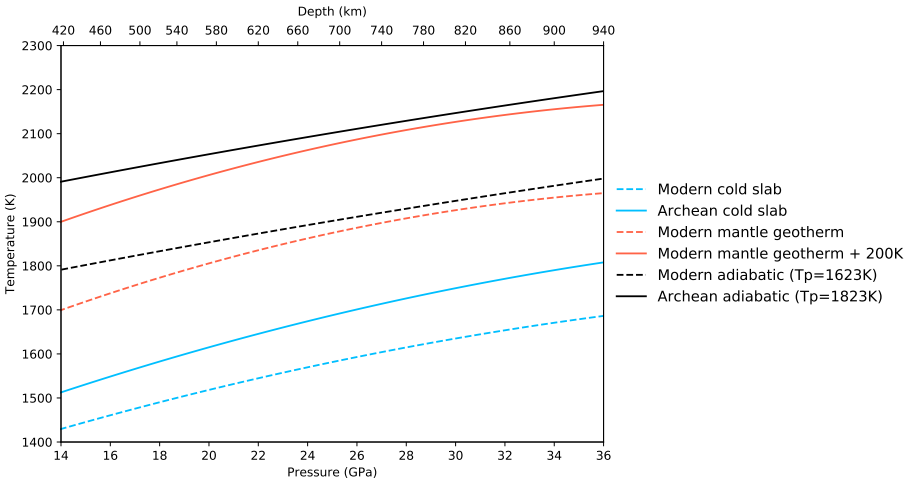

Figure 4.5: Temperature gradients of subducting slabs (blue) and pyrolite (red), and mantle adiabatic gradients (black). Solid and dashed lines represent modern and Archean. Temperature gradients of subducting slabs are from Klein *et al.* (2017). 0.4 K/km is used to plot the mantle adiabats.

Table 4.5: Methods used for the density calculation in this study. Exp: from our experiments; PX: from Perple_X calculation.

Mineralogy	Archean	Modern
Crust	EXP	PX
Harzburgite	PX	PX
Pyrolite	PX	PX

Temperature profile	Archean	Modern
Low	K17[a]	K17[a]
Equilibrated	B81+200 K[c]	B81[b]

[a] Klein *et al.* (2017)
[b] Brown and Shankland (1981)
[c] 200 K added to the modern mantle geotherm.

were assumed to remain unchanged within the same mineralogy field (Table 4.4). At pressures above Brg-in boundary and below CaPv-in boundary, I took Fp into account the mineralogy (Gt + Brg + Fp) and density calculations. The measured Rw composition was used to model the compositions and proportions of Brg and Fp, which form through the post-spinel transition. The unit-cell volumes of Fp were calculated by the equation of state from Speziale *et al.* (2007). At pressures above CaPv-in boundary (for the Gt + Brg + CaPv mineralogy), the compositions of Brg and CaPv were obtained from the STEM-EDS measurements and assumed to be remain unchanged (Table 4.4). Their proportions were obtained by mass-balance calculations based on the gradual transformation of Gt into Brg and CaPv. At pressures above Gt-out boundary (for the Brg + CaPv mineralogy), the compositions and proportions of Brg and CaPv were assumed to remain unchanged (Table 4.4).

I calculated the density of pyrolite in the Archean for comparisons with the B30 density (See Section 4.4.3 for the method). Fig. 4.4 shows that the B30 density is greater than the pyrolite density in the Archean at most depths between 20–34 GPa (570 and 900 km). The pyrolite density shows a sharp increase at 23–23.5 GPa because of the post-spinel transition, followed by the gradual increase, contributed by the post-Gt transition that occurs in the larger pressure interval (22.5-28 GPa) at the elevated mantle temperature in the Archean.

The similar patterns of the phase transitions are observed in B30. The B30 density along the AE temperature markedly increases over a pressure interval of 25–26 GPa (Fig. 4.4), because of the phase transformation of Gt and Rw into Brg (Section 4.3.2). The post-spinel transition in B30 at 23 GPa may not increase the density as much as in pyrolite because the lower proportions of Rw (16 and 60 vol%, respectively; Irifune *et al.* (2010); Ishii *et al.* (2018)) forms the limited amount of Brg. The B30 density becomes slightly lower than the pyrolite density at 24–25 GPa. However, the Gt-out

boundary of the post-Gt transition is at shallower depth in B30 than in pyrolite (26 and 28 GPa, respectively) because of the narrower transition thickness (1.7 GPa of the pressure interval) in B30. As a result, B30 becomes denser than pyrolite by 0.1 g/cm^3 above 25 GPa in the AE temperature (Fig. 4.7a).

In the AL temperature, the B30 density is always greater than the pyrolite density at 20–34 GPa (Fig. 4.4). The B30 density notably increases at 24–25 GPa because of the post-Gt transition with the narrow pressure interval (1.7 GPa). The density along the AL temperature is greater than along the AE temperature, because of the thermal expansion. On the other hand, the B30 density along the colder temperatures was not investigated in this study due to the limited number of data points at low temperatures. However, I speculate that the B30 density along the colder temperatures should be even greater than the densities in the AE and AL temperatures because the depths of phase transition into Brg will be shallower and the volumes of the phases will be smaller with lower temperatures.

4.4.2 Comparisons of the B30 Density Between Experiments and Perple_X

To examine possible differences between experiments and theoretical calculations, I used Perple_X (Connolly, 2009) to calculate the densities of B30 for the AL and AE temperatures and compared with the experiments in this study. In Perple_X, I used the Mie-Grüneisun formulation from Stixrude and Lithgow-Bertelloni (2005) and the thermodynamic data of mineral phases from Stixrude and Lithgow-Bertelloni (2011), which has been widely used for multi-phase assemblages in the Earth's mantle conditions (e.g., Nakagawa *et al.*, 2010; Stixrude and Lithgow-Bertelloni, 2012; Klein *et al.*, 2017).

The B30 density appears to be in a good agreement between the experiments and the Perple_X model except for 24.5–28 GPa, where the density from the experiments

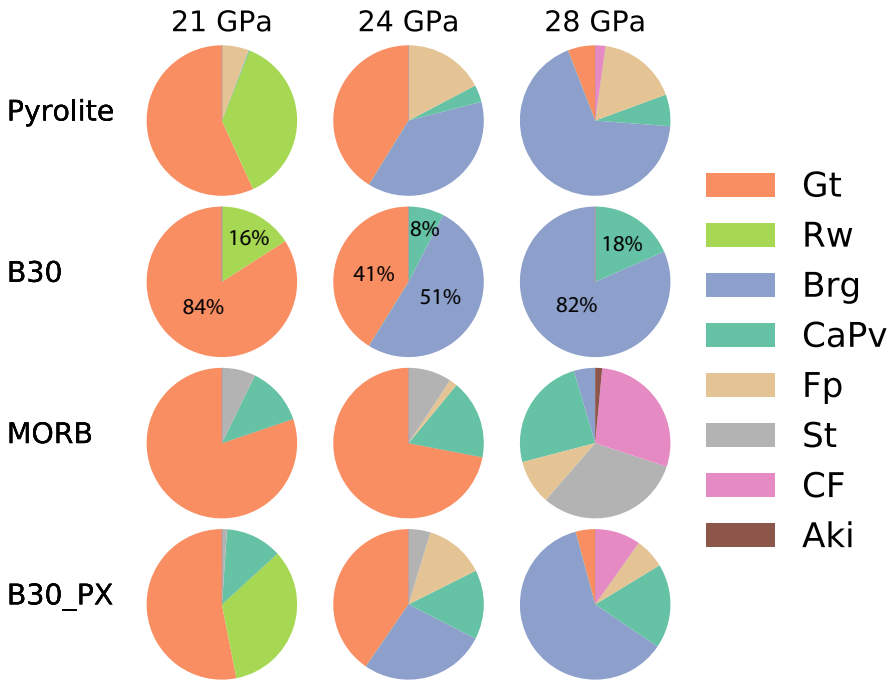

Figure 4.6: The pie charts of the mineralogy for Pyrolite, B30, MORB in vol%. The mineralogy of B30 is from the experimental results in this study. Mineralogies of pyrolite, MORB, and B30_PX were calculated using Perple_X (Connolly, 2009) and the data set from Stixrude and Lithgow-Bertelloni (2011). Gt: garnet; Rw: ringwoodite; Brg: bridgmanite; CaPv: $CaSiO_3$ perovskite; Fp: ferropericlase; St: stishovite; CF: calcium ferrite; Aki: Akimotoite.

becomes much greater (Fig. 4.4). The transition thickness of the post-Gt transition is narrower in the experiments than in the Perple_X model (1.7 and 5 GPa, respectively). The B30 density above 28 GPa in the exepriments is in a good agreement with that in the Perple_X model.

Brg-in boundary is consistent with each other within 1% (23.6 and 23.4 GPa, respectively), whereas the Gt-out boundary is considerably at higher pressure in the Perple_X model than in the experiments (28.1 and 24.8 GPa at 1,700 K, respectively). The discrepancy results in the greater density in the experiments than in the Perple_X

model at 24.8–28 GPa (Fig. 4.4). However, the Clapeyron slopes of the post-spinel and post-Gt transitions are in an excellent agreement between the experiments and Perple_X calculations. The experiments yielded -0.8 ± 0.3 and 3.5 ± 0.5 MPa/K, whereas Perple_X predicted -0.81 MPa/K and 3.1 MPa/K for the post-spinel transition and the post-Gt transition, respectively.

On the other hand, the predicted mineralogy by Perple_X was somewhat different from the experiments (Fig. 4.6). While the major phases, such as, Gt and Brg are the same with different proportions between the experiments and the Perple_X model, the minor phases are additionally predicted from the Perple_X model. For example, in the AL temperature, the Perple_X mineralogy model shows stishovite (Stv) up to 3 vol% together with either Rw or Fp at 21–25 GPa, unlike the experiments (Fig. 4.6). In the AL and AE temperatures, the Perple_X mineralogy model predicted 10 vol% of calcium-ferrite phase above 26 GPa, which was not observed from the experiments. In addition, the Perple_X mineralogy model shows Fp above 24 GPa up to 5 vol%, which was not observed from the experiments either. This is likely caused by the lack of consideration of Fe^{3+} in Brg from the Perple_X model, which ignores the reduction in the number of Fe^{2+} through the disproportionation reaction (Section 4.3.2; Frost *et al.*, 2004). The stoichiometric estimation of Brg from the experiments yields $Fe^{3+}/\Sigma Fe$=57% (Section 4.3.2), which is in a good agreement with the reported values (Frost *et al.*, 2004; Shim *et al.*, 2017).

4.4.3 Density Difference Between the Volcanic Crust and Pyrolite

Fig. 4.7a,b shows density difference of B30 and modern MORB with respect to pyrolite (the surrounding mantle) in the Archean and modern day, respectively. The B30 density is directly from the experiments (Section 4.4.1). The densities of modern MORB and pyrolite were calculated from Perple_X (Section 4.4.2), which are in an

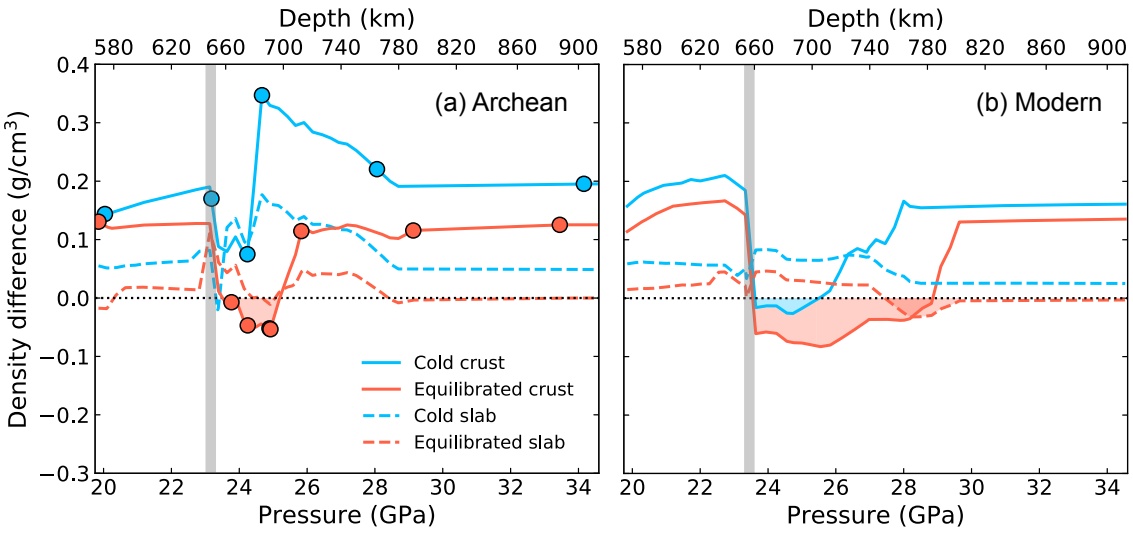

Figure 4.7: Density differences of the crusts and subducting slabs with respect to the pyrolitic mantle (pyrolite): (a) B30 and subducting slab in the Archean and (b) MORB and subducting slab in the modern day. The open circles in (a) represent the experimental data points. The vertical gray bars indicate the depth of the post-spinel transition in the pyrolitic mantle. The depths of the negative density contrast are shaded. For subducting slabs, the thicknesses of crust and harzburgite are 40 and 74 km for Archean, and 7 and 32 km for modern day, respectively (Text 4.4.4). Information on the temperature profiles can be found in Table 4.5.

agreement with previous experiments (Irifune and Ringwood, 1993; Hirose, 2002; Irifune *et al.*, 2010; Ishii *et al.*, 2018). The low temperature profiles for modern MORB (hereafter referred to as ML) were obtained from the temperature model of the subducting model (Klein *et al.*, 2017). The equilibrated temperature for modern MORB (ME) was assumed to be same as the surrounding mantle (Brown and Shankland, 1981).

At 23–23.5 GPa, because of the post-spinel transition in pyrolite, the density difference between B30 and pyrolite drops by less than 0.1 g/cm^3. The drop can be seen

in modern MORB but with a larger magnitude, 0.2 g/cm^3. The proportions of Rw in pyrolite is much smaller in the Archean than in the modern day (30 and 60 vol%, respectively; Fig.S1), therefore the effect of the post-spinel transition on the density increase is smaller in the Archean. The post-Gt transition in B30 and modern MORB increases the density difference, but occurs at the different depths. The increase in the density difference occurs at the lower pressures of 24.5–26 GPa in B30 than at 25–29 GPa in modern MORB, depending on the temperature. If thermally equilibrated with the surrounding mantle (i.e. AE or ME), the density difference of B30 becomes negative only at 24–25 GPa (up to -0.03 g/cm^3), whereas that of modern MORB does at 23.5–29 GPa (up to -0.09 g/cm^3). At the deeper depths, B30 maintains the positive density difference by 0.1-0.2 g/cm^3 at the shallow depth than modern MORB does (26 and 29 GPa, respectively).

4.4.4 Density Difference Between Harzburgite and Pyrolite

Ringwood (1982) proposed a model for the petrological structure of the oceanic lithosphere that is composed mainly of the basaltic crust, harzburgitic, and lherzolitic (depleted pyrolite) lithospheres. The density of the lherzolitic lithosphere should be greater than or at least the same as the surrounding mantle because of the same chemical composition but in the lower temperature or the equilibrated temperature, respectively. Therefore, for the case of the subducting slab the chemical effects on the density of the subducting slab is primarily governed by the harzburgitic lithosphere as well as the crust (Klein *et al.*, 2017; Irifune and Ringwood, 1987a).

When the volcanic crust forms from partial melting of the mantle, it will create complementary residue (harzburgite) beneath the crustal layer. Therefore, the crust and complementary harzburgite have compositional relations with respect to the undepleted mantle (pyrolite). Such relations allow us to estimate the thickness

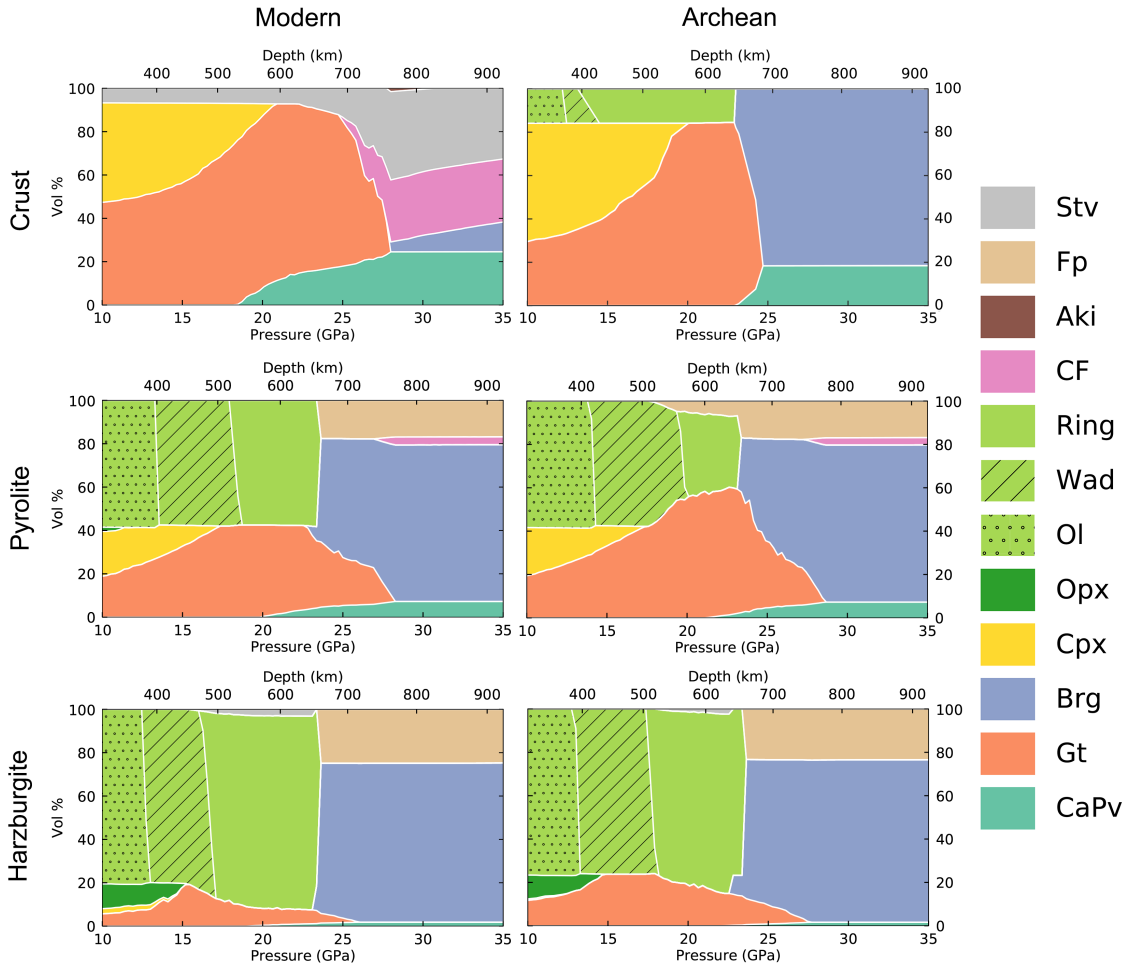

Figure 4.8: Modal proportions (vol%) of (clockwise, from top left) modern MORB, B30, pyrolite in the Archean, Archean harzburgitic lithosphere, modern harzburgitic lithosphere, and pyrolite in the modern day. Phase equilibria were calculated using Perple_X (Connolly, 2009) with thermodynamic data (after Stixrude and Lithgow-Bertelloni, 2011) except for B30 (Archean volcanic crust). For B30, experimental data in the present study were used at 20–35 GPa and extrapolated based on Perple_X model for 10–20 GPa. I used the temperature model of the subducting slab from Klein *et al.* (2017). Modern (Brown and Shankland, 1981) and Archean geotherms (elevated by 200 K with respect to modern geotherm) were used for pyrolite, respectively.

of harzburgitic layer. If I assume their volumes are linearly proportional to their thicknesses, I can describe an equation as follows (Xu *et al.*, 2008):

$$H_{Crust}X_{Crust} + H_{Harz}X_{Harz} = (H_{Crust} + H_{Harz})X_{Pyro} \tag{4.1}$$

where X_{Crust}, X_{Harz}, and X_{Pyro} are the compositions of the crust, complementary harzburgite, and pyrolite, respectively and H_{Crust} and H_{Harz} are the thicknesses of the crust and complementary harzburgite, respectively. With the given thickness of the crust and the compositions of the crust and complementary harzburgite, I can determine the thickness of the complementary harzburgite using the following equation:

$$H_{Harz} = H_{Crust}\frac{X_{Pyro} - X_{Crust}}{X_{Harz} - X_{Pyro}} \tag{4.2}$$

In this study, I used thicknesses of 7 and 40 km for modern and Archean volcanic crusts (i.e. modern MORB and B30), respectively, which yield thicknesses of 32 and 74 km for the modern and Archean complementary harzburgites, respectively (Table 4.1). I used Perple_X to calculate the density of Archean harzburgite. Although the Archean harzburgite has not been cross-examined by both the experiments and Perple_X, unlike the modern harzburgite (Irifune and Ringwood, 1987a; Stixrude and Lithgow-Bertelloni, 2012; Xu *et al.*, 2008), its composition remains very similar to modern harzburgite composition (Table 4.1). Therefore, Archean harzburgite is expected to yield nearly the same mineralogy as modern harzburgite (Fig. 4.8).

The density difference between harzburgite and pyrolite in the Archean and modern day is shown in Fig. 4.9. The calculated mineralogy of harzburgite is nearly the same in between Archean and modern day (Fig. 4.8) because of the similar chemical compositions (Table 4.1). At 20–23.5 GPa, Rw is dominant (80–90 vol%), while Gt represents 10–19 vol% in harzburgite, depending on temperature. Above 23.5 GPa, Brg becomes the most abundant phase and its proportion increases by the post-Gt

transition (70–75 vol%) up to 25.9 and 27.5 GPa, for both the Archean and modern harzburgites, respectively (Fig. 4.8).

The density difference of Archean harzburgite with respect to pyrolite changes with the temperature profile. The AL and AE temperatures have lower densities than pyrolite (Fig. 4.9) except for 23–28 GPa. For the AL temperature, the density difference decreases until at 23.3 GPa due to the post-spinel transition in pyrolite, followed by a sharp increase at 24 GPa because of the post-spinel transition in the Archean harzburgite. For the AE temperature, the density difference abrubtly increases at 23 GPa, because of the post-spinel transition which occurs at the same depth in the Archean harzburgite and pyrolite. Archean harzburgite forms the larger amount of Brg at 23 GPa than pyrolite (53 and 23.5 vol%, respectively) because of the larger amount of Rw (76 and 34 vol%, respectively), leading the steep increase without the sudden drop in density difference. Above 24 GPa, Archean harzburgite shows a gradual decrease in the density difference because of the gradual post-Gt transition in pyrolite until 28.5 GPa. Above 28.5 GPa, Archean harzburgite becomes less dense than pyrolite up to 34 GPa for the AL and AE temperatures, respectively.

Compared to Archean harzburgite, modern harzburgite shows very similar trend in the density difference but with the systemically greater density. The greater density of modern harzburgite may largely be the lower temperature in the modern day. At 23.8 GPa, only the ML temperature shows the sharp decrease (0.15 g/cm^3) in the density difference of modern harzburgite. Because of the negative sign of the Clapeyron slope of the post-spinel transition, the transition depth becomes deeper with the lower temperature. As a result, the post-spinel transition in modern harzburgite with the ML temperature occurs at the deeper depth than that in pyrolite, causing the sudden drop of the density difference, unlike with the ML and ME temperatures.

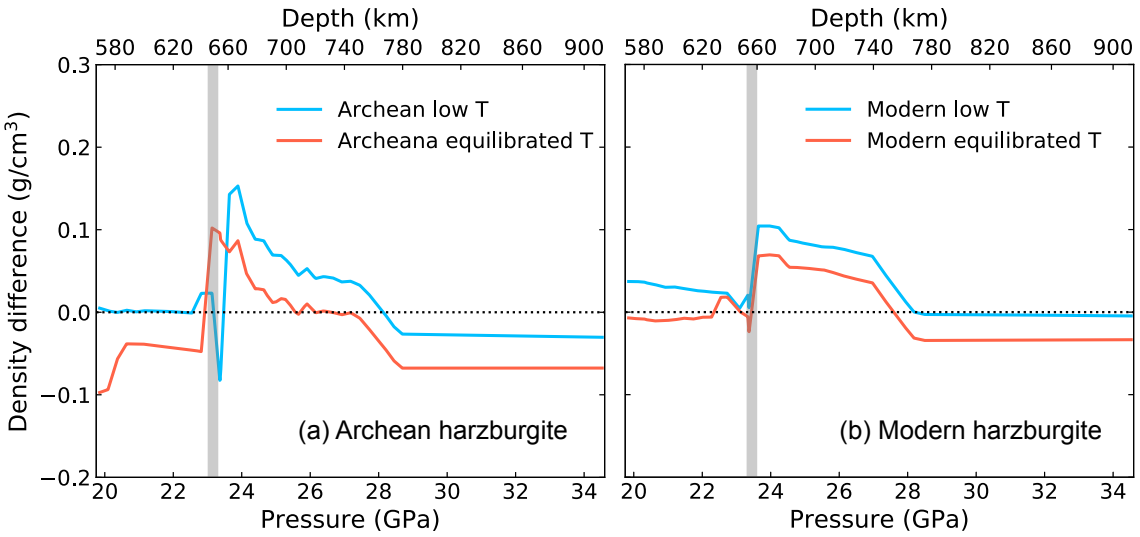

Figure 4.9: Density differences between harzburgite and the pyrolitic surrounding mantle in (a) Archean and (b) modern day. The densities were calculated using Perple_X (Connolly, 2009) with the thermodynamic data set (Stixrude and Lithgow-Bertelloni, 2011). The depths of the post-spinel transition in pyrolite is marked by the vertical grey bars. Information on the temperature profiles can be found in Table 4.5.

4.4.5 Density Difference Between Subducting Slabs and Pyrolite

I calculated the density of the subducting slab by combining the densities of the crust and harzburgite. The density difference of the subducting slab with respect to pyrolite is shown as dashed lines in Fig. 4.7. In the Archean, subducting slabs are equal to or denser than pyrolite in the most depths at 20–34 GPa (Fig. 4.7a). For the AL temperature, because of the post-spinel transition in pyrolite, the density difference drops to -0.01 g/cm^3 at 23.3 GPa. For the AE temperature, the drop in the density difference does not appear because of the shallower depth of the post-spinel transition in the Archean harzburgite at the higher slab temperature (Text 4.4.4). Then, the cold slab maintains the greater density than pyrolite above 28 GPa, while the thermally equilibrated slab becomes equally dense as pyrolite at 29 GPa. On the

other hand, the colder slabs are expected to be even denser than the AL and AE slab cases because of the reduced volume at lower temperatures, therefore the greater density difference with respect to pyrolite.

In modern mantle, the density difference for the ML temperature is always positive at 20–34 GPa (Fig. 4.7b). However, the density difference for the ME temperature becomes negative in 27.5–29.6 GPa because of the persistent Gt in modern MORB at the higher slab temperature. Above, 30 GPa, the density difference for the equilibrated slab becomes -0.01 g/cm^3.

These results suggest that the contribution from the crustal density is much greater in the Archean than in the modern day because of the greater thickness of the crust in the Archean slab (40 and 7 km-thick, respectively).

4.5 Discussion

4.5.1 The Density Behaviors of the Volcanic Crust and Subducting Slab in the Archean

I found that Archean volcanic crust (B30) is denser than the pyrolitic mantle at the most depths of the lower MTZ and the shallow lower mantle regardless of the thermal state of the crust, unlike modern MORB (Fig. 4.7). The different density behaviors of the crust between in the Archean and in the modern day can be attributed to (1) the effect of the Gt composition on the depth of the post-Gt transition in the crust and (2) the temperature effect on the mineralogy of the pyrolitic mantle. First, both Archean volcanic crust and modern MORB have Gt as the most abundant phase (∼80 vol%) in the mineralogy. The composition of Gt differs a lot between the two crusts (Table 4.3), which may affect the depth of the post-Gt transition. For example, the Gt composition in Archean volcanic crust exhibits much smaller Al_2O_3 content

than in modern MORB (4.8 and 13.2 mol%, respectively; Table 4.3). The previous experiments (Irifune *et al.*, 1996) suggested that the Al_2O_3 content may increase the stability of Gt at higher pressure, which is consistent with the observations that Gt-out boundary in Archean volcanic crust is at the shallower depth by 25–50 km-depth (1–2 GPa; Fig.4.2) than that in the modern day. Second, the mineralogy of the pyrolitic mantle may be different depending on temperature. Pyrolite shows only 30 vol% of Rw in the hotter Archean, whereas 60 vol% of Rw in the cooler modern day (Fig. 4.8). The larger Rw proportions in modern-day pyrolite results in the greater increase in the pyrolite density at 660 km-depth through the post-spinel transition. Therefore, the impact on the decrease in the density difference of the crust with respect to the pyrolitic mantle might be much larger in the modern day than in the Archean (Fig. 4.7).

The density models of the subducting slab suggest that the effects on the net density of the slab from the less dense harzburgite are smaller in the Archean than in the modern day (Fig. 4.7). Rather, the greater density of Archean volcanic crust is more effective to the net density of the slab owing to its larger portion in the slab (35 and 18% for Archean volcanic crust and modern MORB, respectively; Table 4.1). As a result, the density contrast between the subducting slab and the pyrolitic mantle is larger in the Archean than in the modern day (Fig. 4.7).

4.5.2 Previous Studies on Candidates for the Subducted Archean Volcanic Rocks

The exact composition of Archean volcanic crust remains uncertain (Herzberg *et al.*, 2010; Herzberg and Rudnick, 2012). Therefore, it is worthwhile to consider the relevant compositions. The mineralogy and density of komatiite in the MTZ and the topmost lower mantle have been documented by previous studies (Klein *et al.*, 2017; Nishihara and Takahashi, 2001). The earlier experiments by Nishihara and Takahashi

(2001) studied Al-depleted komatiite with Di/Si = 1.38 up to 23 GPa. They observed Gt and Rw at 19 GPa, consistent with the experiments in B30 (Section 4.3.1). Brg-in boundary is slightly shallower in Al-depleted komatiite by 0.3 GPa than in B30 although their pressure calibration had a large uncertainty at high pressure (Nishihara and Takahashi, 2001). At 21 GPa, Al-depleted komatiite has the much larger proportion of Rw than B30 (40 and 14 vol%, repectively) because of the higher Di/Si ratio. At 23 GPa, the stable phases of Al-depleted komatiite are Gt + Brg + CaPv + Fp, consistent with B30 in this study except that I did not find Fp (Section 4.3.2) because of the lower MgO content in the B30 composition (32.1 and 22.8 wt%, respectively). They estimated the density of Al-depleted komatiite at high P–T conditionsby thermodynamic calculations based on the zero-pressure densities of the phases (Brown and Shankland, 1981) at 5–23 GPa. Their results showed the greater density of Al-depleted komatiite than PREM density by 0.02–0.44 g/cm^3 in the upper mantle and the MTZ.

Klein *et al.* (2017) proposed a model with the komatiitic composition with the ratio of divalent cations to Si (Di/Si) = 1.12 that is less mafic than the one used in Nishihara and Takahashi (2001) but similar to the B30 composition used in the present study (Table 4.1). In the thermally equilibrated slab, Gt takes up to 92 vol% with minor CaPv and Fp at 20–23 GPa but without Rw. Unfortunately, the experiments does not provide data points to compare at 20–23 GPa along the equilibrated temperature. However, I observed the similar results from the Perple_X mineralogy model of B30 (Section 4.4.2). Klein *et al.* (2017) predicted the greater density of komatiite than the pyrolitic mantle in the Archean except when thermally equilibrated. With the equilibrated temperature, the komatiite density becomes smaller than pyrolite at 24–26 GPa, whereas the B30 density is always greater regardless of the slab temperature.

The general conclusions drawn from Nishihara and Takahashi (2001) and Klein *et al.* (2017) concur with this study in that the density of Archean volcanic crust prefers sinking into the deep lower mantle.

4.5.3 The Sinking Style of Archean Volcanic Crust and the Scale of the Mantle Mixing

Archean volcanic crust might have been transported into the mantle even before the onset of the subduction. Johnson *et al.* (2014) suggested that the base of Archean volcanic crust could have been gravitationally unstable due to the local thickening and eventually delaminated by Rayleigh-Taylor instabilities. The shallow subduction was also proposed by Foley *et al.* (2003). In any scenario, I expect the further sinking of Archean volcanic crust into the lower mantle by Rayleigh-Taylor instabilities at the interface between the MTZ and lower mantle. Therefore, Archean volcanic crust might have been added into the lower mantle regardless of the style of the transportation. However, the volume of the material exchange between the MTZ and lower mantle might have changed after the subduction initiated. If the subduction transported the more amount of the sinking materials into the lower mantle, the whole-mantle mixing might have become more efficient than before. In this case, the mantle mixing with the redox heterogeneities from the lower mantle might have oxidized the upper mantle, eventually leading to the rise of O_2 in the atmosphere toward the GOE (Nicklas *et al.*, 2019; Aulbach and Stagno, 2016; Andrault *et al.*, 2018a).

4.5.4 The Time-dependent Changes in the Scale of Material Circulations in the Mantle

Since the onset of the subduction in the Archean (e.g., Condie and Kröner, 2008; Laurent *et al.*, 2014; Tang *et al.*, 2016), the composition of the subducted volcanic

crust have been changed with time. In this view, modern MORB and Archean volcanic crust can represent the two end-members of the crustal compositions (Herzberg *et al.*, 2010; Johnson *et al.*, 2014). As Earth's mantle cools, the composition of the volcanic crust evolves toward the lower the ratio of Di/Si and more Al, and so the composition of Gt. The change in the Gt composition might have deepen the depth of the post-Gt transition with time. As a result, Gt becomes more stable at the deeper depth, delaying the appearance of Brg, the high-density phase. Also, the thickness of the crust in the slab becomes thinner, and therefore the density contribution from the crust becomes smaller. At the same time, the contribution from the harzburgitic layer becomes more influential in the net density of the subducting slab, if the slab remains mechanically integrated. As shown in Fig. 4.7, the positive density contrast of the subducting slab may have decreased over time.

Today, seismic tomographic images show different states of the modern subducting slabs right beneath the MTZ. Slab stagnation is observed beneath the Western Pacific, whereas subducting slabs seem to directly penetrate into the lower mantle beneath the Central and South American subduction zones (e.g., van der Hilst and Seno, 1993; Fukao *et al.*, 2009; Li and McNamara, 2013; King *et al.*, 2015). As discussed above, the change in the composition and thickness of the crust over time might have reduced the positive density contrast of the subducting slabs, which might partly contribute to the slab stagnation. What I observe from the seismic tomography may be snapshots of the time-dependent transition of the style of the material circulations between the MTZ and the lower mantle. Therefore, the scale of the mantle mixing may be changing from single-layered since Archean to the two-layered in the future (Klein *et al.*, 2017).

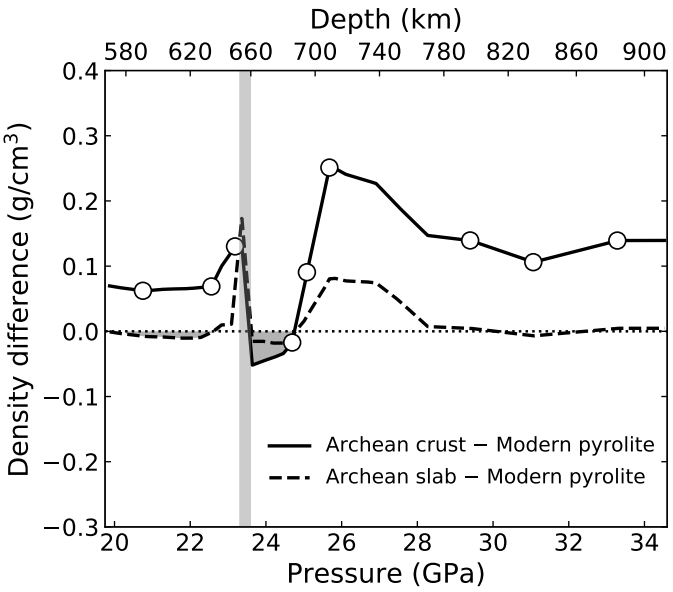

Figure 4.10: The density differences of B30 and Archean subducting slab with respect to the pyrolitic mantle in the modern day. The open circles represent the experimental data in this study. The temperatures of B30 and Archean harzburgite were assumed to be equilibrated to modern mantle (Brown and Shankland, 1981)). The depth of the post-spinel transition in pyrolite is marked as the vertical grey bar. The densities of Archean harzburgite and pyrolite were calculated using Perple_X (Connolly, 2009) and the data set from Stixrude and Lithgow-Bertelloni (2011).

4.5.5 Archean Materials in the Present-day Mantle

The slow diffusion in the lower mantle (Holzapfel *et al.*, 2005) may have allowed Archean volcanic crust to survive until the present day. Such materials can contribute to the seismic heterogeneities observed in the present-day mantle (Frost *et al.*, 2017; Wu *et al.*, 2019). Particularly, a recent study raised the possibility of an accumulation of ancient oceanic crust at 660 km-depth for the cause of small-scale seismic structures (Wu *et al.*, 2019). In order to evaluate the effect of density on the buoyancy of Archean volcanic crust and Archean subducting slab in the pyrolitic modern mantle,

I calculated the densities of B30 and Archean harzburgite. The temperature for the crust and slab was assumed to be the same as the surrounding mantle, therefore thermally equilibrated (Brown and Shankland, 1981). The B30 density was obtained based on the experimental data (Fig. 4.2), while those of Archean harzburgite and modern pyrolite were calculated using Perple_X (Connolly, 2009) and the data set from Stixrude and Lithgow-Bertelloni (2011). For Archean subducting slab, I assumed thicknesses of 40 and 74 km-thick for the crust and harzburgitic layer, respectively (Table 4.1).

I found that B30 remains much denser than the pyrolitic mantle by 0.1 g/cm^3 in most depths between 580 and 900 km-depth (Fig. 4.10). If detached, the density of Archean volcanic crust in the present-day mantle may prefer sinking into the lower mantle to staying at 660 km-depth. In this case, the possible ancient oceanic crust at 660 km-depth that Wu *et al.* (2019) suggested is unlikely originated from Archean but more likely sometime close to present day. For the case of th integrated slab, the density of Archean slab appears to be the same as the modern mantle density at most depths between 580 and 900 km-depth because the lower density of Archean harzburgite cancels out the greater density of B30 (Fig. 4.10). Therefore, the density effect on the buoyancy of Archean slab in the modern mantle at these depths may be negligible.

4.5.6 Improving Mineralogy Modeling for Earth-like Planets

From the stellar elemental abundance, I can infer the bulk chemical compositions of the exoplanets around the stars (Bond *et al.*, 2010; Young *et al.*, 2014; Unterborn and Panero, 2017). Such studies have found a surprisingly large range of Mg/Si ratios for the compositions. For the rocky exoplanets, Mg and Si are often assumed to exclusively compose the mantle minerals. Therefore, in order to model the dynamics

and structures of the interior of the rocky exoplanets, it is important to have capability to predict mineralogy from a range of different compositions. Because of the large parameter space and the paucity of experimental data for such a large range of Mg/Si ratio, thermodynamics codes, such as Perple_X, have become important tools to model the mineralogy of the exoplanetary mantle (e.g. Dorn *et al.*, 2015; Unterborn *et al.*, 2017; Vance *et al.*, 2018).

Such thermodynamics codes have been successful to reproduce the phase relations observed in experiments for Earth's mantle-related compositions, such as pyrolite and MORB, as also demonstrated in my modeling. Besides these two compositions, there are little data at sufficiently high pressure to examine the predicted models through comparison with experimental data. The new data presented here provide the mineralogy with the significantly lower Mg/Si ratio than pyrolite, which is an important opportunity to test the modeling capability for the large range of Mg/Si ratio for the possible mantle compositions.

Section 4.4.2 compares the mineralogy and the density between the experiments and Perple_X model in this study. While the density remains similar to each other at 20–34 GPa (Fig. 4.4), the minor phases were additionally found in Perple_X model, partly because of the lack of consideration of Fe^{3+} in the data set (Stixrude and Lithgow-Bertelloni, 2011). This difference might be the reason for the different chemical compositions of the major phase, such as Gt, which may in turn result in the different depths of the phase transition (24.8 and 28.1 GPa for the Gt-out boundary in the experiments and Perple_X model, respectively). However, because the density and the major phase is similar between the experiments and Perple_X model in the rest of depths (20–24 GPa and 28–34 GPa), I speculate these similarity may continue in the depths of the shallower mantle and the deeper mantle. Gt is known to be

stable throughout the upper mantle and the MTZ (Irifune *et al.*, 1996), while the Rw composition can exist in other forms of polymorphs, such as olivine and wadsleyite (Nishihara and Takahashi, 2001). In the lower mantle, Brg and CaPv should persist up to ∼100 GPa because of the large stability of the perovskite structure (Irifune *et al.*, 2010). Therefore, despite of some differences in the mineralogy and phase transition behaviors at 25–28 GPa, the use of Perple_X with the data set from Stixrude and Lithgow-Bertelloni (2011) can be effective for modelling the mantle mineralogy and density of Earth-like planets with the low Mg/Si ratio.

4.6 Conclusion

I have conducted experiments to investigate stable phases and density relations between Archean volcanic crust and Archean subducting slab in the pyrolitic mantle at conditions related to the lower MTZ and shallow lower mantle. The experiments showed that Archean volcanic crust is denser than the pyrolitic mantle regardless of temperature, increasing the likelihood of penetrating the lower MTZ where modern MORB may experience the slab stagnation beneath some subduction zones. I also modelled the density of the subducting slab in a combination of the densities of the crust and the harzburgitic layer, with respect to the pyrolitic mantle for both Archean and modern day. The models predicted that the positive density contrast between the subducting slab and the pyrolitic mantle is larger in the Archean than in the modern day. The results suggest that the density and the large thickness of Archean volcanic crust might have promoted the further sinking into the lower mantle in any transportation style. Therefore, the mantle mixing between the MTZ and the lower mantle might have been efficient in the Archean.

Chapter 5

THE MINERALOGY AND DENSITY OF THE ANCIENT VOLCANIC CRUSTS IN THE EARTH'S LOWER MANTLE

5.1 Introduction

Subduction is the major way of transportation of the oceanic crust to the Earth's deep interior. The oceanic crust is mainly composed of mid ocean ridge basalt (MORB), which contains a significant amount of SiO_2 and Al_2O_3. On the contrary, the mantle composition is peridotitic, enriched with MgO. The chemical distinction between the oceanic crust and the mantle creates the differences in mineralogy and physical properties such as density.

5.1.1 Chemical Heterogeneities in the Lower Mantle

Tomographic images have shown that the subducting slabs beneath some subduction zones traverse from the upper mantle to regions at the base of the mantle (e.g. Fukao *et al.*, 2009), suggesting that the subducted oceanic crust can form chemical heterogeneities in the lower mantle. Once chemical heterogeneities form, they can be preserved for a long time in the lower mantle because of the slow chemical diffusion under high pressure in the lower mantle (Holzapfel *et al.*, 2005; Stixrude and Lithgow-Bertelloni, 2012). Therefore, the chemical heterogeneites are often used to account for the observed seismic anomalies in the lower mantle. For example, the small-scale topography at 660 km-depth (Wu *et al.*, 2019), strong scatterers at ∼1400–1700 km-depth (Kaneshima, 2016; Haugland *et al.*, 2017; Wang *et al.*, 2020), and ultralow

shear velocity zones (ULVZs; He and Wen, 2009; Rost *et al.*, 2010; Wicks *et al.*, 2017; Yu and Garnero, 2018) above the core-mantle boundary (CMB).

5.1.2 Large Low Shear Velocity Provinces (LLSVPs)

Seismic tomography revealed anomalously large structures called large low shear velocity provinces (LLSVPs) at the bottom of the mantle beneath the Pacific Ocean and south Africa (Ishii and Tromp, 1999; Grand, 2002; Garnero *et al.*, 2016; Dziewonski *et al.*, 2010; Garnero and McNamara, 2008). Although its origin is an ongoing debate between the purely thermal models and the thermo-chemical models, anti-correlation of bulk and shear moduli (Masters *et al.*, 2000) and the strong gradients in shear wave velocity along margins of the LLSVPs (Thorne *et al.*, 2004; Garnero *et al.*, 2016) imply that the LLSVPs are compositionally distinct from the surrounding mantle.

Geodynamic studies have suggested that the thermo-chemical piles can be stabilized at the base of the mantle as long as their intrinsic density is greater than the surrounding mantle by a few percent (McNamara and Zhong, 2005; Bull *et al.*, 2009; Nakagawa *et al.*, 2009; Mulyukova *et al.*, 2015; Li and McNamara, 2018). A number of models for dense materials has been proposed, which can be classified into two in general: 1) an accumulation of subducted oceanic crust (MORB; Christensen and Hofmann, 1994; Hirose *et al.*, 2005; Brandenburg and Van Keken, 2007; Nakagawa *et al.*, 2009; Frost and Rost, 2014; Mulyukova *et al.*, 2015); and 2) the primordial material that is the remnant of differentiation processes of the early mantle (Becker *et al.*, 1999; Tolstikhin *et al.*, 2006; Labrosse *et al.*, 2007; Lee *et al.*, 2010; Carlson *et al.*, 2014; Zhang *et al.*, 2016).

The former models have been supported by high P–T experiments suggesting that the subducted crust (MORB) is denser than the surrounding lower mantle (Hirose

et al., 1999, 2005; Ricolleau *et al.*, 2010). However, geodynamic models have predicted that the accumulation of the present-day crust would be hampered by the plume-associated mantle convection because the crust is too thin (∼7 km-thick) to survive the viscous mantle stirring (Li and McNamara, 2013).

The models of Fe-rich primordial melt have been suggested to account for the origin of the thermo-chemical piles. Fe-rich liquid sank as droplets from the magma ocean to the CMB in early Earth and formed a layer of dense melt, which becomes dense piles through crystallization over time (Labrosse *et al.*, 2007). Lee *et al.* (2010) proposed that dense melt was collected (trapped) between the upper mantle and transition zone, which eventually sank to the CMB after crystallization. These models of Fe-rich melt explain the larger density of the LLSVPs than the background mantle, which can stabilize the structure of the LLSVPs for a long period of time (McNamara and Zhong, 2005; Bull *et al.*, 2009; Nakagawa *et al.*, 2009; Mulyukova *et al.*, 2015; Li and McNamara, 2018). However, the other major elements in the composition, such as Si, Al, and Mg are not constrained, the mineralogy of which remains uncertain.

On the other hand, chemical reaction between the lowermost mantle and the outer core has been suggested (Dubrovinsky *et al.*, 2003). In this model, liquid Fe and silicate mineral may react to form Fe-Si alloy which accumulates above the CMB (Dubrovinsky *et al.*, 2003). However, if this is the case, such chemical reaction should occur globally at the CMB and form a thin layer of an Fe-Si alloy, which cannot explain the locations and shapes of the LLSVPs.

Alternatively, Deschamps *et al.* (2012) suggested that the Si- and Fe-rich primitive material would have formed the Brg-dominant mineralogy with the elevated Fe content compared to the normal mantle. This composition can explain the anti-correlation of shear-wave velocity and bulk-sound velocity as well as the elevated density of the LLSVPs, but its origin still remains unclear (Davies *et al.*, 2015).

5.1.3 Compositions of Ancient Volcanic Crusts

In fact, the suggested composition by Deschamps *et al.* (2012) lies in the middle of pyrolite and modern MORB in terms of the (Mg,Fe,Ca)/Si ratio. Pyrolite has the high (Mg,Fe,Ca)/Si ratio (1.49), whereas modern MORB has the low (Mg,Fe,Ca)/Si ratio (0.63; Table 5.1). In the past, volcanic crusts would have formed with the composition which is between pyrolite and modern MORB in terms of the the Mg/Si ratio. In the Archean, for example, the potential mantle temperature would have been much higher than the present day by approximately 200 K (Korenaga, 2008; Herzberg *et al.*, 2010). The warmer mantle would have formed much mafic composition (higher (Mg,Fe,Ca)/Si ratio) of the volcanic crust through partial melting compared to modern MORB but still less mafic than pyrolite (Table 5.1; Herzberg *et al.*, 2010; Johnson *et al.*, 2014). As the mantle cools down over time, the composition of the volcanic crust should have changed with decreasing the (Mg,Fe,Ca)/Si ratio. Table 5.1 compares the compositions of volcanic crusts formed in the past (B30 for Archean volcanic crust and B15 for Proterozoic volcanic crust) with modern MORB and pyrolite.

Furthermore, the ancient volcanic crusts would have been much thicker up to ∼40 km than modern MORB (∼7 km) because of the extensive partial melting in the warmer mantle in the past during the formation processes. The thicker crusts might have overcome the mantle stirring and accumulated above the CMB. However, whether the ancient volcanic crusts had reached to the CMB remains uncertain due to the limited knowledge of the mineralogy and the buoyancy of the ancient crusts in the lower mantle.

In this study, I show the experimental results of the densities of the B30 and B15 compositions in order to investigate the buoyancy of Archean and Proterozoic

volcanic crusts in the lower mantle. I conducted in-situ X-ray diffraction experiments in the laser-heated diamond anvil cell (LHDAC) to synthesize the stable phases of the B30 and B15 compositions in the lower-mantle related conditions. The measured densities of the B30 and B15 compositions suggest that the negative buoyancy of the ancient crusts, promoting their sinking throughout the lower mantle.

Table 5.1: Chemical compositions of pyrolite, Archean volcanic crust (B30), Proterozoic volcanic crust (B15), and the present-day MORB. Each composition was normalized to 100%.

wt%	Pyrolite[a]	B30[b]	B15[b]	MORB
SiO_2	45.1	47.0	48.1	51.8
Al_2O_3	4.8	7.5	12.7	15.5
FeO	8.4	12.7	9.2	10.1
MgO	37.7	22.8	17.8	8.0
CaO	3.5	8.8	10.4	11.7
Na_2O	0.4	1.3	1.8	2.1
(Mg+Fe+Ca)/Si	1.49	1.15	0.94	0.63

[a] McDonough and Sun (1995)
[b] Johnson *et al.* (2014).

5.2 Experimental Methods

5.2.1 Starting Materials

In this study, two compositions were used for the volcanic crusts that could have formed 3.0 Ga in the Archean (B30) and 1.5 Ga in the Proterozoic (B15), respectively (Also see Section 2.1 in Chapter 4; Johnson *et al.*, 2014). Table 5.1 compares the B30 and B15 compositions with modern MORB. The B30 composition is a komatiitic composition that was also used in Chapter 4. The B15 composition is a basaltic composition but more mafic (higher (Mg,Fe,Ca)/Si ratio) than modern MORB. The

starting materials were synthesized as homogeneous glasses using the laser-levitation method (Tangeman *et al.*, 2001).

The compositions and homogeneity of starting materials were confirmed in an electron probe micro analyzer (JEOL JXA-8530F EPMA) combined with wavelength-dispersive X-ray spectrometer (WDS) at Arizona State University (ASU) (Table 5.1).

5.2.2 Laser-heated Diamond-anvil Cell Experiments

The starting glasses were powdered and mixed with ∼10 wt% of Au powder (grain size of 1–3 μm). Au served as a pressure standard and a laser absorber in the laser-heated diamond-anvil cell (LHDAC) experiments. The mixture was compressed to thin foils with a size of 30–200 μm and a thickness of ∼10 μm. Then, the foil was loaded into a hole in a pre-indented rhenium gasket with a micro-manipulator (Micro-support Axis Pro SS) at ASU. The four spacers (<10 μm sized pure sample particle) were placed between the sample foil and each side of the diamond culets for the gas or liquid medium loading. I loaded Ne and Ar in the COMPRES-GSECARS high-pressure gas loading system (Rivers *et al.*, 2008) or the cryogenic liquid loading system at ASU. I compressed the samples in the symmetric-type diamond-anvil cell with 150-bevel, 200, and 400 μm-sized culet for the target pressures of ∼35, 65, and 100 GPa, respectively.

5.2.3 In-situ X-ray Diffraction Experiments

I have conducted LHDAC experiments combined with in-situ X-ray diffraction (XRD) at sector 13-IDD of the GeoSoilEnviroConsortium (GSECARS) in the Advanced Photon Source (APS; Prakapenka *et al.*, 2008). For the XRD measurements, the monochromatic X-ray beams of 0.3344 and 0.4133 Å are used. I focused the laser beams on both sides of the sample and aligned the laser beams coaxially with the X-

ray beam by visually observing X-ray fluorescence, in order to measure XRD patterns at the center of the laser heating spot. The typical beam diameters for X-ray and the laser were ∼5 and 20 μm, respectively. I fit the thermal radiation spectra measured from both sides of the sample to Planck gray-body equation for the estimation of temperature.

The XRD images were collected with a MarCCD or a Dectris Pilatus detector. The images were then integrated to 1D diffraction patterns with the calibration parameters obtained from the LaB_6 standard in the DIOPTAS software (Prescher and Prakapenka, 2015). The collected diffraction patterns were analyzed and fitted with a pseudo-Voigt profile function to obtain the peak positions in the PeakPo software (Shim, 2017a). The unit-cell parameters were obtained by using the PeakPo and UnitCell softwares (Holland and Redfern, 1997). For St, the unit-cell volumes were calculated by using the equation of state parameters from Wang *et al.* (2012) due to the the limited number of available XRD lines. I determined pressures with the equation of state (EOS) of Au (Dorogokupets and Dewaele, 2007) using the Pytheos software (Shim, 2017b). From in-situ XRD patterns I have observed that the glass samples transformed into crystalline phases within 5–60 seconds depending on temperature.

The B30 and B15 samples were synthesized at 1) ∼35 GPa and 2,200 ± 200 K (A33 and P34, respectively); 2) 65 GPa and 2,450 ±350 K (A65 and P65, respectively); and 3) 100 GPa and 2,300 ± 200 K (A100 and P100, respectively). Note that A33, A65, and A100 are identical samples as K33, K65, and K100 in Chapter 4.

5.2.4 Chemical Analysis

I recovered the synthesized samples of 1) A33 and A100 for the B30 composition; and 2) P34 and P100 for the B15 composition by using a micro-manipulator. The

samples were processed for the STEM measurements in a focused ion beam (FIB; FEI Nova 200 and FEI Helios) at ASU and University of Arizona (UofA), respectively. I extracted the center part of the heated area and mounted it on a Cu or Mo grid. The compositions of the samples were analyzed in the aberration-corrected scanning transmission electron microscope (STEM): JEOL ARM200F at ASU and Hitachi HF-5000 at UofA combined with energy-dispersive X-ray spectroscopy (EDS). A 120 and 200 keV of acceleration voltages were used at ASU and UofA, respectively. I measured standard spectra from the starting glass materials for the data analysis. I performed a 2D scan to obtain the chemical maps for A100 and P100 (Fig. 4.3). I also performed a point analysis with exposure time of 20–40 seconds depending on the beam sensitivity at a target grain. The collected EDS spectra were fitted using a python code LMFIT (Newville *et al.*, 2016).

5.3 Results

5.3.1 The Mineralogy of the Ancient Crusts in the Lower Mantle

As described in Section 3.3.3 in Chapter 3, the B30 composition forms the different mineral assemblages depending largely on the synthesis pressures. At 33 GPa, I observed the XRD patterns of Mg-Brg and CaPv as major phases with minor stishovite (St; Fig 5.1a). The chemical analysis confirmed the XRD observations (Table 5.2). Based on the measured unit-cell volumes and compositions of the phases, the mass balance calculations yielded 84.3, 14.3, and 1.3 vol% for Mg-Brg, CaPv, and St, respectively in A33 (A33; Table 5.2).

Similar to the B30 composition, the XRD patterns of the B15 composition at 34 GPa show Mg-Brg and CaPv as major phases with minor alumina (Al_2O_3) and St (P34; Fig 5.1b). The mass balance calculations based on the chemical analysis

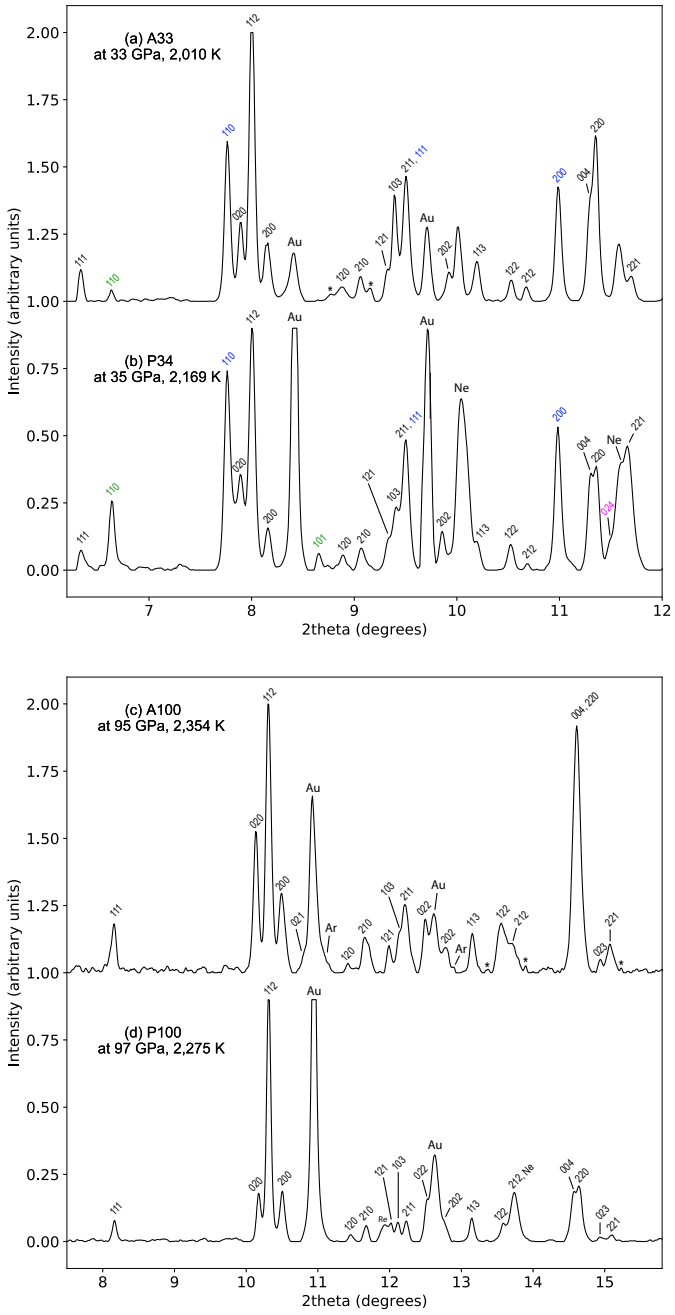

Figure 5.1: In-situ X-ray diffraction (XRD) patterns of the B30 (a,c) and B15 (b,d) compositions at high P–T in laser-heated diamond anvil cell (LHDAC). X-ray energies were 37 (a,b,c) and 30 keV (d). Miller indices of bridgmanite (black), $CaSiO_3$ perovskite (blue), stishovite (green) and Al_2O_3 (magenta) are provided. Au: gold (pressure standard); Ar: argon (medium); Ne: neon (medium); and $*$: unidentified peaks.

yielded 63.2, 22.1, 8.2, and 6.5 vol% for Mg-Brg, CaPv, Alumina, and St, respectively in P34 (Table 5.3).

The XRD intensities of St 110 and St 101 are stronger in P34 than in A33, consistent with the estimated larger proportions of St in P34. Alumina 024 is identified in P34, which is not observed in A33. The other lines of alumina are difficult to resolve because of the overlap with the stronger lines of Mg-Brg in P34. Mg-Brg exists as matrix that surrounds grains of the other phases in both A33 and P34. Due to the small grain size of alumina in P34, the composition measurements on the alumina grains seem to include the Mg-Brg matrix. Therefore, I subtracted the measured composition of the alumina grains with the Mg-Brg composition in order to extract the alumina composition (Table 5.3).

The larger amount of St and the presence of alumina in P34 are because of the compositional difference of the B15 composition from the B30 composition. In the B15 composition, the amount of Mg and Fe is smaller, whereas the amounts of Si and Al are greater than in the B30 composition (Table 5.1). The more amounts of the SiO_2 and Al_2O_3 components in the B15 composition formed the more Si- and Al-bearing phases. This difference is also found in the compositions of Mg-Brg in A33 and P34. The Mg-Brg composition in P34 shows the smaller amounts of Mg and Fe but the larger amounts of Si and Al components than in A33 (Table 5.3,5.2).

At the higher pressures, the mineralogies of the B30 and B15 compositions become different from the mineralogy at the low pressures. For the B30 composition, the XRD patterns of A65 and A100 show Ca-Brg as a dominant phase (Fig 5.1c). As shown in Fig. 3.5, the chemical analysis on A100 revealed that Ca-Brg surrounds minor silica (presumably $CaCl_2$-type silica; e.g. Tsuchiya *et al.*, 2004a; Nomura *et al.*, 2010) and alumina grains, consistent with the XRD observations (Table 5.2). The mass balance calculations based on the measured compositions of the phases yielded 94.7,

Table 5.2: Chemical compositions of recovered samples of the B30 Composition. The compositions were normalized to be 100% in total.

	A33: 33 GPa, 2,200 K			A100: 100 GPa, 2,300 K		
wt%	Mg-Brg	CaPv	silica	Ca-Brg	silica	Alumina
SiO_2	46.7	48.1	95.6	47.4	89.2	0.0
Al_2O_3	9.5	1.1	0.7	7.3	3.3	97.8
FeO[a]	13.5	4.6	1.5	13.3	1.9	2.2
MgO	27.4	3.4	1.5	22.2	3.8	0.0
CaO	2.8	42.8	0.7	9.9	1.9	0.0
Vol%	84.3	14.3	1.3	94.7	3.1	2.2

[a]All Fe is assumed to be Fe^{2+}.

Table 5.3: Chemical compositions of recovered samples of the B15 composition. The compositions were normalized to be 100% in total.

	P34: 34 GPa, 2,200 K				P100: 100 GPa, 2,350 K		
wt%	Mg-Brg	CaPv	Alumina[b]	silica	Ca-Brg	Alumina	silica
SiO_2	48.5	52.9	2.6	93.4	48.1	0.0	88.3
Al_2O_3	11.1	6.0	96.0	4.3	12.6	95.9	8.7
FeO[a]	11.7	0.0	1.1	0.0	8.5	4.1	0.0
MgO	26.3	0.0	0.0	1.8	19.3	0.0	0.0
CaO	2.2	41.1	0.2	0.5	11.6	0.0	3.0
Vol%	63.2	22.1	8.2	6.5	96.2	2.1	1.7

[a]All Fe is assumed to be Fe^{2+}.

[b]The alumina composition was subtracted with the Mg-Brg composition due to the overlapping grains from the measurements.

3.1, and 2.2 vol% for Ca-Brg, St, and alumina, respectively in A100 (Table 5.2). Given that the XRDs show the nearly same patterns between A65 and A100, the chemical compositions and phase proportions of A65 are assumed to be very similar to those of A100. The notable difference from the lower-pressure sample (A33) is the absence of CaPv in A65 and A100 (see also Chapter 3). The significant amount of Ca (9.9 wt%) was measured in Ca-Brg in A100 (Table 5.2). Another difference is that alumina was observed in A65 and A100, unlike A33. The Al content is smaller in Ca-Brg of A100 by 2.2% than in Mg-Brg of A33, consistent of the presence of alumina as a separate phase (Table 5.2).

The B15 composition shows the nearly same mineralogy as the B30 composition at the higher pressures. The XRD patterns of P65 and P100 show Ca-Brg as the dominant phase with minor alumina and silica. The XRD observations are consistent with the STEM images where alumina and silica are found as small grains (up to 100 nm) in the chemical analysis on P100, while Ca-Brg exists as a matrix. The mass balance calculations yielded 96.2, 2.1, and 1.7 vol% for Ca-Brg, alumina and st, respectively (Table 5.3). The proportions of silica and alumina are smaller in P100 than in A100 despite of the larger contents of Si and Al in the B15 composition than in the B30 composition. Ca-Brg contains more Si and Al in P100 than in A100, compensating the smaller proportions of alumina and silica in the mineralogy of P100. In particular, compared to Ca-Brg in A100, Ca-Brg in P100 has considerably more Al_2O_3 (12.6 and 7.3 wt%, respectively) but much less FeO (13.3 and 8.5 wt%, respectively).

5.3.2 The Density Profiles of the B30 and B15 Compositions in the Lower Mantle

Densities of the B30 and B15 compositions at high temperatures (2,200–2,400 K) were calculated based on the unit-cell volumes at in-situ high P–T measurements and

the chemical compositions from the recovered samples (Fig. 5.2). For the samples synthesized at higher pressures (A65, A100, P65, and P100), silica and alumina were excluded from the density calculation (i.e. only Ca-Brg was considered). The vol% of Ca-Brg is >95% in these samples, therefore the effects of the densities of the minor phases on the bulk density of the rock would be negligible.

While the density profiles of both the B30 and B15 compositions are greater than the PREM density, the density difference with respect to the PREM density is much larger for the B30 composition than for the B15 composition (1.0–1.7% and 0.2–0.9%, respectively). The density profile of the B30 composition is systemically greater by 0.3–0.9% than that of the B15 composition. The greater density of the B30 composition is because primarily of the greater amount of heavier elements in the B30 composition, such as Fe (Table 5.1). For example, the FeO content in Ca-Brg is larger in A100 than in P10 (13.3 and 8.5 wt%, respectively; Table 5.2,5.3). The larger FeO content results in the greater molar mass of Ca-Brg in A100 by 0.9% than in P100. Although the unit-cell volume of Ca-Brg is smaller in A100 by 0.4% than in P100, the difference in mass is larger, resulting in the greater density of A100 (Fig. 5.2).

On the other hand, the density of the present-day MORB (Ricolleau *et al.*, 2010) is plotted for comparison as the dashed line in Fig. 5.2. The MORB density is nearly the same as the densities of the B30 and B15 compositions at ∼35 GPa. However, the MORB density becomes larger than those of the B30 and B15 compositions at higher pressures up to 105 GPa.

5.3.3 Equation of State of Bridgmanite

The equations of state of Mg-Brg and Ca-Brg in the B15 composition at 300 K are presented in Fig. 5.3. The unit-cell volume of Mg-Brg is slightly smaller in the B15 composition than in the B30 composition. At 1 bar, Mg-Brg in the B15 composition is

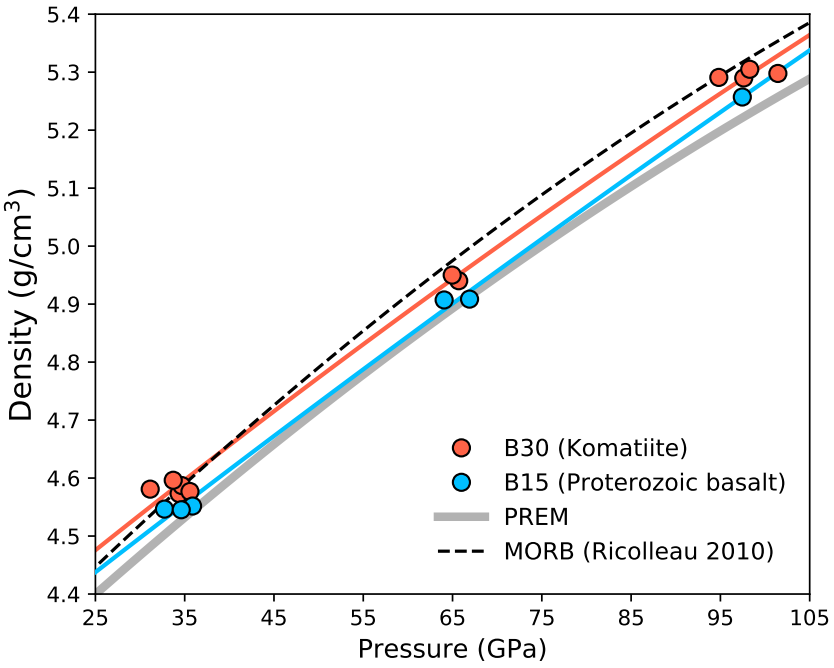

Figure 5.2: Density profiles of the B30 and B15 compositions at high P–T conditions of the lower mantle. The dashed line is the density profile of the present-day MORB along 2,400 K from Ricolleau *et al.* (2010). The PREM density is plotted as a grey line for comparison.

only smaller by 0.3%, but the difference becomes larger with increasing pressure. This observation suggests that Mg-Brg in the B15 composition is more compressible. The bulk modulus of Mg-Brg at room conditions (K_0) is smaller in the B15 composition than in the B30 composition (244.6 and 247.5 GPa, respectively; Table 5.4). This can be explained by the compositional difference of Mg-Brg between the B15 composition and the B30 composition. Mg-Brg in the B15 composition contains more Al_2O_3 (11.1 and 9.5 wt%, respectively) but less FeO (11.7 and 13.5 wt%, respectively) than in the B30 composition (Table 5.2, 5.3). K_0 of Mg-Brg is decreased by Al_2O_3 (Walter *et al.*, 2004a), but increased by FeO (Dorfman *et al.*, 2013).

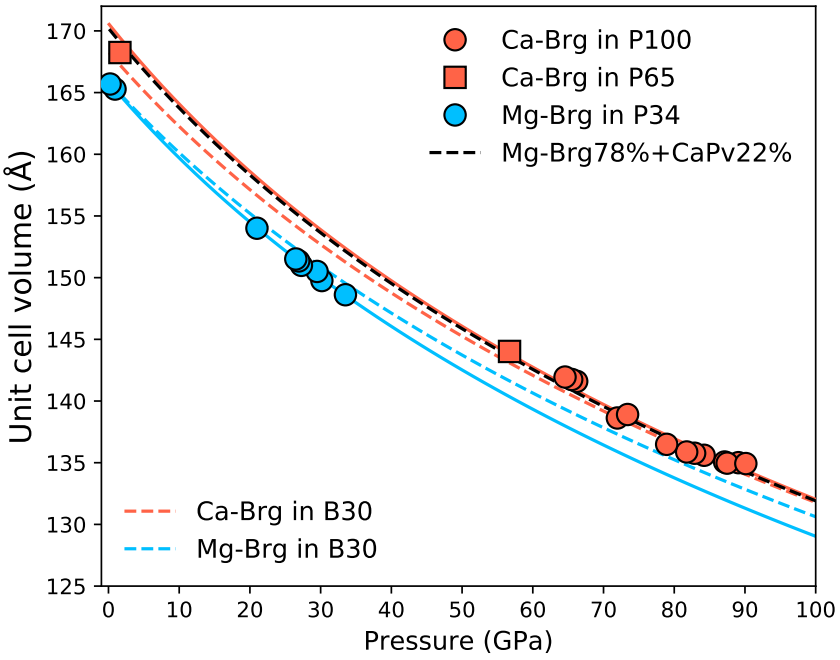

Figure 5.3: The compressibility of bridgmanite in the B15 composition at 300 K. The data for the unit-cell volume of bridgmanite were obtained from decompression measurements. The red and blue circles represent Ca-bridgmanite (Ca-Brg) and Ca-low bridgmanite (Mg-Brg), respectively. The solid curves are fits to the Vinet equation of state. The combined volume of Mg-Brg (78 %) and $CaSiO_3$ perovskite (22 %) is plotted as the dashed black curve for comparison. The blue and red dashed curves represent the volumes of Mg-Brg and Ca-Brg from the B30 composition, respectively (Section 3.3.4 in Chapter 3).

The unit-cell volume of Ca-Brg in the B15 composition is larger than those of Mg-Brg, consistent with the B30 composition (Fig. 5.3; see also Section 3.3.4 in Chapter 3). However, the difference in volume between Ca-Brg and Mg-Brg is twice larger in the B15 composition (2.9%) than in the B30 composition (1.4%). The larger amount of Ca in Ca-Brg in the B15 composition than in the B30 composition (11.6 and 9.9 wt%, respectively; Table 5.2,5.3) can be responsible for the larger expansion of the Ca-Brg structure. In addition to Ca, Al increases the volume of Brg (e.g. Walter *et al.*, 2004a) as well. Ca-Brg in the B15 composition contains 12.6 wt% of Al_2O_3 (Table 5.3), which is ∼60% larger than 7.3 wt% of Al_2O_3 in Ca-Brg in the B30 composition (Table 5.2).

The volume of Ca-Brg in the B15 composition at 300 K is compared with the combined volume of Mg-Brg and CaPv (Fig. 5.3). The proportions of Mg-Brg and CaPv were obtained from the mass balance calculations based on the chemical compositions of P34. The comparison shows the nearly same volume between Ca-Brg and Mg-Brg + CaPv in the B15 composition. The difference seems to be within the experimental error, consistent with the observations on the B30 composition (Section 3.3.4 in Chapter 3).

Table 5.4: Vinet equation of state parameters for Ca-bridgmanite (Ca-Brg) and Ca-low bridgmanite (Mg-Brg) at high pressure and 300 K. K_0' was fixed as 4 for all fits. Δ represents the difference between Ca-Brg and Mg-Brg. Dorogokupets and Dewaele (2007) was used for the gold pressure scale.

Composition	Brg type	V_0 (Å^3)	K_0 (GPa)	$\Delta\ V_0$ (Å^3)	$\Delta\ K_0$ (GPa)
B30	Ca-Brg	168.3(0)	254.3(1)	1.9	6.0
	Mg-Brg	166.3(7)	247.5(8)	(1.2%)	(2.4%)
B15	Ca-Brg	170.6(0)	237.4(5)	4.7	−7.2
	Mg-Brg	165.8(7)	244.6(4)	(2.9%)	(−3.0%)

5.4 Discussion

5.4.1 The Mineralogical Effects on the Viscosity and Compressibility of the Ancient Crusts

The results in this study show that the majority of the mineralogy in the B30 and B15 compositions is Brg at the P–T conditions of the lower mantle. Mg-Brg is the most abundant phase at ∼34 GPa (84.3 and 63.2 vol% for the B30 and B15 compositions, respectively), while Ca-Brg becomes the most abundant phase at 65 and 100 GPa (94.7 and 96.2 vol% for the B30 and B15 compositions, respectively). This mineralogy suggests that the physical properties of ancient crusts in Archean and Proterozoic would largely depends on those of Mg-Brg and Ca-Brg.

The most notable difference in mineralogy between the ancient crusts and pyrolite is that the ancient crusts do not have ferropericlase (Fp) in their mineralogy. In pyrolite, Fp is the second most abundant phase (18 vol%; Irifune *et al.*, 2010; Ishii *et al.*, 2018) in the lower mantle, which plays an important role in the viscosity and compressibility of the lower mantle. The absence of Fp would have made the ancient crusts more viscous and less compressible than the pyrolitic lower mantle. The previous studies showed that the viscosity of Fp is two orders of magnitude smaller than that of Brg (Yamazaki and Karato, 2001; Ammann *et al.*, 2010). Also, recent experiments (Girard *et al.*, 2015) showed that the presence of Fp can induce the shear localization in the lower mantle because of the substantially weak shear strength of Fp. Assuming Fp is internally connected (Yamazaki and Karato, 2001; Yamazaki *et al.*, 2014) in the surrounding mantle, the shear strain can be localized in the layers of Fp in the surrounding mantle, whereas the viscous ancient crusts remain intact. In addition, the ancient crusts would be less compressible than the pyrolitic mantle because Fp is much compressible than Brg (Chapter 3.4.4). For example, K_0

is 148–177 GPa for Fp (Finkelstein *et al.*, 2017), whereas 254.3 and 237.4 GPa for Ca-Brg in the B30 and B15 compositions, respectively.

5.4.2 Density Relations of the Ancient Crusts with Respect to the Lower Mantle

The mantle would have been warmer by ∼200 and ∼100 K in the Archean and Proterozoic, respectively (e.g. Herzberg *et al.*, 2010). The density of the lower mantle would have been lower in ancient times of the Archean and Proterozoic than in the present day because of the thermal expansion, if the chemical composition of the lower mantle remains unchanged. The present study showed that the densities of the B15 and B30 compositions are systematically greater than the PREM density throught the lower mantle. The density difference between the B15 composition and PREM appears to be relatively small (only 0.2% at 65 GPa). However, the density difference between the B15 composition and PREM may not be the case for the Proterozoic because the PREM density reflects the present-day mantle density, not the Proterozoic mantle when the mantle was hotter (Korenaga, 2008; Herzberg *et al.*, 2010). The thermal expansion would have reduced the density of the hotter mantle in the Proterozoic. Therefore, the ancient crusts would have been denser than the surrounding mantle in the past, promoting their sinking into the base of the mantle.

5.4.3 Accumulation of the Ancient Volcanic Crusts Near the CMB

The thickness of the ancient crusts (up to 40 km; Herzberg *et al.*, 2010) could increase the chance of the accumulation at the base of the mantle for billions of years. As discussed in Sector 5.4.1, the ancient crusts would be more viscous than the pyrolitic mantle because of the absence of Fp, which is also in favor of the accumulation of the ancient crusts.

In the deep lower mantle, the ancient crusts would have >90 vol% of Brg with elevated FeO (13.3 and 8.5 wt% for the B30 and B15 compositions, respectively; Table 5.2, 5.3), compared to pyrolite which has 80 vol% of Mg-Brg with <7 wt% of FeO (Hirose, 2002). The compositions of the ancient crusts are consistent with the composition model suggested by Deschamps *et al.* (2012) (90% of Brg with the 50% more FeO compared to pyrolite) to explain the anti-correlation of the shear wave velocity and the bulk sound velocity of the LLSVPs (i.e. low shear wave velocity and the high bulk sound velocity). The bulk moduli (K_0) of the ancient crusts would be larger than that of the pyrolitic mantle because of the absence of Fp in the ancient crusts (Section 5.4.1).

The shear wave velocity (V_S) of the ancient crusts was not measured in this study. However, I calculated V_S of the B30 and B15 compositions by using a thermodynamic program Perple_X (Connolly, 2009). The thermodynamic dataset from Stixrude and Lithgow-Bertelloni (2011) was used for the calculation. Note that the Perple_X calculations do not consider the Ca incorporation into Brg, and hence always form CaPv in the B30 and B15 compositions in the *P*–*T* conditions of the lower-mantle. The calculated results are shown as the V_S difference of the B30 and B15 compositions with respect to pyrolite in Fig. 5.4. At 2,100–2,890 km-depth, V_S of the B30 and B15 compositions are slower than pyrolite except for 2,550 km-depth where V_S of the B15 composition becomes faster than pyrolite. The V_S differences for the B30 and B15 compositions are -1 to -2.5 and 0 to -2 km/s, respectively, depending on temperature at 2,100–2,890 km-depth. The negative V_S differences become much larger at 2,550–2,650 km-depth (-2.5) for both compositions because of the appearance of post-perovskite (pPv) in pyrolite, which has much faster V_S than Brg. In pyrolite, the phase transformation from Brg to pPv occurs at ∼2,550 km-depth, decreasing the V_S difference. In the B30 and B15 compositions, the transformation occurs at

the deeper depths (2,600–2,650 km-depth depending on temperature), because of the compositional difference, increasing the V_S difference.

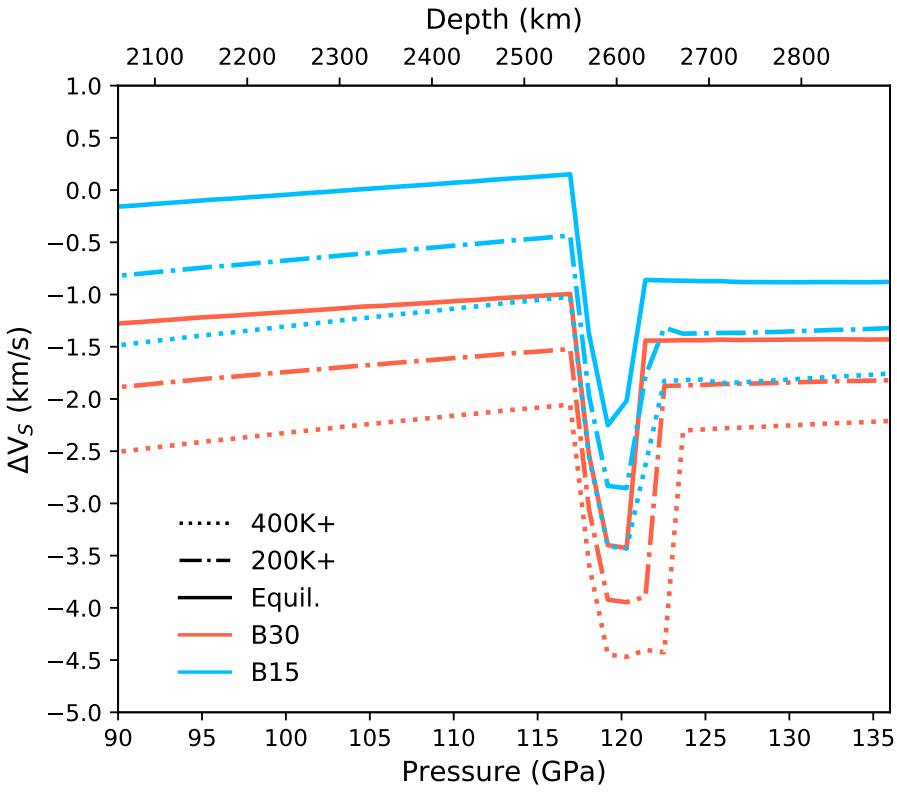

Figure 5.4: Modelled shear velocity profiles of the B30 and B15 compositinos with respect to pyrolite. The shear velocities are calculated by using Perple_X with thermodynamic data from (Stixrude and Lithgow-Bertelloni, 2011). Note that the calculated mineralogy includes $CaSiO_3$ perovskite for both compositions. 'Equil.' represent the equilibrated temperature to the surrounding mantle.

In the calculated models, Brg in the B30 and B15 compositions contains substantially more amount of Fe and Al than in pyrolite, which deepens the lower boundary of the post-perovskite transition and increases the transition thickness (Catalli *et al.*, 2009). As discussed in Chapter 4.42, the Perple_X models assume all Fe is Fe^{2+} (i.e. excluding Fe^{3+} in the calculations) and ignore the effects of Fe^{3+} on the transition

depth. The dominant valence state of Fe in Brg and pPv is known to be Fe^{3+} (∼60%; McCammon, 1997; Sinmyo *et al.*, 2008). However, Fe^{3+} has similar effects to Fe^{2+} which deepens the transition depth with increased transition thickness (Catalli *et al.*, 2009). Therefore, the low V_S difference at ∼2,600 km-depth for the B30 and B15 compositinos would still exist even if Fe^{3+} is taken into account.

On the other hand, the shear modulus of CaPv used in the calculation may be overestimated, which increases V_S of the B30 and B15 compositions. The recent measurements (Greaux *et al.*, 2019; Thomson *et al.*, 2019) on the shear modulus of CaPv showed the much lower values than the earlier prediction (Stixrude and Lithgow-Bertelloni, 2011) which was used in the calculated models. If the new values are used for the calculations, the V_s of the B30 and B15 compositions would be smaller (Greaux *et al.*, 2019; Thomson *et al.*, 2019).

In addition, the incorporation of Ca in Brg makes the structure less distorted, which can potentially affect the shear modulus of Brg significantly relative to the bulk modulus of Brg. This means that knowledge of the effect of the Ca incorporation in Brg on shear modulus is critical to better evaluate whether the B30 and B15 compositions are viable candidates for the chemical origin of the LLSVPs.

5.5 Conclusions

This study investigated the mineralogies and densities of Archean and Proterozoic volcanic crusts experimentally. I found that Archean and Proterozoic crusts would have been denser than the surrounding lower mantle, promoting their descent to the CMB. In addition, I found that the ancient crusts are mostly composed of Brg without Fp, which increases their viscosity. Combined with the greater density and viscosity, the large thickness of the ancient crusts would have allowed them to accumulate in the

region. This study suggests that the ancient crusts would have accumulated above the CMB and formed the LLSVPs since the Archean.

Chapter 6

CONCLUSIONS

6.1 The Mineralogy of the Earth's Lower Mantle

Exploring the chemistry and structure of bridgmanite (Brg) is of paramount importance to understanding the mineralogy of the lower mantle. My experiments on the Ca solubility in Brg open up the new possibility that Brg accommodates a large-sized cation Ca in the A-site in the conditions of the deep lower mantle. The incorporation of Ca causes a decrease in the octahedral tilting and an expansion of the unit-cell volume of Brg.

The results of this study imply that the Earth's lower mantle is not mineralogically homogeneous. In the shallow lower mantle (SLM), Ca-low Brg (Mg-Brg), ferropericlase (Fp), and $CaSiO_3$ perovskite (CaPv) are stable as the major phases, whereas only Ca-bearing Brg (Ca-Brg) and Fp are stable as the major phases in the deep lower mantle (DLM) where the temperature is higher than 2,250 K. The bulk modulus at 300 K (K_0) of Ca-Brg is slightly larger than that of Mg-Brg in pyrolite, thus K_0 of the Ca-Brg + Fp assemblage in the DLM would be larger than that of the Mg-Brg + Fp + CaPv assemblage in the SLM. Also, the absence of CaPv in the DLM would increase the bulk modulus (less compressible) of the Ca-Brg + Fp assemblage even further because of the lower bulk modulus of CaPv (K_0=223 GPa at fixed K_0'=4 Chen *et al.*, 2018) than that of of Brg (K_0∼250 GPa at fixed K_0'=4; Table 3.3).

On the other hand, the absence of CaPv would increase the shear modulus the Ca-Brg + Fp assemblage because of the low shear modulus of CaPv in the lower mantle (Greaux *et al.*, 2019; Thomson *et al.*, 2019). If the shear modulus of Ca-Brg is

nearly the same as that of Mg-Brg, the shear modulus of the Ca-Brg + Fp assemblage would be larger than that of the Mg-Brg + Fp + CaPv assemblage.

In addition, the Ca dissolution in Brg may change the rheology of the lower mantle. Although viscosity is difficult or even impossible to be measured experimentally, it can be inferred by using the homologous melting temperature scaling, an empirical model that relates melting temperature to activation enthalpy (e.g. Sherby *et al.*, 1970; Karato, 1981). In the lower mantle, viscosity η can be described as:

$$\eta = A\frac{RT}{\Omega}\frac{G^2}{D} \tag{6.1}$$

where A is a constant, Ω is the molar volume, R is the gas constant, T is temperature, D is diffusion coefficient, and G is grain size of the material. At constant pressure, the diffusion coefficient can be expressed as a function of the activation enthalpy in Arrhenius equation as followed:

$$D = D_0 exp[-\Delta H/RT] \tag{6.2}$$

where D_0 is the pre-exponential factor and ΔH is the activation enthalpy. The following equation shows the correlation between the activation enthalpy and the melting temperature:

$$\Delta H = gRT_m \tag{6.3}$$

where g is a constant and T_m is the melting temperature at constant pressure. By substituting Equation 6.3 for the activation enthalpy in Equation 6.2, the diffusion coefficient can be written as follows:

$$D = D_0 exp[-gT_m/T] \tag{6.4}$$

where T/T_m is referred to as homologous temperature. Then, the viscosity can be

written as:

$$\eta = A\frac{RT}{\Omega}\frac{G^2}{D_0}exp[-gT_m/T] \tag{6.5}$$

which shows the correlation between viscosity and melting temperature.

For mantle silicate minerals in the upper mantle, the substitution of Mg^{2+} with Fe^{2+} is known to reduce the melting temperature (e.g. Zhao *et al.*, 2009). If this is the case of Brg in the pyrolitic composition, which contains a substantial amount of Fe, its melting temperature would be lower than pure $MgSiO_3$ Brg (Akins *et al.*, 2004). The present study found that the effects of Fe^{2+} and Ca^{2+} on crystal structure and bulk modulus of Brg are very similar. I speculate that Ca would reduce the melting temperature of Brg, and hence the melting temperature of Ca-Brg would be lower than that of Mg-Brg in the pyrolitic composition. Therefore, the viscosity of Ca-Brg would be lower than that of Mg-Brg.

In addition, the absence of CaPv may increase or decrease the bulk viscosity of the Ca-Brg + Fp assemblage although the viscosity of CaPv has not been investigated by previous studies or the present study. Nonetheless, whether the viscosity of CaPv is larger or smaller than that of Brg, the absence of CaPv will make a difference in terms of the bulk viscosity between the Ca-Brg + Fp and Mg-Brg + Fp + CaPv assemblages.

One may argue that the effects of the presence or absence of CaPv on the physical properties between the SLM and the DLM are not seismically detectable because of the low abundance of CaPv in the pyrolitic lower mantle (∼5%; e.g. Irifune *et al.*, 2010). However, the physical properties of the bulk rock depend greatly on the geometry of the constituent components (e.g. Handy, 1994). If the secondary phase is internally connected, the properties of the bulk rock can be controlled by those of the secondary phase (e.g. Yamazaki *et al.*, 2014).

This study did not investigate the shear modulus of Ca-Brg. Shear velocity measurements on Ca-Brg should be followed in the future to evaluate the seismic detectability of Ca-Brg with the absence of CaPv in the deep lower mantle.

6.2 The Evolution of the Scale of the Mantle Mixing

The higher temperature of the Archean mantle has the two main effects on the volcanic crust: 1) the ultramafic composition; and 2) the larger thickness. My experiments suggest that in the deep transition zone, the ultramafic composition of Archean volcanic crust forms ringwoodite (Rw) as the secondary phase, unlike modern MORB which forms stishovite (St) instead of Rw. Because of the existence of Rw, the denser phase of Brg appears in the shallower depths in Archean volcanic crust than in modern MORB. As a result, Archean volcanic crust is denser than pyrolite at most depths in 580–900 km-depth, regardless of the temperature of Archean volcanic crust.

In addition, my density models for the harzburgite layer of the subducting slab showed that the harzburgite layer is less dense than the crust in both the Archean and the present day. However, thanks to the larger fraction of the crustal layer in the Archean subducting slab, the density of the subducting slab is still denser than pyrolite at 580–900 km-depth in the Archean. The results suggest the negative buoyancy of the crust and the subducting slab in the Archean at the depth of the deep transition zone and the topmost lower mantle. In the present day, the fraction of modern MORB in the subducting slab is much smaller than in the Archean. Therefore, the density of the harzburgite layer of the modern slab becomes more influential in the net density of the slab. The modern subducting slab becomes less dense than pyrolite at 660–700 or 750–790 km-depth depending on the slab temperature.

The sinking behavior of a subducting slab is controlled by viscosity as well as buoyancy. As discussed in Chapter 1.2.4, the mantle viscosity depends primarily

on temperature and water content. The higher temperature of the mantle in the Archean would heat up the subducting slab faster because of the larger thermal gradient within the slab. However, the competing effect is the larger thickness of the Archean slab, which results from the extensive partial melting of the hotter mantle in the Archean. The larger thickness would allow the subducting slab to stay cold longer in the Archean.

While multiple lines of evidence support that the present-day mantle contains the significant amount of water in the transition zone (Bercovici and Karato, 2003; Huang *et al.*, 2005; Pearson *et al.*, 2014), the water content in the Archean mantle is very little known (Korenaga, 2018) due to a paucity of evidence. Therefore, the question whether the viscosity contrast between the subducting slab and the surrounding mantle was larger in the Archean remains.

The present study suggest that in the Archean, the positive density contrast of the subducting slab with respect to the surrounding mantle is in favor of the slab descent into the lower mantle. The Archean subducting slabs would have experienced less or no stagnation at the topmost lower mantle, unlike modern subducting slabs. Assuming that the viscosity contrast between the subducting slab and the surrounding mantle in the Archean is the same as that in the present day, the mass exchange between the upper mantle and lower mantle might have been more efficient in the Archean, supporting the whole-mantle convection.

6.3 The Chemical Heterogeneities in the Lower Mantle

The volcanic crust is chemically distinctive from the pyrolitic mantle, which can form the chemical heterogeneities in the deep lower mantle, such as the large low shear velocity provinces (LLSVPs) at the base of the mantle (Ishii and Tromp, 1999; Grand, 2002; Garnero *et al.*, 2016; Dziewonski *et al.*, 2010; Garnero and McNamara,

2008). On the present-day Earth, the volcanic crust forms from the partially-molten mantle near the surface and travels back to the mantle in the form of subduction. These processes of the material circulation would have been going on for at least 2.5–3.5 billion years since the onset of subduction (e.g., Condie and Kröner, 2008; Laurent *et al.*, 2014; Tang *et al.*, 2016).

I found that ancient volcanic crusts (3.0–1.5 Ga) would have formed nearly pure Brg in the lower mantle, resulting in the larger density than the surrounding mantle. The positive density contrast of the ancient crusts with respect to the surrounding mantle would have facilitated their sinking throughout the lower mantle. The ancient volcanic crusts were also much thicker compared to the present-day oceanic crust (∼45 and 7 km-thick, respectively), increasing the likelihood of the accumulation above the core-mantle boundary (CMB).

Chemical diffusion is extremely slow under high pressure in the deep mantle (e.g. Holzapfel *et al.*, 2005; Xu *et al.*, 2011) such that the ancient crusts can last for billions of years, particularly with their large thickness. Stixrude and Lithgow-Bertelloni (2012) suggested the length scale l over which chemical diffusion is operative:

$$l = \sqrt{D\tau} \tag{6.6}$$

where D is the diffusion coefficient and τ is time interval. The diffusion rate of the lower mantle (D_{LM}) can be estimated by the diffusion rate of Brg (D_{Brg}), since D_{LM} is largely governed by the slowest diffusivity, D_{Brg} (Ammann *et al.*, 2010; Ito and Toriumi, 2010). Using D_{Brg} in Equation 6.6, only ∼1 m of l is calculated for 3 billion years.

Indeed, the diffusion rate is sensitive to temperature, and thus can be enhanced in the hotter regions in the lower mantle like the LLSVPs, which are often interpreted as the thermo-chemical piles (e.g. Trampert *et al.*, 2004; McNamara and Zhong, 2005;

Garnero *et al.*, 2016). Also, the mantle was hotter in the past by up to ∼200 K (Korenaga, 2008; Herzberg *et al.*, 2010). Fig. 6.1 illustrates D_{Brg} in the lower mantle depending on temperature. At 750 km-depth, for instance, D_{Brg} increases with increasing temperature from $\sim 10^{-18.5}$ to $\sim 10^{-17}\,m^2s^{-1}$ at 400 K higher temperature than the mantle geotherm (Fig. 6.1). The increased D_{Brg} yields only ∼3 m of l for 3 billion years. This calculation indicates that in order for chemical diffusion to be effectively operative, l needs to be reduced to few meters.

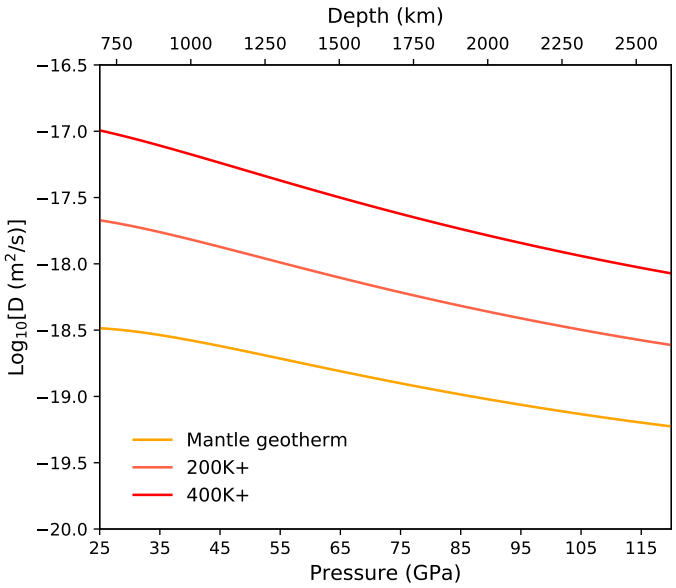

Figure 6.1: Comparison of diffusion rate of bridgmanite depending on temperature. The mantle geotherm is obtained from Katsura *et al.* (2010).

The viscous mantle flow can reduce the thickness of the ancient crusts. The thinning rate can be expressed as follows:

$$h = h_0 exp(\dot{\varepsilon}\tau) \tag{6.7}$$

where h_0 is the initial thickness and $\dot{\varepsilon}$ is the strain rate (Spence *et al.*, 1988). Although the strain rate of the lower mantle is not well constrained, it is typically assumed to

be $\sim 10^{-16}$ if the diffusion creep dominates the deformation in the lower mantle (e.g. Karato, 2010). With this value, the time interval (τ) is estimated to be 3 billion years for the 25–45 km-thick crust to reach 3 m of the length scale over which the chemical diffusion becomes effective.

The present study suggests that the crust has accumulated above the CMB since 3.0 Ga. Although it is hard to constrain how extensive the subduction was and how large the subducting slabs were in the past, the continuous accumulation for billions of years would have enabled the crusts to form or at least contribute to forming the large-scaled thermo-chemical piles above the CMB. However, an important question pertains to how the chemistry of such piles has evolved, while the chemical composition of the accumulating crust has gradually changed. As discussed above, the chemical diffusion in the lower mantle is too slow to form a homogeneous composition. I envision that the accumulated crusts would exist as mechanically-mixed fragments with the complicated chemical structure within the piles.

6.4 The Mineralogy and Rheology of the Si-rich Mantle

The Mg/Si ratio of terrestrial exoplanets can widely range from < 0.9 to > 2.0 based on the stellar elemental abundance (Bond *et al.*, 2010; Young *et al.*, 2014; Unterborn and Panero, 2017). Assuming that Mg and Si are exclusively assigned to form the mantle minerals and that the upper mantle and the lower mantle is chemically homogeneous, the B30 composition used in this study can be applied to infer the mineralogy of the Si-rich mantle in Earth-like exoplanets.

In fact, the divalent cations (Mg + Fe + Ca) to Si ratio can be more reasonable to use as a mineralogy index than the Mg/Si ratio. Mg^{2+}, Fe^{2+}, and Ca^{2+} are the major divalent cations in Earth's mantle, which commonly form solid solutions in the silicate mantle minerals. For example, Brg can form the chemical formula of

(Ca,Mg,Fe)SiO_3—although the incorporation of Ca in Brg depends on temperature (Chapter 3).

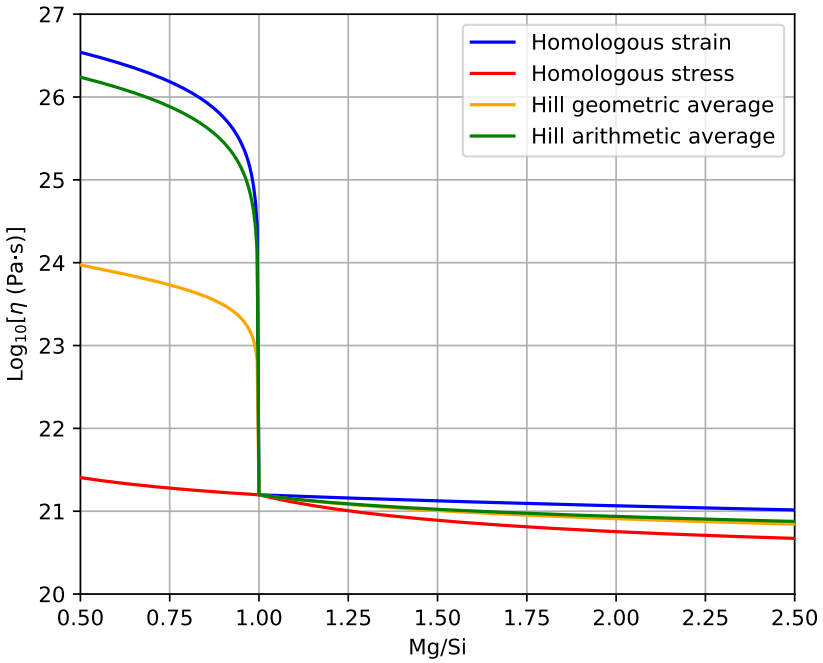

Figure 6.2: Viscosity of the lower mantle in Mg-Si-O system as a function of the Mg/Si ratio. Viscosity was calculated at fixed pressure and temperature of 50 GPa and 2,100 K, respectively.

The (Mg + Fe + Ca)/Si ratio of B30 is much lower (1.15) than that of pyrolite (1.49). My experiments found that the B30 mineralogy includes the SiO_2 phase as a minor phase (3 vol%; Table 5.2) but no Fp, unlike pyrolite that includes ~20% of Fp besides Brg in the lower-mantle conditions (Hirose, 2002; Irifune *et al.*, 2010). Given the fact that the Brg viscosity is ~2 orders of magnitude greater than the Fp viscosity (Yamazaki and Karato, 2001; Ammann *et al.*, 2010), the absence of Fp can make the Si-rich mantle more viscous than pyrolite. Also, the presence of the SiO_2 phase can increase the bulk viscosity of the Si-rich mantle. The viscosity of St is several orders

of magnitude greater than that of Brg, because of the slower Si diffusion in St than in Brg (Xu *et al.*, 2017). At the deeper depth in Earth's mantle, St transforms into $CaCl_2$-type SiO_2 at ∼70 GPa (e.g. Karki *et al.*, 1997; Murakami *et al.*, 2003; Tsuchiya *et al.*, 2004a; Nomura *et al.*, 2010; Fischer *et al.*, 2018), which further transforms into seifertite (α-PbO_2-type SiO_2) at ∼120 GPa (e.g. Karki *et al.*, 1997; Murakami *et al.*, 2003; Tsuchiya *et al.*, 2004a). The viscosities of these higher-pressure polymorphs of SiO_2 have not been investigated by any study yet. Assuming the viscosity remains similar among the polymorphs, the bulk viscosity of the lower mantle can be inferred in a range of the Mg/Si ratio.

I calculated the viscosity of the lower mantle in the Mg-Si-O system as a function of the Mg/Si ratio (Fig. 6.2) at 50 GPa and 2,100 K. In the calculations, I simplified the mineral assemblage such that if Mg/Si >1, the Brg + Fp assemblage forms and if Mg/Si <1, the Brg + St assemblage forms. The homologous melting temperature scaling was used for the calculations (Equation 6.1–6.4). The viscosities of Brg, Fp, and St were calculated based on the thermodynamic data from Yamazaki and Karato (2001) for Brg and Fp and Xu *et al.* (2017) for St. Note that only St was considered for the SiO_2 phase because of the lack of available diffusivity data for $CaCl_2$-type SiO_2 and seifertite. The bulk viscosity of the two-phase rock depends heavily on the geometry of the constituent phases (e.g. Handy, 1994). Handy (1994) suggested the two composite models for the two-phase rock: 1) a load-bearing framework (LBF) where the weaker phase is isolated and surrounded by the stronger phase (homologous strain); and 2) interconnected layers of weak phase (IWL) where the weaker phase is internally connected (homologous stress). The bulk viscosity of the two-phase rock was calculated for these two models based on the relationship between the viscosity contrast and the density contrast of the two phases (Takeda, 1998).

Fig. 6.2 shows the calculated viscosity profiles at 50 GPa and 2,100 K for the LBF model and IWL model as the blue and red curves, respectively. Hill's geometric and arithmetic averages of the two models are also plotted as the yellow and green curves, respectively. The calculated results suggest that the effect of the secondary phase on the bulk viscosity is much larger with St than with Fp (Fig. 6.2). The lower-mantle viscosity increases exponentially even with a small amount of St except for the case of the IWL model (Xu *et al.*, 2017). Therefore, the larger viscosity of the Si-rich lower mantle may decrease the vigor of the mantle convection. Also, this estimation emphasizes the importance of the mineralogy and the geometry of the phases on the viscosity of the lower mantle in Earth's like exoplanets.

It should be noted that the other common elements in stellar abundance, such as Fe, Al, and Ca, must be taken into account to infer the rheology of the lower mantle. For example, the dominant valence state of Fe can be either Fe^{2+} or Fe^{3+} in silicate minerals like Brg depending on the redox state of the mantle. Fe^{2+} substitutes Mg^{2+} in Brg, whereas Fe^{3+} substitutes either Mg^{2+} or Si^{4+} in Brg. In the latter case, the substituted Si^{4+} by Fe^{3+} can form a separate phase of SiO_2. Therefore, the redox state of the mantle can alter the mineralogy of the lower mantle. This means that the (Mg + Fe + Ca)/Si ratio cannot be directly converted to the mineral assemblage of the mantle, but requires careful approaches.

The rheology of the Brg + St system (Si-rich lower mantle) has never been investigated experimentally, unlike the Brg + Fp system (Girard *et al.*, 2015). Experimental studies of the rheological behavior of the Brg + St system as well as the effects of the redox condition on the mineralogy of the lower mantle need to be carried out in the future for better understanding of the compositional effects on the dynamics of the lower mantle.

REFERENCES

Akins, J. A., S.-N. Luo, P. D. Asimow and T. J. Ahrens, "Shock-induced melting of mgsio3 perovskite and implications for melts in earth's lowermost mantle", Geophysical Research Letters 31, 14 (2004).

Ammann, M., J. Brodholt, J. Wookey and D. Dobson, "First-principles constraints on diffusion in lower-mantle minerals and a weak d// layer", Nature 465, 7297, 462 (2010).

Andrault, D., N. Bolfan-Casanova and N. Guignot, "Equation of state of lower mantle (al, fe)-mgsio3 perovskite", Earth and Planetary Science Letters 193, 3-4, 501–508 (2001).

Andrault, D., M. Muñoz, G. Pesce, V. Cerantola, A. Chumakov, I. Kantor, S. Pascarelli, R. Rüffer and L. Hennet, "Large oxygen excess in the primitive mantle could be the source of the great oxygenation event", Geochemical Perspectives Letters 6, 5–10 (2018a).

Andrault, D., G. Pesce, M. A. Bouhifd, N. Bolfan-Casanova, J.-M. Hénot and M. Mezouar, "Melting of subducted basalt at the core-mantle boundary", Science 344, 6186, 892–895 (2014).

Andrault, D., G. Pesce, G. Manthilake, J. Monteux, N. Bolfan-Casanova, J. Chantel, D. Novella, N. Guignot, A. King, J.-P. Itié *et al.*, "Deep and persistent melt layer in the archaean mantle", Nature Geoscience 11, 2, 139 (2018b).

Arevalo, R., W. F. McDonough and M. Luong, "The k/u ratio of the silicate earth: Insights into mantle composition, structure and thermal evolution", Earth and Planetary Science Letters 278, 3, 361–369 (2009).

Asahara, Y., E. Ohtani, T. Kondo, T. Kubo, N. Miyajima, T. Nagase, K. Fujino, T. Yagi and T. Kikegawa, "Formation of metastable cubic-perovskite in high-pressure phase transformation of ca (mg, fe, al) si2o6", American Mineralogist 90, 2-3, 457–462 (2005).

Aulbach, S. and V. Stagno, "Evidence for a reducing archean ambient mantle and its effects on the carbon cycle", Geology 44, 9, 751–754 (2016).

Badro, J., "Spin transitions in mantle minerals", Annual Review of Earth and Planetary Sciences 42, 231–248 (2014).

Badro, J., G. Fiquet, F. Guyot, J.-P. Rueff, V. V. Struzhkin, G. Vankó and G. Monaco, "Iron partitioning in earth's mantle: toward a deep lower mantle discontinuity", Science 300, 5620, 789–791 (2003).

Baker, M. B. and J. R. Beckett, "The origin of abyssal peridotites: a reinterpretation of constraints based on primary bulk compositions", Earth and Planetary Science Letters 171, 1, 49–61 (1999).

Becker, T. W., J. B. Kellogg and R. J. O'Connell, "Thermal constraints on the survival of primitive blobs in the lower mantle", Earth and Planetary Science Letters 171, 3, 351–365 (1999).

Bédard, J. H., "A catalytic delamination-driven model for coupled genesis of archaean crust and sub-continental lithospheric mantle", Geochimica et Cosmochimica Acta 70, 5, 1188–1214 (2006).

Bercovici, D. and S.-i. Karato, "Whole-mantle convection and the transition-zone water filter", Nature 425, 6953, 39 (2003).

Berry, A. J., L. V. Danyushevsky, H. S. C. O'Neill, M. Newville and S. R. Sutton, "Oxidation state of iron in komatiitic melt inclusions indicates hot archaean mantle", Nature 455, 7215, 960–963 (2008).

Billen, M. I., "Slab dynamics in the transition zone", Physics of the Earth and Planetary Interiors 183, 1-2, 296–308 (2010).

Bond, J. C., D. P. O'Brien and D. S. Lauretta, "The compositional diversity of extrasolar terrestrial planets. i. in situ simulations", The Astrophysical Journal 715, 2, 1050 (2010).

Bower, D. J., J. K. Wicks, M. Gurnis and J. M. Jackson, "A geodynamic and mineral physics model of a solid-state ultralow-velocity zone", Earth and Planetary Science Letters 303, 3-4, 193–202 (2011).

Brandenburg, J. and P. Van Keken, "Deep storage of oceanic crust in a vigorously convecting mantle", Journal of Geophysical Research: Solid Earth 112, B6 (2007).

Brodholt, J. P., G. Helffrich and J. Trampert, "Chemical versus thermal heterogeneity in the lower mantle: The most likely role of anelasticity", Earth and Planetary Science Letters 262, 3-4, 429–437 (2007).

Brown, J. and T. Shankland, "Thermodynamic parameters in the earth as determined from seismic profiles", Geophysical Journal International 66, 3, 579–596 (1981).

Brown, S. P., M. S. Thorne, L. Miyagi and S. Rost, "A compositional origin to ultralow-velocity zones", Geophysical Research Letters 42, 4, 1039–1045 (2015).

Buffett, B. A., E. J. Garnero and R. Jeanloz, "Sediments at the top of earth's core", Science 290, 5495, 1338–1342 (2000).

Bull, A. L., A. K. McNamara and J. Ritsema, "Synthetic tomography of plume clusters and thermochemical piles", Earth and Planetary Science Letters 278, 3, 152–162 (2009).

Burke, K., B. Steinberger, T. H. Torsvik and M. A. Smethurst, "Plume generation zones at the margins of large low shear velocity provinces on the core–mantle boundary", Earth and Planetary Science Letters 265, 1-2, 49–60 (2008).

Capitanio, F., G. Morra, S. Goes, R. Weinberg and L. Moresi, "India–asia convergence driven by the subduction of the greater indian continent", Nature Geoscience 3, 2, 136–139 (2010).

Carlson, R. W., E. Garnero, T. M. Harrison, J. Li, M. Manga, W. F. McDonough, S. Mukhopadhyay, B. Romanowicz, D. Rubie, Q. Williams *et al.*, "How did early earth become our modern world?", Annual Review of Earth and Planetary Sciences 42, 151–178 (2014).

Catalli, K., S.-H. Shim and V. Prakapenka, "Thickness and clapeyron slope of the post-perovskite boundary", Nature 462, 7274, 782 (2009).

Catalli, K., S.-H. Shim, V. B. Prakapenka, J. Zhao, W. Sturhahn, P. Chow, Y. Xiao, H. Liu, H. Cynn and W. J. Evans, "Spin state of ferric iron in mgsio3 perovskite and its effect on elastic properties", Earth and Planetary Science Letters 289, 1-2, 68–75 (2010).

Chen, H., S.-H. Shim, K. Leinenweber, V. Prakapenka, Y. Meng and C. Prescher, "Crystal structure of casio3 perovskite at 28–62 gpa and 300 k under quasi-hydrostatic stress conditions", American Mineralogist 103, 3, 462–468 (2018).

Christensen, U. R., "The influence of trench migration on slab penetration into the lower mantle", Earth and Planetary Science Letters 140, 1-4, 27–39 (1996).

Christensen, U. R., "Influence of chemical buoyancy on the dynamics of slabs in the transition zone", Journal of Geophysical Research: Solid Earth 102, B10, 22435–22443, URL `http://dx.doi.org/10.1029/97JB01342` (1997).

Christensen, U. R. and A. W. Hofmann, "Segregation of subducted oceanic crust in the convecting mantle", Journal of Geophysical Research: Solid Earth 99, B10, 19867–19884 (1994).

Condie, K. C. and A. Kröner, "When did plate tectonics begin? evidence from the geologic record", Geological society of America special papers 440, 281–294 (2008).

Connolly, J., "The geodynamic equation of state: what and how", Geochemistry, Geophysics, Geosystems 10, 10 (2009).

Cooper, K. M., J. M. Eiler, K. W. Sims and C. H. Langmuir, "Distribution of recycled crust within the upper mantle: Insights from the oxygen isotope composition of morb from the australian-antarctic discordance", Geochemistry, Geophysics, Geosystems 10, 12 (2009).

Corgne, A., N. L. Allan and B. J. Wood, "Atomistic simulations of trace element incorporation into the large site of mgsio3 and casio3 perovskites", Physics of the Earth and Planetary Interiors 139, 1-2, 113–127 (2003).

Davies, D., S. Goes and H. Lau, "Thermally dominated deep mantle llsvps: a review", in "The earth's heterogeneous mantle", pp. 441–477 (Springer, 2015).

Davies, D. R., S. Goes, J. H. Davies, B. Schuberth, H.-P. Bunge and J. Ritsema, "Reconciling dynamic and seismic models of earth's lower mantle: The dominant role of thermal heterogeneity", Earth and Planetary Science Letters 353, 253–269 (2012).

Davies, G. F., "On the emergence of plate tectonics", Geology 20, 11, 963–966 (1992).

Davies, G. F., "Episodic layering of the early mantle by the "basalt barrier" mechanism", Earth and Planetary Science Letters 275, 3-4, 382–392, URL `http://dx.doi.org/10.1016/j.epsl.2008.08.036` (2008).

De Wit, M. and L. Ashwal, "Preface: convergence towards divergent models of greenstone belts", in "Greenstone belts", pp. ix–xvii (Clarendon Press Oxford, 1997).

Deng, J. and K. K. Lee, "Viscosity jump in the lower mantle inferred from melting curves of ferropericlase", Nature communications 8, 1, 1–8 (2017).

Deschamps, F., L. Cobden and P. J. Tackley, "The primitive nature of large low shear-wave velocity provinces", Earth and Planetary Science Letters 349, 198–208 (2012).

Dorfman, S. M., Y. Meng, V. B. Prakapenka and T. S. Duffy, "Effects of fe-enrichment on the equation of state and stability of (mg, fe) sio3 perovskite", Earth and Planetary Science Letters 361, 249–257 (2013).

Dorfman, S. M., S. R. Shieh, Y. Meng, V. B. Prakapenka and T. S. Duffy, "Synthesis and equation of state of perovskites in the (mg, fe) 3al2si3o12 system to 177 gpa", Earth and Planetary Science Letters 357, 194–202 (2012).

Dorn, C., A. Khan, K. Heng, J. A. Connolly, Y. Alibert, W. Benz and P. Tackley, "Can we constrain the interior structure of rocky exoplanets from mass and radius measurements?", Astronomy & Astrophysics 577, A83 (2015).

Dorogokupets, P. and A. Dewaele, "Equations of state of mgo, au, pt, nacl-b1, and nacl-b2: Internally consistent high-temperature pressure scales", High Pressure Research 27, 4, 431–446 (2007).

Dubrovinsky, L., N. Dubrovinskaia, F. Langenhorst, D. Dobson, D. Rubie, C. Gessmann, I. Abrikosov, B. Johansson, V. Baykov, L. Vitos *et al.*, "Iron–silica interaction at extreme conditions and the electrically conducting layer at the base of earth's mantle", Nature 422, 6927, 58–61 (2003).

Duffy, T. S. and D. L. Anderson, "Seismic velocities in mantle minerals and the mineralogy of the upper mantle", Journal of Geophysical Research: Solid Earth 94, B2, 1895–1912 (1989).

Dziewonski, A. M. and D. L. Anderson, "Preliminary reference earth model", Physics of the earth and planetary interiors 25, 4, 297–356 (1981).

Dziewonski, A. M., V. Lekic and B. A. Romanowicz, "Mantle anchor structure: an argument for bottom up tectonics", Earth and Planetary Science Letters 299, 1, 69–79 (2010).

Fei, H., D. Yamazaki, M. Sakurai, N. Miyajima, H. Ohfuji, T. Katsura and T. Yamamoto, "A nearly water-saturated mantle transition zone inferred from mineral viscosity", Science advances 3, 6, e1603024 (2017).

Fei, Y., L. Zhang, A. Corgne, H. Watson, A. Ricolleau, Y. Meng and V. Prakapenka, "Spin transition and equations of state of (mg, fe) o solid solutions", Geophysical Research Letters 34, 17 (2007).

Finkelstein, G. J., J. M. Jackson, W. Sturhahn, D. Zhang, E. E. Alp and T. S. Toellner, "Single-crystal equations of state of magnesiowüstite at high pressures", American Mineralogist: Journal of Earth and Planetary Materials 102, 8, 1709–1717 (2017).

Fischer, R. A., A. J. Campbell, B. A. Chidester, D. M. Reaman, E. C. Thompson, J. S. Pigott, V. B. Prakapenka and J. S. Smith, "Equations of state and phase boundary for stishovite and cacl2-type sio2", American Mineralogist 103, 5, 792–802 (2018).

Foley, S. F., S. Buhre and D. E. Jacob, "Evolution of the archaean crust by delamination and shallow subduction", Nature 421, 6920, 249 (2003).

Forte, A. M. and J. X. Mitrovica, "Deep-mantle high-viscosity flow and thermochemical structure inferred from seismic and geodynamic data", Nature 410, 6832, 1049–1056 (2001).

Frost, D. A. and S. Rost, "The p-wave boundary of the large-low shear velocity province beneath the pacific", Earth and Planetary Science Letters 403, 380–392 (2014).

Frost, D. A., S. Rost, E. J. Garnero and M. Li, "Seismic evidence for earth's crusty deep mantle", Earth and Planetary Science Letters 470, 54–63 (2017).

Frost, D. J., C. Liebske, F. Langenhorst, C. A. McCammon, R. G. Trønnes and D. C. Rubie, "Experimental evidence for the existence of iron-rich metal in the earth's lower mantle", Nature 428, 6981, 409 (2004).

Fujino, K., D. Nishio-Hamane, Y. Seto, N. Sata, T. Nagai, T. Shinmei, T. Irifune, H. Ishii, N. Hiraoka, Y. Q. Cai *et al.*, "Spin transition of ferric iron in al-bearing mg–perovskite up to 200gpa and its implication for the lower mantle", Earth and Planetary Science Letters 317, 407–412 (2012).

Fukao, Y. and M. Obayashi, "Subducted slabs stagnant above, penetrating through, and trapped below the 660 km discontinuity", Journal of Geophysical Research: Solid Earth 118, 11, 5920–5938 (2013).

Fukao, Y., M. Obayashi, T. Nakakuki and D. S. P. Group, "Stagnant slab: a review", Annual Review of Earth and Planetary Sciences 37, 19–46 (2009).

Funamori, N., R. Jeanloz, N. Miyajima and K. Fujino, "Mineral assemblages of basalt in the lower mantle", Journal of Geophysical Research: Solid Earth 105, B11, 26037–26043 (2000).

Gale, A., C. A. Dalton, C. H. Langmuir, Y. Su and J.-G. Schilling, "The mean composition of ocean ridge basalts", Geochemistry, Geophysics, Geosystems 14, 3, 489–518 (2013).

Garnero, E. J. and D. V. Helmberger, "Seismic detection of a thin laterally varying boundary layer at the base of the mantle beneath the central-pacific", Geophysical Research Letters 23, 9, 977–980 (1996).

Garnero, E. J. and A. K. McNamara, "Structure and dynamics of earth9s lower mantle", science 320, 5876, 626–628 (2008).

Garnero, E. J., A. K. McNamara and S.-H. Shim, "Continent-sized anomalous zones with low seismic velocity at the base of earth's mantle", Nature Geoscience 9, 7, 481 (2016).

Garnero, E. J., J. Revenaugh, Q. Williams, T. Lay and L. H. Kellogg, "Ultralow velocity zone at the core-mantle boundary", The core-mantle boundary region 28, 319–334 (1998).

Gautron, L., S. Greaux, D. Andrault, N. Bolfan-Casanova, N. Guignot and M. A. Bouhifd, "Uranium in the earth's lower mantle", Geophysical Research Letters 33, 23 (2006).

Girard, J., G. Amulele, R. Farla, A. Mohiuddin and S.-i. Karato, "Shear deformation of bridgmanite and magnesiowüstite aggregates at lower mantle conditions", Science p. aad3113 (2015).

Goes, S., R. Agrusta, J. van Hunen and F. Garel, "Subduction-transition zone interaction: A review", Geosphere 13, 3, 644–664 (2017).

Grand, S. P., "Mantle shear–wave tomography and the fate of subducted slabs", Philosophical Transactions of the Royal Society of London. Series A: Mathematical, Physical and Engineering Sciences 360, 1800, 2475–2491 (2002).

Gréaux, S., F. Farges, L. Gautron, N. Trcera, A.-M. Flank and P. Lagarde, "X-ray absorption near edge structure (xanes) study of the speciation of uranium and thorium in al-rich casio3 perovskite", American Mineralogist 97, 1, 100–109 (2012).

Gréaux, S., L. Gautron, D. Andrault, N. Bolfan-Casanova, N. Guignot and M. A. Bouhifd, "Experimental high pressure and high temperature study of the incorporation of uranium in al-rich casio3 perovskite", Physics of the Earth and Planetary Interiors 174, 1-4, 254–263 (2009).

Greaux, S., T. Irifune, Y. Higo, Y. Tange, T. Arimoto, Z. Liu and A. Yamada, "Sound velocity of casio 3 perovskite suggests the presence of basaltic crust in the earth's lower mantle", Nature 565, 7738, 218–221 (2019).

Grove, T. and S. Parman, "Thermal evolution of the earth as recorded by komatiites", Earth and Planetary Science Letters 219, 3-4, 173–187 (2004).

Gu, T., M. Li, C. McCammon and K. K. Lee, "Redox-induced lower mantle density contrast and effect on mantle structure and primitive oxygen", Nature Geoscience 9, 9, 723–727 (2016).

Handy, M. R., "Flow laws for rocks containing two non-linear viscous phases: a phenomenological approach", Journal of Structural Geology 16, 3, 287–302 (1994).

Haugland, S. M., J. Ritsema, S. Kaneshima and M. S. Thorne, "Estimate of the rigidity of eclogite in the lower mantle from waveform modeling of broadband s-to-p wave conversions", Geophysical Research Letters 44, 23, 11–778 (2017).

He, Y. and L. Wen, "Structural features and shear-velocity structure of the "pacific anomaly"", Journal of Geophysical Research: Solid Earth 114, B2 (2009).

Herzberg, C., P. D. Asimow, N. Arndt, Y. Niu, C. Lesher, J. Fitton, M. Cheadle and A. Saunders, "Temperatures in ambient mantle and plumes: Constraints from basalts, picrites, and komatiites", Geochemistry, Geophysics, Geosystems 8, 2 (2007).

Herzberg, C., K. Condie and J. Korenaga, "Thermal history of the earth and its petrological expression", Earth and Planetary Science Letters 292, 1-2, 79–88 (2010).

Herzberg, C. and R. Rudnick, "Formation of cratonic lithosphere: An integrated thermal and petrological model", Lithos 149, 4–15 (2012).

Hinkel, N. R., F. Timmes, P. A. Young, M. D. Pagano and M. C. Turnbull, "Stellar abundances in the solar neighborhood: the hypatia catalog", The Astronomical Journal 148, 3, 54 (2014).

Hirose, K., "Phase transitions in pyrolitic mantle around 670-km depth: Implications for upwelling of plumes from the lower mantle", Journal of Geophysical Research: Solid Earth 107, B4 (2002).

Hirose, K. and Y. Fei, "Subsolidus and melting phase relations of basaltic composition in the uppermostlower mantle", Geochimica et Cosmochimica Acta 66, 12, 2099–2108 (2002).

Hirose, K., Y. Fei, Y. Ma and H.-K. Mao, "The fate of subducted basaltic crust in the earth's lower mantle", Nature 397, 6714, 53 (1999).

Hirose, K., N. Takafuji, N. Sata and Y. Ohishi, "Phase transition and density of subducted morb crust in the lower mantle", Earth and Planetary Science Letters 237, 1, 239–251 (2005).

Hirth, G. and D. Kohlstedf, "Rheology of the upper mantle and the mantle wedge: A view from the experimentalists", GEOPHYSICAL MONOGRAPH-AMERICAN GEOPHYSICAL UNION 138, 83–106 (2003).

Holland, T. and S. Redfern, "Unitcell: a nonlinear least-squares program for cell-parameter refinement and implementing regression and deletion diagnostics", Journal of Applied Crystallography 30, 1, 84–84 (1997).

Holzapfel, C., D. C. Rubie, D. J. Frost and F. Langenhorst, "Fe-mg interdiffusion in (mg, fe) sio3 perovskite and lower mantle reequilibration", Science 309, 5741, 1707–1710 (2005).

Hsu, H., P. Blaha, M. Cococcioni and R. M. Wentzcovitch, "Spin-state crossover and hyperfine interactions of ferric iron in mgsio 3 perovskite", Physical Review Letters 106, 11, 118501 (2011).

Huang, C., W. Leng and Z. Wu, "The continually stable subduction, iron-spin transition and the formation of llsvps from subducted oceanic crust", Journal of Geophysical Research: Solid Earth p. e2019JB018262 (2020).

Huang, X., Y. Xu and S.-i. Karato, "Water content in the transition zone from electrical conductivity of wadsleyite and ringwoodite", Nature 434, 7034, 746–749 (2005).

Idehara, K., "Structural heterogeneity of an ultra-low-velocity zone beneath the philippine islands: Implications for core–mantle chemical interactions induced by massive partial melting at the bottom of the mantle", Physics of the Earth and Planetary Interiors 184, 1-2, 80–90 (2011).

Irifune, T., T. Koizumi and J.-i. Ando, "An experimental study of the garnet-perovskite transformation in the system mgsio3-mg3al2si3o12", Physics of the Earth and Planetary Interiors 96, 2-3, 147–157 (1996).

Irifune, T., M. Miyashita, T. Inoue, J. Ando, K. Funakoshi and W. Utsumi, "High-pressure phase transformation in camgsi2o6 and implications for origin of ultra-deep diamond inclusions", Geophysical Research Letters 27, 21, 3541–3544 (2000).

Irifune, T. and A. Ringwood, "Phase transformations in a harzburgite composition to 26 gpa: implications for dynamical behaviour of the subducting slab", Earth and Planetary Science Letters 86, 2-4, 365–376 (1987a).

Irifune, T. and A. Ringwood, "Phase transformations in primitive morb and pyrolite compositions to 25 gpa and some geophysical implications", High pressure research in mineral physics 39, 235–246 (1987b).

Irifune, T. and A. Ringwood, "Phase transformations in subducted oceanic crust and buoyancy relationships at depths of 600–800 km in the mantle", Earth and Planetary Science Letters 117, 1-2, 101–110 (1993).

Irifune, T., A. Ringwood and W. Hibberson, "Subduction of continental crust and terrigenous and pelagic sediments: an experimental study", Earth and Planetary Science Letters 126, 4, 351–368 (1994).

Irifune, T., T. Sekine, A. Ringwood and W. Hibberson, "The eclogite-garnetite transformation at high pressure and some geophysical implications", Earth and Planetary Science Letters 77, 2, 245–256 (1986).

Irifune, T., T. Shinmei, C. A. McCammon, N. Miyajima, D. C. Rubie and D. J. Frost, "Iron partitioning and density changes of pyrolite in earth's lower mantle", Science 327, 5962, 193–195 (2010).

Ishii, M. and J. Tromp, "Normal-mode and free-air gravity constraints on lateral variations in velocity and density of earth's mantle", Science 285, 5431, 1231–1236 (1999).

Ishii, T., R. Huang, H. Fei, I. Koemets, Z. Liu, F. Maeda, L. Yuan, L. Wang, D. Druzhbin, T. Yamamoto *et al.*, "Complete agreement of the post-spinel transition with the 660-km seismic discontinuity", Scientific reports 8, 1, 6358 (2018).

Ishii, T., H. Kojitani and M. Akaogi, "Post-spinel transitions in pyrolite and mg2sio4 and akimotoite–perovskite transition in mgsio3: precise comparison by high-pressure high-temperature experiments with multi-sample cell technique", Earth and Planetary Science Letters 309, 3-4, 185–197 (2011).

Ito, E. and E. Takahashi, "Postspinel transformations in the system mg2sio4-fe2sio4 and some geophysical implications", Journal of Geophysical Research: Solid Earth 94, B8, 10637–10646 (1989).

Ito, Y. and M. Toriumi, "Silicon self-diffusion of mgsio3 perovskite by molecular dynamics and its implication for lower mantle rheology", Journal of Geophysical Research: Solid Earth 115, B12 (2010).

Johnson, T. E., M. Brown, B. J. Kaus and J. A. VanTongeren, "Delamination and recycling of archaean crust caused by gravitational instabilities", Nature Geoscience 7, 1, 47 (2014).

Kaneshima, S., "Seismic scatterers in the mid-lower mantle", Physics of the Earth and Planetary Interiors 257, 105–114 (2016).

Karato, S.-i., "Pressure dependence of diffusion in ionic solids", Physics of the Earth and Planetary Interiors 25, 1, 38–51 (1981).

Karato, S.-i., "Rheology of the earth's mantle: A historical review", Gondwana Research 18, 1, 17–45 (2010).

Karato, S.-i., *Deformation of earth materials: an introduction to the rheology of solid earth* (Cambridge University Press, 2012).

Karato, S.-i. and B. B. Karki, "Origin of lateral variation of seismic wave velocities and density in the deep mantle", Journal of Geophysical Research: Solid Earth 106, B10, 21771–21783 (2001).

Karato, S.-i. and P. Wu, "Rheology of the upper mantle: A synthesis", Science 260, 5109, 771–778 (1993).

Karki, B. B., L. Stixrude and J. Crain, "Ab initio elasticity of three high-pressure polymorphs of silica", Geophysical Research Letters 24, 24, 3269–3272 (1997).

Kasting, J. F., "What caused the rise of atmospheric o2?", Chemical Geology 362, 13–25 (2013).

Katsura, T., H. Yamada, T. Shinmei, A. Kubo, S. Ono, M. Kanzaki, A. Yoneda, M. J. Walter, E. Ito, S. Urakawa *et al.*, "Post-spinel transition in mg2sio4 determined by high p–t in situ x-ray diffractometry", Physics of the Earth and Planetary Interiors 136, 1-2, 11–24 (2003).

Katsura, T., A. Yoneda, D. Yamazaki, T. Yoshino and E. Ito, "Adiabatic temperature profile in the mantle", Physics of the Earth and Planetary Interiors 183, 1-2, 212–218 (2010).

Kearey, P., K. A. Klepeis and F. J. Vine, *Global tectonics* (John Wiley & Sons, 2009).

Kesson, S., J. F. Gerald and J. Shelley, "Mineralogy and dynamics of a pyrolite lower mantle", Nature 393, 6682, 252–255 (1998).

King, S. D., D. J. Frost and D. C. Rubie, "Why cold slabs stagnate in the transition zone", Geology 43, 3, 231–234 (2015).

Klein, B. Z., O. Jagoutz and M. D. Behn, "Archean crustal compositions promote full mantle convection", Earth and Planetary Science Letters 474, 516–526, URL `http://dx.doi.org/10.1016/j.epsl.2017.07.003` (2017).

Koelemeijer, P., A. Deuss and J. Ritsema, "Density structure of earth's lowermost mantle from stoneley mode splitting observations", Nature Communications 8, 1, 1–10 (2017).

Korenaga, J., "Urey ratio and the structure and evolution of earth's mantle", Reviews of Geophysics 46, 2 (2008).

Korenaga, J., "Scaling of stagnant-lid convection with arrhenius rheology and the effects of mantle melting", Geophysical Journal International 179, 1, 154–170 (2009).

Korenaga, J., "Scaling of plate tectonic convection with pseudoplastic rheology", Journal of Geophysical Research: Solid Earth 115, B11 (2010).

Korenaga, J., "Crustal evolution and mantle dynamics through earth history", Philosophical Transactions of the Royal Society A: Mathematical, Physical and Engineering Sciences 376, 2132, 20170408 (2018).

Kubo, A. and M. Akaogi, "Post-garnet transitions in the system mg4si4o12–mg3al2si3o12 up to 28 gpa: phase relations of garnet, ilmenite and perovskite", Physics of the Earth and Planetary Interiors 121, 1-2, 85–102 (2000).

Kubo, A., E. Ito, T. Katsura, K. Fujino and K.-I. Funakoshi, "In situ x-ray diffraction of pyrolite to 40 gpa using kawai-type apparatus with sintered diamond anvils: possibility for the existence of iron-rich metallic particles in the lower mantle", High Pressure Research 28, 3, 351–362 (2008).

Kubo, T., E. Ohtani, T. Kato, S. Urakawa, A. Suzuki, Y. Kanbe, K.-i. Funakoshi, W. Utsumi and K. Fujino, "Formation of metastable assemblages and mechanisms of the grain-size reduction in the postspinel transformation of mg2sio4", Geophysical Research Letters 27, 6, 807–810 (2000).

Labrosse, S., J. Hernlund and N. Coltice, "A crystallizing dense magma ocean at the base of the earth's mantle", Nature 450, 7171, 866–869 (2007).

Laurent, O., H. Martin, J.-F. Moyen and R. Doucelance, "The diversity and evolution of late-archean granitoids: Evidence for the onset of "modern-style" plate tectonics between 3.0 and 2.5 ga", Lithos 205, 208–235 (2014).

Lee, C.-T. A., P. Luffi, T. Höink, J. Li, R. Dasgupta and J. Hernlund, "Upside-down differentiation and generation of a'primordial'lower mantle", Nature 463, 7283, 930 (2010).

Lee, K. K., B. O'Neill, W. R. Panero, S.-H. Shim, L. R. Benedetti and R. Jeanloz, "Equations of state of the high-pressure phases of a natural peridotite and implications for the earth's lower mantle", Earth and Planetary Science Letters 223, 3-4, 381–393 (2004).

Letoullec, R., J. Pinceaux and P. Loubeyre, "The membrane diamond anvil cell: a new device for generating continuous pressure and temperature variations", International Journal of High Pressure Research 1, 1, 77–90 (1988).

Li, B., C. Ji, W. Yang, J. Wang, K. Yang, R. Xu, W. Liu, Z. Cai, J. Chen and H.-k. Mao, "Diamond anvil cell behavior up to 4 mbar", Proceedings of the National Academy of Sciences 115, 8, 1713–1717 (2018).

Li, M. and A. K. McNamara, "The difficulty for subducted oceanic crust to accumulate at the earth's core-mantle boundary", Journal of Geophysical Research: Solid Earth 118, 4, 1807–1816 (2013).

Li, M. and A. K. McNamara, "The influence of deep mantle compositional heterogeneity on earth's thermal evolution", Earth and Planetary Science Letters 500, 86–96 (2018).

Litasov, K., E. Ohtani, A. Sano, A. Suzuki and K. Funakoshi, "In situ x-ray diffraction study of post-spinel transformation in a peridotite mantle: implication for the 660-km discontinuity", Earth and Planetary Science Letters 238, 3, 311–328 (2005).

Litasov, K., E. Ohtani, A. Suzuki, T. Kawazoe and K. Funakoshi, "Absence of density crossover between basalt and peridotite in the cold slabs passing through 660 km discontinuity", Geophysical Research Letters 31, 24 (2004).

Litasov, K. D. and E. Ohtani, "Phase relations in hydrous morb at 18–28gpa: implications for heterogeneity of the lower mantle", Physics of the Earth and Planetary Interiors 150, 4, 239–263, URL `http://dx.doi.org/10.1016/j.pepi.2004.10.010` (2005).

Liu, J., J. Li, R. Hrubiak and J. S. Smith, "Origins of ultralow velocity zones through slab-derived metallic melt", Proceedings of the National Academy of Sciences 113, 20, 5547–5551 (2016).

Liu, L.-g., "New silicate perovskites", Geophysical Research Letters 14, 11, 1079–1082 (1987).

Liu, Z., M. Nishi, T. Ishii, H. Fei, N. Miyajima, T. B. Ballaran, H. Ohfuji, T. Sakai, L. Wang, S. Shcheka *et al.*, "Phase relations in the system mgsio3-al2o3 up to 2300 k at lower mantle pressures", Journal of Geophysical Research: Solid Earth 122, 10, 7775–7788 (2017).

Lundin, S., K. Catalli, J. Santillan, S.-H. Shim, V. Prakapenka, M. Kunz and Y. Meng, "Effect of fe on the equation of state of mantle silicate perovskite over 1 mbar", Physics of the Earth and Planetary Interiors 168, 1-2, 97–102 (2008).

Mao, W. and S. Zhong, "Slab stagnation due to a reduced viscosity layer beneath the mantle transition zone", Nature Geoscience 11, 11, 876 (2018).

Marquardt, H. and L. Miyagi, "Slab stagnation in the shallow lower mantle linked to an increase in mantle viscosity", Nature Geoscience 8, 4, 311 (2015).

Masters, G. and D. Gubbins, "On the resolution of density within the earth", Physics of the Earth and Planetary Interiors 140, 1-3, 159–167 (2003).

Masters, G., G. Laske, H. Bolton and A. Dziewonski, "The relative behavior of shear velocity, bulk sound speed, and compressional velocity in the mantle: Implications for chemical and thermal structure", Earth's deep interior: mineral physics and tomography from the atomic to the global scale 117, 63–87 (2000).

McCammon, C., "Perovskite as a possible sink for ferric iron in the lower mantle", Nature 387, 6634, 694 (1997).

McDonough, W. F. and S.-S. Sun, "The composition of the earth", Chemical geology 120, 3-4, 223–253 (1995).

McNamara, A. K. and S. Zhong, "Thermochemical structures beneath africa and the pacific ocean", Nature 437, 7062, 1136 (2005).

Mulyukova, E., B. Steinberger, M. Dabrowski and S. V. Sobolev, "Survival of llsvps for billions of years in a vigorously convecting mantle: replenishment and destruction of chemical anomaly", Journal of Geophysical Research: Solid Earth 120, 5, 3824–3847 (2015).

Murakami, M., K. Hirose, S. Ono and Y. Ohishi, "Stability of cacl2-type and α-pbo2-type sio2 at high pressure and temperature determined by in-situ x-ray measurements", Geophysical Research Letters 30, 5 (2003).

Nakagawa, T., P. J. Tackley, F. Deschamps and J. A. Connolly, "Incorporating self-consistently calculated mineral physics into thermochemical mantle convection simulations in a 3-d spherical shell and its influence on seismic anomalies in earth's mantle", Geochemistry, Geophysics, Geosystems 10, 3 (2009).

Nakagawa, T., P. J. Tackley, F. Deschamps and J. A. Connolly, "The influence of morb and harzburgite composition on thermo-chemical mantle convection in a 3-d spherical shell with self-consistently calculated mineral physics", Earth and Planetary Science Letters 296, 3-4, 403–412, URL http://dx.doi.org/10.1016/j.epsl.2010.05.026 (2010).

Newville, M., T. Stensitzki, D. B. Allen, M. Rawlik, A. Ingargiola and A. Nelson, "Lmfit: Non-linear least-square minimization and curve-fitting for python", Astrophysics Source Code Library (2016).

Nicklas, R. W., I. S. Puchtel, R. D. Ash, P. M. Piccoli, E. Hanski, E. G. Nisbet, P. Waterton, D. G. Pearson and A. D. Anbar, "Secular mantle oxidation across the archean-proterozoic boundary: Evidence from v partitioning in komatiites and picrites", Geochimica et Cosmochimica Acta (2019).

Nisbet, E., M. Cheadle, N. Arndt and M. Bickle, "Constraining the potential temperature of the archaean mantle: a review of the evidence from komatiites", Lithos 30, 3-4, 291–307 (1993).

Nishi, M., T. Kubo, H. Ohfuji, T. Kato, Y. Nishihara and T. Irifune, "Slow si–al interdiffusion in garnet and stagnation of subducting slabs", Earth and Planetary Science Letters 361, 44–49 (2013).

Nishihara, Y. and E. Takahashi, "Phase relation and physical properties of an al-depleted komatiite to 23 gpa", Earth and Planetary Science Letters 190, 1-2, 65–77 (2001).

Nishiyama, N., T. Irifune, T. Inoue, J.-i. Ando and K.-i. Funakoshi, "Precise determination of phase relations in pyrolite across the 660 km seismic discontinuity by in situ x-ray diffraction and quench experiments", Physics of the Earth and Planetary Interiors 143, 185–199 (2004).

Nishiyama, N. and T. Yagi, "Phase relation and mineral chemistry in pyrolite to 2200 c under the lower mantle pressures and implications for dynamics of mantle plumes", Journal of Geophysical Research: Solid Earth 108, B5 (2003).

Nomura, R., K. Hirose, N. Sata and Y. Ohishi, "Precise determination of post-stishovite phase transition boundary and implications for seismic heterogeneities in the mid-lower mantle", Physics of the Earth and Planetary Interiors 183, 1-2, 104–109 (2010).

Nomura, R., K. Hirose, K. Uesugi, Y. Ohishi, A. Tsuchiyama, A. Miyake and Y. Ueno, "Low core-mantle boundary temperature inferred from the solidus of pyrolite", Science 343, 6170, 522–525 (2014).

Obayashi, M., J. Yoshimitsu, G. Nolet, Y. Fukao, H. Shiobara, H. Sugioka, H. Miyamachi and Y. Gao, "Finite frequency whole mantle p wave tomography: Improvement of subducted slab images", Geophysical Research Letters 40, 21, 5652–5657 (2013).

Ogawa, M., "Chemical stratification in a two-dimensional convecting mantle with magmatism and moving plates", Journal of Geophysical Research 108, B12, URL http://dx.doi.org/10.1029/2002JB002205 (2003).

Oguri, K., N. Funamori, T. Uchida, N. Miyajima, T. Yagi and K. Fujino, "Post-garnet transition in a natural pyrope: a multi-anvil study based on in situ x-ray diffraction and transmission electron microscopy", Physics of the Earth and Planetary Interiors 122, 3-4, 175–186 (2000).

Ohta, K., K. Hirose, T. Lay, N. Sata and Y. Ohishi, "Phase transitions in pyrolite and morb at lowermost mantle conditions: implications for a morb-rich pile above the core–mantle boundary", Earth and Planetary Science Letters 267, 1-2, 107–117 (2008).

O'keeffe, M., B. Hyde and J.-O. Bovin, "Contribution to the crystal chemistry of orthorhombic perovskites: Mgsio 3 and namgf 3", Physics and Chemistry of Minerals 4, 4, 299–305 (1979).

Ono, S., Y. Ohishi, M. Isshiki and T. Watanuki, "In situ x-ray observations of phase assemblages in peridotite and basalt compositions at lower mantle conditions: Implications for density of subducted oceanic plate", Journal of Geophysical Research: Solid Earth 110, B2 (2005).

Ono, S., Y. Ohishi and K. Mibe, "Phase transition of ca-perovskite and stability of al-bearing mg-perovskite in the lower mantle", American Mineralogist 89, 10, 1480–1485 (2004).

Palin, R. M. and R. W. White, "Emergence of blueschists on earth linked to secular changes in oceanic crust composition", Nature Geoscience 9, 1, 60 (2016).

Panasyuk, S. V. and B. H. Hager, "A model of transformational superplasticity in the upper mantle", Geophysical Journal International 133, 3, 741–755 (1998).

Parman, S., T. Grove and J. Dann, "The production of barberton komatiites in an archean subduction zone", Geophysical Research Letters 28, 13, 2513–2516 (2001).

Pearson, D., F. Brenker, F. Nestola, J. McNeill, L. Nasdala, M. Hutchison, S. Matveev, K. Mather, G. Silversmit, S. Schmitz *et al.*, "Hydrous mantle transition zone indicated by ringwoodite included within diamond", Nature 507, 7491, 221–224 (2014).

Perry, S. N., J. S. Pigott and W. R. Panero, "Ab initio calculations of uranium and thorium storage in casio3-perovskite in the earth's lower mantle", American Mineralogist 102, 2, 321–326 (2017).

Prakapenka, V., A. Kubo, A. Kuznetsov, A. Laskin, O. Shkurikhin, P. Dera, M. Rivers and S. Sutton, "Advanced flat top laser heating system for high pressure research at gsecars: application to the melting behavior of germanium", High Pressure Research 28, 3, 225–235 (2008).

Prescher, C. and V. B. Prakapenka, "Dioptas: a program for reduction of two-dimensional x-ray diffraction data and data exploration", High Pressure Research 35, 3, 223–230, URL http://dx.doi.org/10.1080/08957959.2015.1059835 (2015).

Ricolleau, A., Y. Fei, E. Cottrell, H. Watson, L. Deng, L. Zhang, G. Fiquet, A.-L. Auzende, M. Roskosz, G. Morard *et al.*, "Density profile of pyrolite under the lower mantle conditions", Geophysical Research Letters 36, 6 (2009).

Ricolleau, A., J.-p. Perrillat, G. Fiquet, I. Daniel, J. Matas, A. Addad, N. Menguy, H. Cardon, M. Mezouar and N. Guignot, "Phase relations and equation of state of a natural morb: Implications for the density profile of subducted oceanic crust in the earth's lower mantle", Journal of Geophysical Research: Solid Earth 115, B8 (2010).

Ringwood, A. E., "Phase transformations and differentiation in subducted lithosphere: implications for mantle dynamics, basalt petrogenesis, and crustal evolution", The Journal of Geology 90, 6, 611–643 (1982).

Ringwood, A. E. and T. Irifune, "Nature of the 650–km seismic discontinuity: implications for mantle dynamics and differentiation", Nature 331, 6152, 131 (1988).

Rivers, M., V. B. Prakapenka, A. Kubo, C. Pullins, C. M. Holl and S. D. Jacobsen, "The compres/gsecars gas-loading system for diamond anvil cells at the advanced photon source", High Pressure Research 28, 3, 273–292 (2008).

Ross, A., H. Thybo and L. Solidilov, "Reflection seismic profiles of the core-mantle boundary", Journal of Geophysical Research: Solid Earth 109, B8 (2004).

Rost, S., E. J. Garnero and W. Stefan, "Thin and intermittent ultralow-velocity zones", Journal of Geophysical Research: Solid Earth 115, B6 (2010).

Rudolph, M. L., V. Lekić and C. Lithgow-Bertelloni, "Viscosity jump in earth's mid-mantle", Science 350, 6266, 1349–1352 (2015).

Sanehira, T., T. Irifune, T. Shinmei, H. Ohfuji, F. Brunet and K.-I. Funakoshi, "Density profiles of pyrolite and morb compositions across the 660 km seismic discontinuity", High Pressure Research 28, 3, 335–349 (2008).

Sano, A., E. Ohtani, K. Litasov, T. Kubo, T. Hosoya, K. Funakoshi and T. Kikegawa, "In situ x-ray diffraction study of the effect of water on the garnet–perovskite transformation in morb and implications for the penetration of oceanic crust into the lower mantle", Physics of the Earth and Planetary Interiors 159, 1-2, 118–126 (2006).

Schellart, W. P. and L. Moresi, "A new driving mechanism for backarc extension and backarc shortening through slab sinking induced toroidal and poloidal mantle flow: Results from dynamic subduction models with an overriding plate", Journal of Geophysical Research: Solid Earth 118, 6, 3221–3248 (2013).

Schuberth, B. S., H.-P. Bunge and J. Ritsema, "Tomographic filtering of high-resolution mantle circulation models: Can seismic heterogeneity be explained by temperature alone?", Geochemistry, Geophysics, Geosystems 10, 5 (2009).

Schulz, K., "Magnesian basalts from the archaean terrains of minnesota", Komatiites. London, George Allen & Unwin pp. 171–186 (1982).

Schutt, D. and C. Lesher, "Effects of melt depletion on the density and seismic velocity of garnet and spinel lherzolite", Journal of Geophysical Research: Solid Earth 111, B5 (2006).

Shannon, R. D., "Revised effective ionic radii and systematic studies of interatomic distances in halides and chalcogenides", Acta crystallographica section A: crystal physics, diffraction, theoretical and general crystallography 32, 5, 751–767 (1976).

Sherby, O., J. Robbins and A. Goldberg, "Calculation of activation volumes for self-diffusion and creep at high temperature", Journal of Applied Physics 41, 10, 3961–3968 (1970).

Shim, S.-H., "Peakpo - a python software for x-ray diffraction analysis at high pressure and high temperature", URL `https://doi.org/10.5281/zenodo.842949` (2017a).

Shim, S.-H., "Pytheos - a python tool set for equations of state pytheos - a python tool set for equations of state", URL `https://doi.org/10.5281/zenodo.802392` (2017b).

Shim, S.-H., B. Grocholski, Y. Ye, E. E. Alp, S. Xu, D. Morgan, Y. Meng and V. B. Prakapenka, "Stability of ferrous-iron-rich bridgmanite under reducing midmantle conditions", Proceedings of the National Academy of Sciences 114, 25, 6468–6473 (2017).

Sinmyo, R. and K. Hirose, "The soret diffusion in laser-heated diamond-anvil cell", Physics of the Earth and Planetary Interiors 180, 3-4, 172–178 (2010).

Sinmyo, R. and K. Hirose, "Iron partitioning in pyrolitic lower mantle", Physics and Chemistry of Minerals 40, 2, 107–113 (2013).

Sinmyo, R., K. Hirose, S. Muto, Y. Ohishi and A. Yasuhara, "The valence state and partitioning of iron in the earth's lowermost mantle", Journal of Geophysical Research: Solid Earth 116, B7 (2011).

Sinmyo, R., H. Ozawa, K. Hirose, A. Yasuhara, N. Endo, N. Sata and Y. Ohishi, "Ferric iron content in (mg, fe) sio3 perovskite and post-perovskite at deep lower mantle conditions", American Mineralogist 93, 11-12, 1899–1902 (2008).

Sizova, E., T. Gerya, M. Brown and L. Perchuk, "Subduction styles in the precambrian: Insight from numerical experiments", Lithos 116, 3-4, 209–229 (2010).

Spence, D., J. Ockendon, P. Wilmott, D. Turcotte and L. Kellogg, "Convective mixing in the mantle: the role of viscosity differences", Geophysical Journal International 95, 1, 79–86 (1988).

Speziale, S., V. Lee, S. Clark, J. Lin, M. Pasternak and R. Jeanloz, "Effects of fe spin transition on the elasticity of (mg, fe) o magnesiowüstites and implications for the seismological properties of the earth's lower mantle", Journal of Geophysical Research: Solid Earth 112, B10 (2007).

Speziale, S., A. Milner, V. Lee, S. M. Clark, M. P. Pasternak and R. Jeanloz, "Iron spin transition in earth's mantle", Proceedings of the National Academy of Sciences 102, 50, 17918–17922 (2005).

Steinberger, B. and T. H. Torsvik, "A geodynamic model of plumes from the margins of large low shear velocity provinces", Geochemistry, Geophysics, Geosystems 13, 1 (2012).

Stixrude, L. and C. Lithgow-Bertelloni, "Thermodynamics of mantle minerals—i. physical properties", Geophysical Journal International 162, 2, 610–632 (2005).

Stixrude, L. and C. Lithgow-Bertelloni, "Thermodynamics of mantle minerals-ii. phase equilibria", Geophysical Journal International 184, 3, 1180–1213 (2011).

Stixrude, L. and C. Lithgow-Bertelloni, "Geophysics of chemical heterogeneity in the mantle", Annual Review of Earth and Planetary Sciences 40, 569–595 (2012).

Takeda, Y.-T., "Flow in rocks modelled as multiphase continua: Application to polymineralic rocks", Journal of Structural Geology 20, 11, 1569–1578 (1998).

Tan, E., W. Leng, S. Zhong and M. Gurnis, "On the location of plumes and lateral movement of thermochemical structures with high bulk modulus in the 3-d compressible mantle", Geochemistry, Geophysics, Geosystems 12, 7 (2011).

Tang, M., K. Chen and R. L. Rudnick, "Archean upper crust transition from mafic to felsic marks the onset of plate tectonics", Science 351, 6271, 372–375 (2016).

Tangeman, J. A., B. L. Phillips, A. Navrotsky, J. Weber, A. D. Hixson and T. S. Key, "Vitreous forsterite (mg2sio4): synthesis, structure, and thermochemistry", Geophysical research letters 28, 13, 2517–2520 (2001).

Tetzlaff, M. and H. Schmeling, "The influence of olivine metastability on deep subduction of oceanic lithosphere", Physics of the Earth and Planetary Interiors 120, 1-2, 29–38 (2000).

Thomas, C., J.-M. Kendall and G. Helffrich, "Probing two low-velocity regions with pkp b-caustic amplitudes and scattering", Geophysical Journal International 178, 1, 503–512 (2009).

Thomson, A., W. Crichton, J. Brodholt, I. Wood, N. Siersch, J. Muir, D. Dobson and S. Hunt, "Seismic velocities of casio 3 perovskite can explain llsvps in earth's lower mantle", Nature 572, 7771, 643–647 (2019).

Thorne, M. S., E. J. Garnero and S. P. Grand, "Geographic correlation between hot spots and deep mantle lateral shear-wave velocity gradients", Physics of the Earth and Planetary Interiors 146, 1, 47–63 (2004).

Toby, B. H. and R. B. Von Dreele, "Gsas-ii: the genesis of a modern open-source all purpose crystallography software package", Journal of Applied Crystallography 46, 2, 544–549 (2013).

Tolstikhin, I., J. D. Kramers and A. Hofmann, "A chemical earth model with whole mantle convection: the importance of a core–mantle boundary layer (d″) and its early formation", Chemical geology 226, 3-4, 79–99 (2006).

Torii, Y. and S. Yoshioka, "Physical conditions producing slab stagnation: Constraints of the clapeyron slope, mantle viscosity, trench retreat, and dip angles", Tectonophysics 445, 3-4, 200–209 (2007).

Torsvik, T. H., K. Burke, B. Steinberger, S. J. Webb and L. D. Ashwal, "Diamonds sampled by plumes from the core–mantle boundary", Nature 466, 7304, 352–355 (2010).

Trampert, J., F. Deschamps, J. Resovsky and D. Yuen, "Probabilistic tomography maps chemical heterogeneities throughout the lower mantle", Science 306, 5697, 853–856 (2004).

Tsuchiya, T., R. Caracas and J. Tsuchiya, "First principles determination of the phase boundaries of high-pressure polymorphs of silica", Geophysical Research Letters 31, 11 (2004a).

Tsuchiya, T., J. Tsuchiya, K. Umemoto and R. M. Wentzcovitch, "Elasticity of post-perovskite mgsio3", Geophysical Research Letters 31, 14 (2004b).

Unterborn, C. T., S. J. Desch, N. R. Hinkel and A. Lorenzo Jr, "Inward migration of the trappist-1 planets as inferred from their water-rich compositions", arXiv preprint arXiv:1706.02689 (2017).

Unterborn, C. T. and W. R. Panero, "The effects of mg/si on the exoplanetary refractory oxygen budget", The Astrophysical Journal 845, 1, 61 (2017).

van der Hilst, R. and T. Seno, "Effects of relative plate motion on the deep structure and penetration depth of slabs below the izu-bonin and mariana island arcs", Earth and Planetary Science Letters 120, 3-4, 395–407 (1993).

Van der Hilst, R. D., S. Widiyantoro and E. Engdahl, "Evidence for deep mantle circulation from global tomography", Nature 386, 6625, 578–584 (1997).

Van Hunen, J. and J.-F. Moyen, "Archean subduction: fact or fiction?", Annual Review of Earth and Planetary Sciences 40, 195–219 (2012).

van Hunen, J. and A. P. van den Berg, "Plate tectonics on the early earth: limitations imposed by strength and buoyancy of subducted lithosphere", Lithos 103, 1-2, 217–235 (2008).

Vance, S. D., M. P. Panning, S. Stähler, F. Cammarano, B. G. Bills, G. Tobie, S. Kamata, S. Kedar, C. Sotin, W. T. Pike *et al.*, "Geophysical investigations of habitability in ice-covered ocean worlds", Journal of Geophysical Research: Planets 123, 1, 180–205 (2018).

Vinet, P., J. R. Smith, J. Ferrante and J. H. Rose, "Temperature effects on the universal equation of state of solids", Physical Review B 35, 4, 1945 (1987).

Walter, M., A. Kubo, T. Yoshino, J. Brodholt, K. Koga and Y. Ohishi, "Phase relations and equation-of-state of aluminous mg-silicate perovskite and implications for earth's lower mantle", Earth and Planetary Science Letters 222, 2, 501–516 (2004a).

Walter, M., E. Nakamura, R. Trønnes and D. Frost, "Experimental constraints on crystallization differentiation in a deep magma ocean", Geochimica et Cosmochimica Acta 68, 20, 4267–4284 (2004b).

Wang, F., Y. Tange, T. Irifune and K.-i. Funakoshi, "P-v-t equation of state of stishovite up to mid-lower mantle conditions", Journal of Geophysical Research: Solid Earth 117, B6 (2012).

Wang, W., Y. Xu, D. Sun, S. Ni, R. Wentzcovitch and Z. Wu, "Velocity and density characteristics of subducted oceanic crust and the origin of lower-mantle heterogeneities", Nature Communications 11, 1, 1–8 (2020).

Weertman, J. and J. R. Weertman, "High temperature creep of rock and mantle viscosity", Annual Review of Earth and Planetary Sciences 3, 1, 293–315 (1975).

Wicks, J., J. Jackson and W. Sturhahn, "Very low sound velocities in iron-rich (mg, fe) o: Implications for the core-mantle boundary region", Geophysical Research Letters 37, 15 (2010).

Wicks, J. K., J. M. Jackson, W. Sturhahn and D. Zhang, "Sound velocity and density of magnesiowüstites: Implications for ultralow-velocity zone topography", Geophysical Research Letters 44, 5, 2148–2158 (2017).

Williams, Q. and E. J. Garnero, "Seismic evidence for partial melt at the base of earth's mantle", Science 273, 5281, 1528–1530 (1996).

Wu, W., S. Ni and J. C. Irving, "Inferring earth's discontinuous chemical layering from the 660-kilometer boundary topography", Science 363, 6428, 736–740 (2019).

Xu, F., D. Yamazaki, N. Sakamoto, W. Sun, H. Fei and H. Yurimoto, "Silicon and oxygen self-diffusion in stishovite: Implications for stability of sio2-rich seismic reflectors in the mid-mantle", Earth and Planetary Science Letters 459, 332–339 (2017).

Xu, J., D. Yamazaki, T. Katsura, X. Wu, P. Remmert, H. Yurimoto and S. Chakraborty, "Silicon and magnesium diffusion in a single crystal of mgsio3 perovskite", Journal of Geophysical Research: Solid Earth 116, B12 (2011).

Xu, W., C. Lithgow-Bertelloni, L. Stixrude and J. Ritsema, "The effect of bulk composition and temperature on mantle seismic structure", Earth and Planetary Science Letters 275, 1-2, 70–79 (2008).

Xu, Y. and K. D. Koper, "Detection of a ulvz at the base of the mantle beneath the northwest pacific", Geophysical research letters 36, 17 (2009).

Yamazaki, D. and S.-i. Karato, "Some mineral physics constraints on the rheology and geothermal structure of earth's lower mantle", American Mineralogist 86, 4, 385–391 (2001).

Yamazaki, D., T. Yoshino and T. Nakakuki, "Interconnection of ferro-periclase controls subducted slab morphology at the top of the lower mantle", Earth and Planetary Science Letters 403, 352–357 (2014).

Ye, Y., C. Gu, S.-H. Shim, Y. Meng and V. Prakapenka, "The postspinel boundary in pyrolitic compositions determined in the laser-heated diamond anvil cell", Geophysical Research Letters 41, 11, 3833–3841 (2014).

Ye, Y., V. Prakapenka, Y. Meng and S.-H. Shim, "Intercomparison of the gold, platinum, and mgo pressure scales up to 140 gpa and 2500 k", Journal of Geophysical Research: Solid Earth 122, 5, 3450–3464 (2017).

Young, P. A., S. J. Desch, A. D. Anbar, R. Barnes, N. R. Hinkel, R. Kopparapu, N. Madhusudhan, N. Monga, M. D. Pagano, M. A. Riner *et al.*, "Astrobiological stoichiometry", Astrobiology 14, 7, 603–626 (2014).

Yu, S. and E. J. Garnero, "Ultralow velocity zone locations: a global assessment", Geochemistry, Geophysics, Geosystems 19, 2, 396–414 (2018).

Yuan, K. and B. Romanowicz, "Seismic evidence for partial melting at the root of major hot spot plumes", Science 357, 6349, 393–397 (2017).

Zhang, Z., S. M. Dorfman, J. Labidi, S. Zhang, M. Li, M. Manga, L. Stixrude, W. F. McDonough and Q. Williams, "Primordial metallic melt in the deep mantle", Geophysical Research Letters 43, 8, 3693–3699 (2016).

Zhao, Y.-H., M. E. Zimmerman and D. L. Kohlstedt, "Effect of iron content on the creep behavior of olivine: 1. anhydrous conditions", Earth and Planetary Science Letters 287, 1-2, 229–240 (2009).

Zindler, A. and S. Hart, "Chemical geodynamics", Annual review of earth and planetary sciences 14, 1, 493–571 (1986).